

MLK-07-080 (Vol II) Copy No.

# Experimental Investigation of Capillary Propellant Control Devices for Low Gravity Environments

## Volume II - Final Report

June 1970

Prepared Under Contract NAS8-21259 for

George C. Marshall Space Flight Center  
Marshall Space Flight Center, Alabama 35812

FACILITY FORM 602	<b>N70-32913</b>	
	(ACCESSION NUMBER)	(THRU)
	150	
	(PAGES)	(CODE)
	CR-110755	27
	(NASA CR OR TMX OR AD NUMBER)	(CATEGORY)

**MARTIN MARIETTA CORPORATION**

Reproduced by the  
**CLEARINGHOUSE**  
for Federal Scientific & Technical  
Information Springfield Va. 22151

Contract NAS8-21259  
Contract Control No. 1-8-52-10187

VOLUME II - FINAL REPORT

EXPERIMENTAL INVESTIGATION OF CAPILLARY  
PROPELLANT CONTROL DEVICES FOR LOW-GRAVITY ENVIRONMENTS

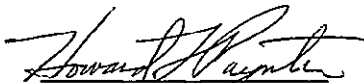
Report Period: June 26, 1967 to June 30, 1970

June 1970

Authors:

George E. Alexander  
Thomas R. Barksdale  
Ralph E. Hise  
Kingsley C. Lunden  
Howard L. Paynter

Approved by:

  
Howard L. Paynter  
Program Manager

Prepared for  
George C. Marshall Space Flight Center  
Marshall Space Flight Center, Alabama 35812

Prepared by  
MARTIN MARIETTA CORPORATION  
Denver Division  
Denver, Colorado 80201

### FOREWORD

This report was prepared by the Martin Marietta Corporation, Denver, Colorado, under Contract NAS8-21259, Experimental Investigation of Capillary Propellant Control Devices for Low-Gravity Environments. It includes work done under an earlier study, Contract NAS8-20837, Design, Fabrication, and Testing of Subscale Propellant Tanks with Capillary Traps. Both programs were conducted for the George C. Marshall Space Flight Center of the National Aeronautics and Space Administration. The period of performance for the first program was from June 26, 1967 to March 15, 1968. The second study covered the period from May 2, 1968 to June 30, 1970.

The work was administered under the technical direction of Mr. Leon J. Hastings of the Propulsion and Vehicle Engineering Laboratory of the George C. Marshall Space Flight Center. A 16 mm film summarizing test results is available at the George C. Marshall Space Flight Center.

CONTENTS

	<u>Page</u>
Foreword . . . . .	ii
Contents . . . . .	iii
Summary . . . . .	x
Nomenclature . . . . .	xi
I. Introduction . . . . .	I-1 thru I-4
II. Martin Marietta's Free-Fall Facility . . . . .	II-1 thru II-4
III. Liquid/Gas Interface Stability (Acceleration Normal to Foraminous Surface) . . . . .	III-1
A. Objectives . . . . .	III-1
B. Experimental Apparatus . . . . .	III-6
C. Test Procedure . . . . .	III-12
D. Experimental Results . . . . .	III-15
E. Discussion of Results . . . . .	III-24 thru III-31
IV. Schemes to Prevent Passage of Settled Pro- pellants through Foraminous Barriers . . . . .	IV-1
A. Objectives . . . . .	IV-1
B. Experimental Apparatus . . . . .	IV-5
C. Test Procedure . . . . .	IV-10
D. Experimental Results . . . . .	IV-12
E. Discussion of Results . . . . .	IV-19 thru IV-34
V. Liquid/Gas Interface Stability (Acceleration Parallel to Foraminous Surface) . . . . .	V-1
A. Objectives . . . . .	V-1
B. Experimental Apparatus and Test Procedure . . . . .	V-1



	C. Experimental Results . . . . .	V-4
	D. Discussion of Test Results . . . . .	V-16 thru V-37
VI.	Filling of Capillary Devices . . . . .	VI-1
	A. Objectives . . . . .	VI-1
	B. Experimental Apparatus and Test Procedure .	VI-2
	C. Experimental Results . . . . .	VI-4
	D. Discussion of Results . . . . .	VI-16 thru VI-27
VII.	Conclusions and Recommendations . . . . .	VII-1
	A. Conclusions . . . . .	VII-1
	B. Recommendations . . . . .	VII-3
VIII.	References . . . . .	VIII-1 thru VIII-4

#### Figure

1	Capillary Trap Concept . . . . .	I-2
2	Cryogenic Storage Concept . . . . .	I-3
3	Compartmented Tank . . . . .	I-3
4	Compartmented Trap Device . . . . .	I-3
5	Trap Device with Perforated Liner . . . . .	I-3
6	Vertical Test Facility . . . . .	II-1
7	Low-g Drop Tower . . . . .	II-2
8	Low-g Capsule Assembly . . . . .	II-3
9	Basic Test Setup Used to Evaluate Passive Barriers . . . . .	II-4
10	NEG'ATOR Constant Torque Motor (Bottom View of Test Cell) . . . . .	II-5
11	Propellant Interface Locations . . . . .	III-2
12	Wetting Liquid in a Cylindrical Tube . . . . .	III-4
13	Basic Hydrostatic Pore Stability Condition Investigated . . . . .	III-7
14	Cylindrical Test Specimens . . . . .	III-7

15	Typical Test Setup . . . . .	III-7
16	Perforated Plate Barriers . . . . .	III-10
17	Typical Screen Barriers . . . . .	III-11
18	Typical Hole Layout Pattern for Plates with Constant Hole Size . . . . .	III-11
19	Filmed Sequence of Run 2, Showing Pore In- stability Due to Incomplete Wetting of Barriers . . . . .	III-13
20	Drop Test Setup, Showing Vertical Ball Travel Meter . . . . .	III-17
21	Stability Characteristics of Perforated Plate Barriers . . . . .	III-19
22	Stability Characteristics of Square Weave Screen Barriers . . . . .	III-20
23	Sequence Showing Pore Stability from Run 22a . .	III-22
24	Test Results from Runs 2a and 8a . . . . .	III-23
25	Bubble Formation Due to Pore Instability, Run 31d . . . . .	III-29
26	Passive Barrier Control Problem . . . . .	IV-1
27	Settling Bond Number vs Cylindrical Tank Radius .	IV-3
28	Categorization of Flow Regimes During Settling	IV-4
29	Square Hole Pattern . . . . .	IV-7
30	Staggered Hole Pattern . . . . .	IV-7
31	Double-Plate Barrier with Offset Pores . . . . .	IV-7
32	Multi-tube Insert Barrier . . . . .	IV-9
33	Barrier 7 . . . . .	IV-9
34	Screen Tube Used in Barrier 8 . . . . .	IV-9
35	Pie-Tin Barrier . . . . .	IV-10
36	Settling Results for Run 60 . . . . .	IV-11

37	Test Specimen with Perforated Plate and Annular Deflector Ring . . . . .	IV-12
38	Impact Velocity of Liquid Column vs Settling Bond Number . . . . .	IV-14
39	Columnar Velocity Factor . . . . .	IV-15
40	Damping Categories A thru G . . . . .	IV-22
41	Damping Performance of Single-Layer Perforated Plate Barriers . . . . .	IV-23
42	Damping Performance of Double-Layer Perforated Plate Barriers . . . . .	IV-23
43	Damping Performance of Single-Layer Square Weave Barriers . . . . .	IV-24
44	Damping Performance of Single-Layer Dutch Twill Barriers . . . . .	IV-24
45	Test Results for Run 23 . . . . .	IV-25
46	Test Results for Run 37 . . . . .	IV-26
47	Cross-Sectional Views of Various Screen Weaves . . . . .	IV-27
48	Test Results for Runs 38 and 56 . . . . .	IV-28
49	Hydrostatic Condition Following Damping . . . . .	IV-29
50	Typical Screen Containment Results . . . . .	IV-30
51	Test Results for Run 46, $\Delta t = 1.9$ sec . . . . .	IV-31
52	Plexiglas Model for 1-g Lateral Stability Tests . . . . .	V-1
53	Bench Test Setup . . . . .	V-2
54	Lateral Accelerator Mechanism (15 in. of travel) . . . . .	V-3
55	Lateral Motion Device (approximately 2 ft of travel) . . . . .	V-3
56	Box-Like Test Specimen . . . . .	V-4
57	Box-Like Test Specimen Positioned on Lateral Travel Mechanism . . . . .	V-5
58	Pressure Retention under Lateral Acceleration . . . . .	V-5

59	Lateral Acceleration Test, Run 195 . . . . .	V-18
60	Lateral Acceleration Test, Run 205 . . . . .	V-19
61	Stability Characteristics for Straight-Hole Perforated Plates . . . . .	V-20
62	Stability Characteristics for Straight-Hole Perforated Plates . . . . .	V-20
63	Stability Characteristics for Cone-Hole Perforated Plates . . . . .	V-21
64	Stability Characteristics for Square-Weave Screens . . . . .	V-21
65	Stability Characteristics for 30x250-Mesh Screens . . . . .	V-22
66	Stability Characteristics for 24x110-Mesh Screens . . . . .	V-22
67	Stability Characteristics for Straight-Hole Perforated Plates . . . . .	V-24
68	Stability Characteristics for Cone-Hole Perforated Plates . . . . .	V-24
69	Stability Characteristics for Square-Weave Screens . . . . .	V-25
70	Stability Characteristics for Dutch-Twill Screens . . . . .	V-25
71	Effect of Open-to-Closed Area Ratio on Stability of Perforated Plates . . . . .	V-26
72	Possible Sideways Liquid Motion . . . . .	V-27
73	Annulus Being Filled in Run 4 . . . . .	VI-3
74	Annulus Fill Time vs Liquid-to-Container Volume Ratio . . . . .	VI-6
75	Annulus Fill Test, Run 11 . . . . .	VI-7
76	Annulus Fill Test, Run 19 . . . . .	VI-8
77	Comparison of Predicted and Recorded Fill Time for a Spherical Annulus . . . . .	VI-10
78	Schematic Representation of Annulus Filling . .	VI-12

79	Possible Liquid/Gas Annulus Condition . . . . .	VI-17
80	No Continuous Liquid Path to Bulk Liquid . . . . .	VI-18
81	Schematic Sketch of Annulus . . . . .	VI-20
82	Nondimensional Capillary Pressure Difference Across a Liquid Interface Inside a Spherical Annulus . . . . .	VI-22
83	Schematic Representation of a Wetted Screen . . . . .	VI-23
84	Sketch of Possible Baffle Scheme to Delay Wetting of Screen Liner . . . . .	VI-27

Table

1	Physical Properties of Test Liquids and Storable Propellants . . . . .	III-3
2	Perforated Plate Barrier Specification . . . . .	III-8
3	Square Weave Screen Barrier Specifications . . . . .	III-9
4	Summary of Test Results . . . . .	III-14
5	Pertinent Variables and Their Uncertainty Intervals . . . . .	III-27
6	Perforated Plate Barriers . . . . .	IV-6
7	Screen Barriers . . . . .	IV-6
8	Dutch-Twill Micron Ratings . . . . .	IV-8
9	Liquid-Wall-Flow Velocity Factors, $K_w$ . . . . .	IV-17
10	Physical Properties of Test Liquids . . . . .	IV-17
11	Summary of Single-Layer Perforated Plate Tests . . . . .	IV-18
12	Summary of Double-Layer Perforated Plate Tests . . . . .	IV-19
13	Summary of Single-Layer Square Weave Barrier Tests . . . . .	IV-20
14	Summary of Double-Layer Square Weave Screen Tests . . . . .	IV-20
15	Summary of Multitube Barrier Tests . . . . .	IV-20
16	Summary of Single-Layer Dutch Twill Barrier Tests . . . . .	IV-21

17	Uncertainty Intervals for Pertinent Variables Used to Calculate $B_o$ . . . . .	IV-33
18	Uncertainty Intervals for Pertinent Variables Used to Calculate Impingement $W_e$ . . . . .	IV-33
19	One-g Lateral Stability Test Results . . . . .	V-8
20	Foraminous Samples Used for Drop Tests (2.2 in. of Lateral Travel) . . . . .	V-8
21	Lateral Acceleration Test Results (2.2-in. Lateral Travel Device) . . . . .	V-9
22	Foraminous Samples Used for Drop Tests (15.0 in. of Lateral Travel) . . . . .	V-9
23	Barriers Used in Lateral Acceleration Tests . .	V-10
24	Lateral Acceleration Stability Test Results . .	V-11
25	Uncertainty Intervals for Sample Variables Used to Calculate $\phi$ and $G_a$ . . . . .	V-29
26	Per Cent Uncertainty for Lateral Stability Tests Made with Lateral Travel Mechanism Shown in Fig. 58 . . . . .	V-29
27	Summary of Data on Annulus Filling . . . . .	VI-5

SUMMARY

An experimental program was conducted in Martin Marietta's 2.1-sec drop tower to collect and verify criteria needed to design capillary systems to provide orientation and control liquid propellant during low-g accelerations. More than 300 drop tests were made under controllable and repeatable near-constant accelerations applied normal and parallel to flat perforated plates and screens to evaluate liquid/gas interface stability and liquid damping criteria. The ability of annuli formed by screens to refill by capillary pumping was also studied. Test liquids were Freon-TF, carbon tetrachloride, chloroform, and methanol. The test results and dimensionless parameters presented are applicable to the design of capillary systems that rely only upon surface tension and system pressure to control liquid propellants during coasting phases of space missions.

NOMENCLATURE

$a$	=	acceleration
$a_L$	=	lateral acceleration
$A$	=	area
$b$	=	radius of curvature
$B$	=	intercept
$Bo$	=	Bond number
$d$	=	pore diameter
$D$	=	hydraulic diameter
$f$	=	force
$fs$	=	film speed
$Fr$	=	Froude number
$g$	=	gravitational acceleration
$g_c$	=	gravitational constant
$Ga$	=	Galileo number (modified)
$h$	=	distance
$K$	=	empirical factor
$K_c$	=	columnar velocity factor
$K_w$	=	wall-flow velocity factor
$\ell$	=	annulus gap width
$L$	=	liquid height
$L_v$	=	vertical travel distance
$m$	=	slope
$M$	=	mass
$n$	=	force ratio



$N$	=	number of pores (per hole circle)
$P$	=	pressure
$\Delta P$	=	differential pressure
$r$	=	pore radius
$R$	=	cylinder radius
$R_c$	=	critical tube radius
$Re$	=	Reynolds number
$t$	=	time
$t'$	=	characteristic time
$\Delta t$	=	time interval
$T$	=	barrier thickness
$v$	=	velocity
$v_c$	=	columnar impingement velocity
$v_w$	=	wall-flow velocity (average)
$v_L$	=	lateral velocity
$V$	=	volume
$V_C$	=	container volume
$V_L$	=	liquid volume
$V_R$	=	volume ratio ( $V_L/V_C$ )
$w$	=	uncertainty interval
$W_L$	=	liquid weight
$We$	=	Weber number
$\Delta x$	=	lateral travel increment
$Z$	=	bubble height (in liquid)

$\emptyset$	=	dimensionless parameter (ratio of acceleration-to-capillary forces)
$\theta$	=	liquid-to-solid contact angle
$\Phi$	=	factor (contribution of contact angle effects, etc.)
$\mu$	=	absolute viscosity
$\nu$	=	kinematic viscosity
$\sigma$	=	interfacial surface tension
$\rho$	=	density
$\beta$	=	kinematic surface tension
$\xi$	=	open-to-closed area ratio
$\eta$	=	axisymmetric free-surface height

Subscripts

A	=	annulus
$a_L$	=	lateral acceleration
b	=	buoyant
B	=	bubble
Bo	=	Bond number
c	=	capillary
C	=	container
d	=	pore diameter
f	=	force
fs	=	film speed
$\Delta f$	=	16mm frame interval
g	=	gas

$h$	=	distance
$\ell$	=	liquid
$M$	=	mass
$N$	=	NEG'ATOR motor
$P$	=	pressure
$r$	=	pore radius
$R$	=	cylinder radius
$u$	=	ullage
$v$	=	velocity
$V$	=	vapor
$\Delta x$	=	lateral travel increment
$0,1,2$	=	stations
$\phi$	=	dimensionless parameter
$\sigma$	=	interfacial surface tension
$\beta$	=	kinematic surface tension
$\nu$	=	kinematic viscosity
$\rho$	=	density

## I. INTRODUCTION

The use of surface-tension devices is one of the more promising means for the orientation and control of fluids to supply single-phase liquid, as required, during conditions of near-weightlessness. Liquid transfer between orbiting vehicles and restart of a liquid rocket engine after coast periods in space are particularly promising applications. Transfer and/or propellant acquisition will be required for future vehicles, e.g., Space Tug, Nuclear Shuttle, Space Station, Orbital Propellant Depot and the Space Shuttle.

The attractiveness of these devices is borne out by the results of present, and recent, contractual studies. Lockheed Missiles and Space Company and General Dynamics/Convair selected surface tension as the method for propellant control for the Advanced Maneuvering Propulsion System (AMPS), Ref 1. Martin Marietta Corporation chose a capillary design for the propellant management of an advanced spacecraft propulsion system (Ref 2). They were also selected for post-'75 Mars missions and for the Grand Tour (of Jupiter, Saturn, Uranus, and Neptune) under Contract NAS7-754 (Ref 3).

The AMPS study, and the capillary designs under Contracts NAS8-21465 (Ref 4) and NAS9-10480 (Ref 5), are for cryogenic propellants. The NASA-MSFC study evaluated designs for large-scale vehicles, such as the S-IVC; the NASA-MSC program is concerned with satisfying the cryogenic storage requirements for the Space Shuttle.

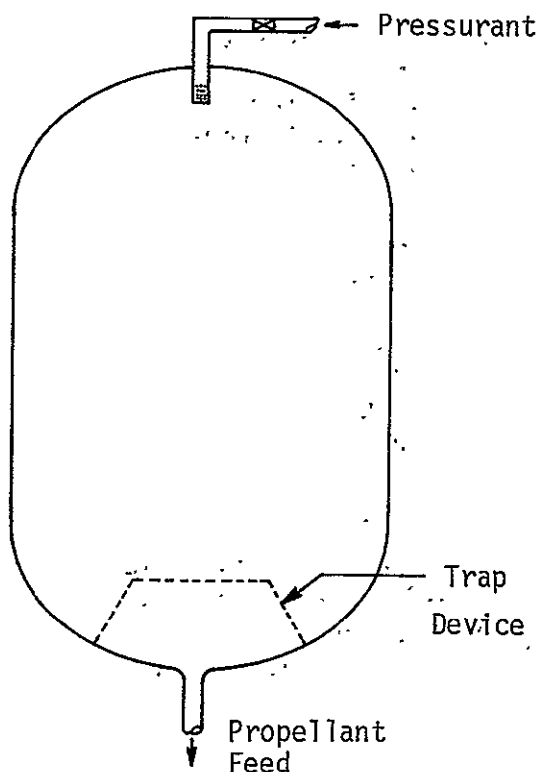
The operational principle of these passive devices is discussed in Ref 6. Ullage pressure supports the liquid in its desired location while surface tension maintains separation of the fluid phases by stabilizing the liquid-ullage interface at the foraminous material. Such surface-tension systems use either screens or perforated plates that are configured within the tank to control part, or all, of the propellant during the coasting (unpowered) phases of orbital and interplanetary missions.

A typical passive device is pictured in Fig. 1. It is sized to provide enough liquid at the tank outlet so that gas-free liquid is available to the engine on demand. A simple trap device holds the liquid within the trap under the perturbing forces caused by vehicle drag or attitude-control maneuvers, and may be designed so that it is refilled with liquid during each engine burn.

The device, as shown, is applicable to cryogenic propellants only if additional means are used to prevent heat leak into the tank that would cause vaporization within the trap. One possible scheme is to maintain the cryogen at a sub-cooled state, as pictured in Fig. 2. In this method, fluid is withdrawn from the tank, expanded to a lower pressure and temperature, and then heated while passing through coils on the tank wall before being vented overboard (Ref 7).

In addition to providing gas-free liquid to the engine, capillary devices may be used to control the location of the bulk propellant to minimize the center-of-mass offset. This may be done by compartmenting the tank, as pictured in Fig. 3. The number and location of the foraminous barriers are dictated by the number of major propellant demands and the center-of-mass control required. The concept shown in Fig. 3 is indicative of three major engine burns. Each compartment is sized to the major propellant demands.

Additional design features may be needed to satisfy requirements for more sophisticated missions. For example, interplanetary missions require gas-free liquid for one or more trim maneuvers



after expending 95% or so of the loaded propellant during orbital insertion (Ref 3). One approach to meet these large-ullage trim burns is to compartment the trap itself, as shown in Fig. 4; here each compartment is sized to satisfy each trim demand. A second approach is to use a perforated liner, as shown in Fig. 5, to prevent the ingestion of ullage during liquid expulsion. As shown by the flow path in this figure, propellant within the trap is drained from the tank by flowing through the liner and then into the liquid-annular-region between the foraminous material and the tank wall.

Fig. 1 Capillary Trap Concept

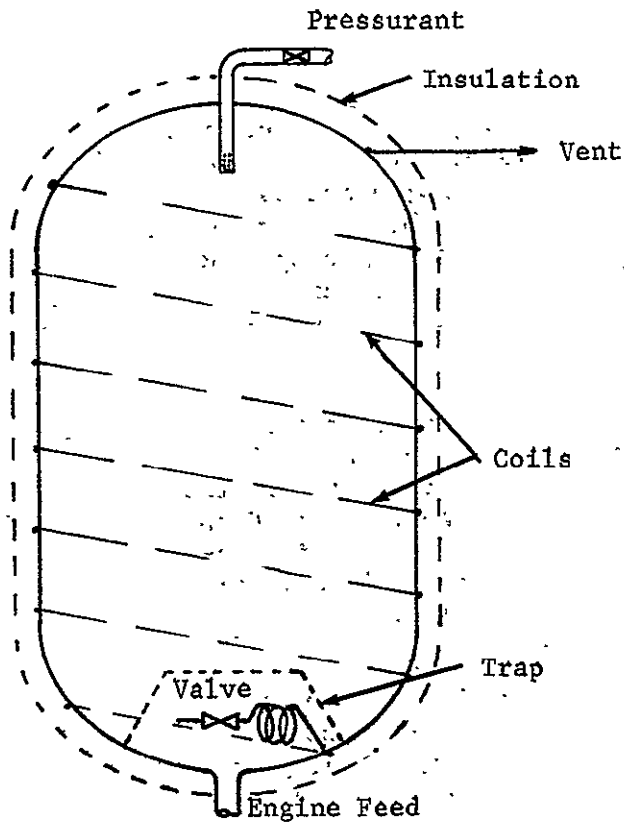


Figure 2 Cryogenic Storage Concept

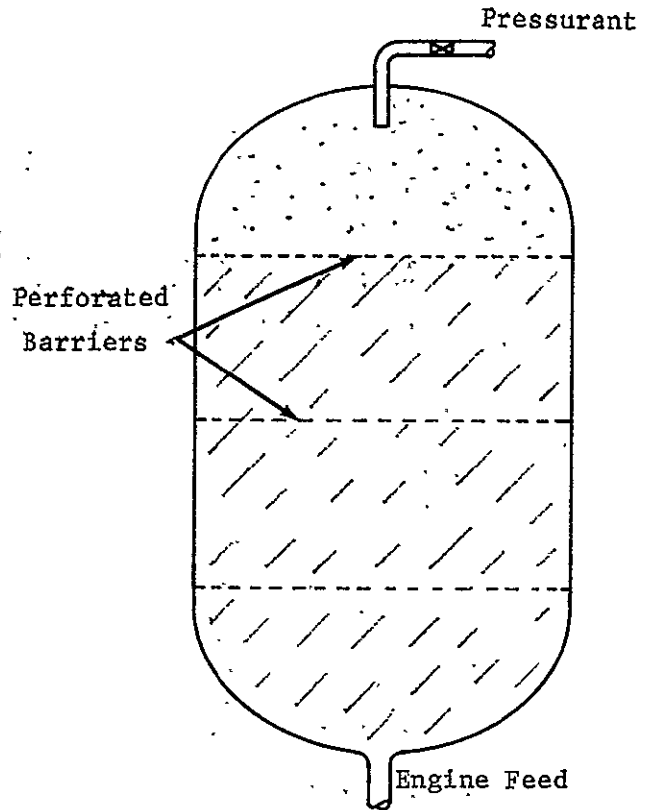


Figure 3 Compartmented Tank

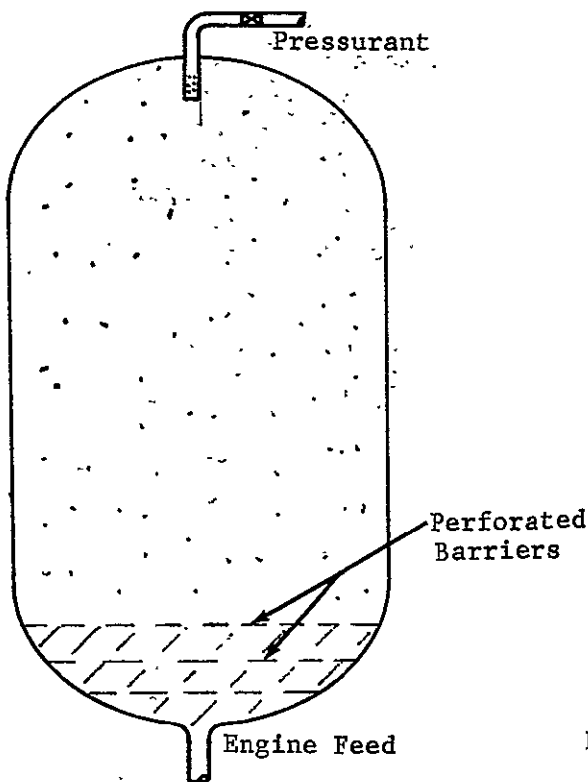


Figure 4 Compartmented Trap Device

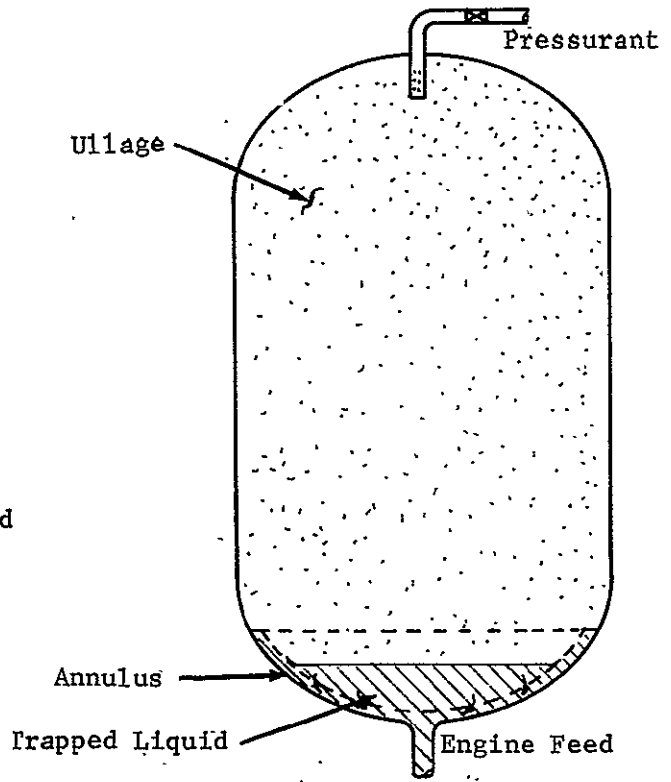


Figure 5 Trap Device with Perforated Liner

The simple capillary concepts shown in Fig. 1 thru 5 are attractive when compared to other liquid-orientation and control concepts because they are applicable to both cryogens and non-cryogens, and are completely passive; i.e., they have no moving parts and require no additional power. In addition, the systems are not limited by tank geometry and size, nor by the number of liquid expulsions, and they tend to be lighter than those that utilize other control techniques.

The work described in this report was begun under Contract NAS8-20837 in June 1967 and continued under Contract NAS8-21259 from May 1968 to June 1970. Both programs were conducted in the Denver Division's 2.1-sec drop tower, which is described in Chapter II. The overall objective of the studies was to provide engineering data to advance the state-of-the-art of capillary designs for liquid-propellant orientation and control.

The specific objectives under Contract NAS8-20837 were to evaluate the liquid/gas interfacial stability provided by perforated plates and square-weave screens under a near-constant acceleration acting normal to the foraminous surface. In this study, the initial level of the liquid was above the foraminous material. The experimental apparatus, test procedure, and results are presented in Chapter III.

The program objectives for Contract NAS8-21259 were to evaluate: (1) various schemes for preventing the passage of settled propellants through foraminous barriers; (2) the liquid/gas interfacial stability provided by perforated plates and screens under a near-constant acceleration acting parallel to the foraminous surface; and (3) liquid filling of annuli and the removal of vapor pockets during filling. The experimental apparatus, test procedure, and results are presented for each of these objectives in Chapters IV, V, and VI.

The overall conclusions and recommendations are presented in Chapter VII. References are listed in Chapter VIII.

## II. MARTIN MARIETTA'S FREE-FALL FACILITY

The experimental program was conducted in Martin Marietta's drop tower, which is located in the vertical test facility (VTF). The VTF is pictured in Fig. 6.

A schematic of the drop tower is shown in Fig. 7. The 75-ft free-fall distance provides a usable low-g test duration of 2.1 sec. The drop-capsule package consists of an outer capsule (drag shield) and an inner capsule (test cell), as shown in Fig. 8. Each drop is initiated by severing a 5/16-in.-diameter machine bolt that supports the entire capsule package. The free-fall terminates when the legs and the annular-ring assembly attached to the bottom of the drag shield embed themselves in wheat stored in a large cylindrical bin (see Fig. 7). Deceleration takes less than 0.15 sec, during which the peak acceleration is less than 25 g.

The test cell houses the test specimen, the battery pack, and the 16-mm Milliken Model DBM 3a camera. A back-lighting technique is used to illuminate the transparent test specimens and to permit photographic documentation at a camera speed of 200 fps.

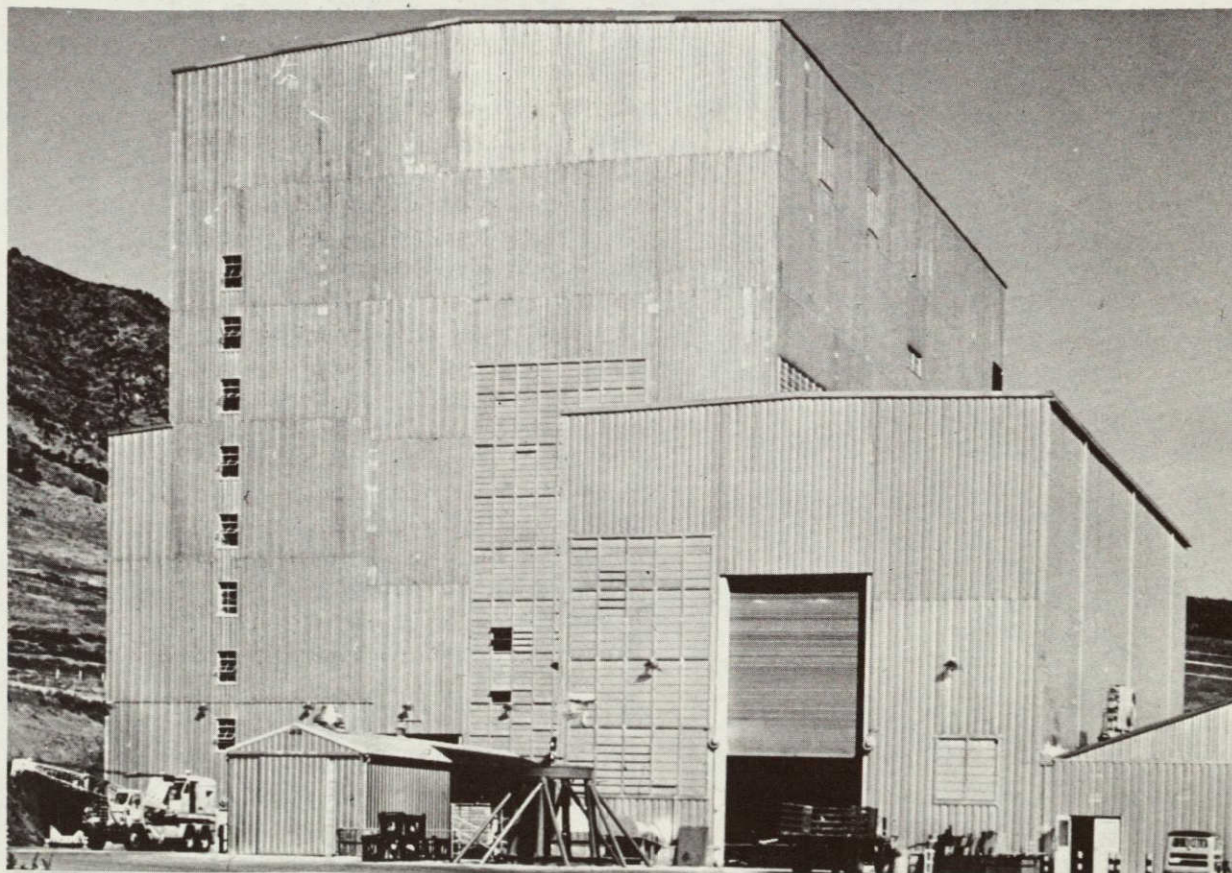


Fig 6 Vertical Test Facility



For this program, tests were conducted at near-zero accelerations and at axial accelerations less than or equal to 0.055 g. The zero-g condition was achieved by allowing the test cell to fall independently within the drag shield. The air drag on the test cell and the piston effect due to relative travel between the two capsules were both reduced to an insignificant level (less than  $10^{-5}$  g) by evacuating the space between the test cell and the drag shield. The absolute pressure was less than 5 mm of Hg for all tests.

The near-axial force used to accelerate the test cell was provided by NEG'ATOR\* constant-torque motors (see Fig. 8). Upon release of the capsule package, the NEG'ATOR motor pulled the test cell downward within the drag shield until an aluminum tube attached to the bottom of the test cell bottomed in the drag shield. The length of the tube was sized so that bottoming occurred milliseconds before the drag shield contacted the wheat.

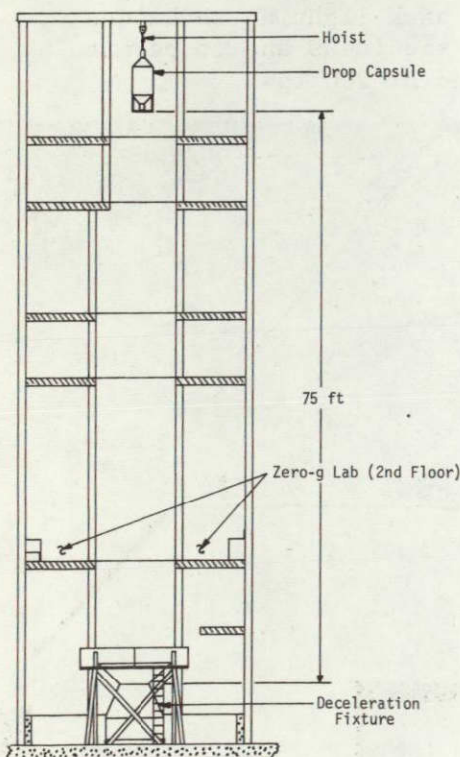


Fig. 7 Low-g Drop Tower

The NEG'ATOR motors used for testing were selected after measuring their constancy of force vs. linear deflection on a tensile tester (Tinnius Olsen Universal Test Machine). The test cell was weighed before each test, and the average axial acceleration during free-fall was calculated using the mass of the test cell and the average force measured for the motor over its deflection range during the drop test.

The test specimens were mounted on a flat platform in view of the Milliken camera (see Fig. 9). The glass specimens were washed in a warm detergent solution, rinsed with tap water, and air-dried before each test. The foraminous material was dipped in an acid solution, rinsed with water, and air-dried before being placed in the cylinders.

\*Manufactured by Hunter Spring Co., Hatfield, Pennsylvania.

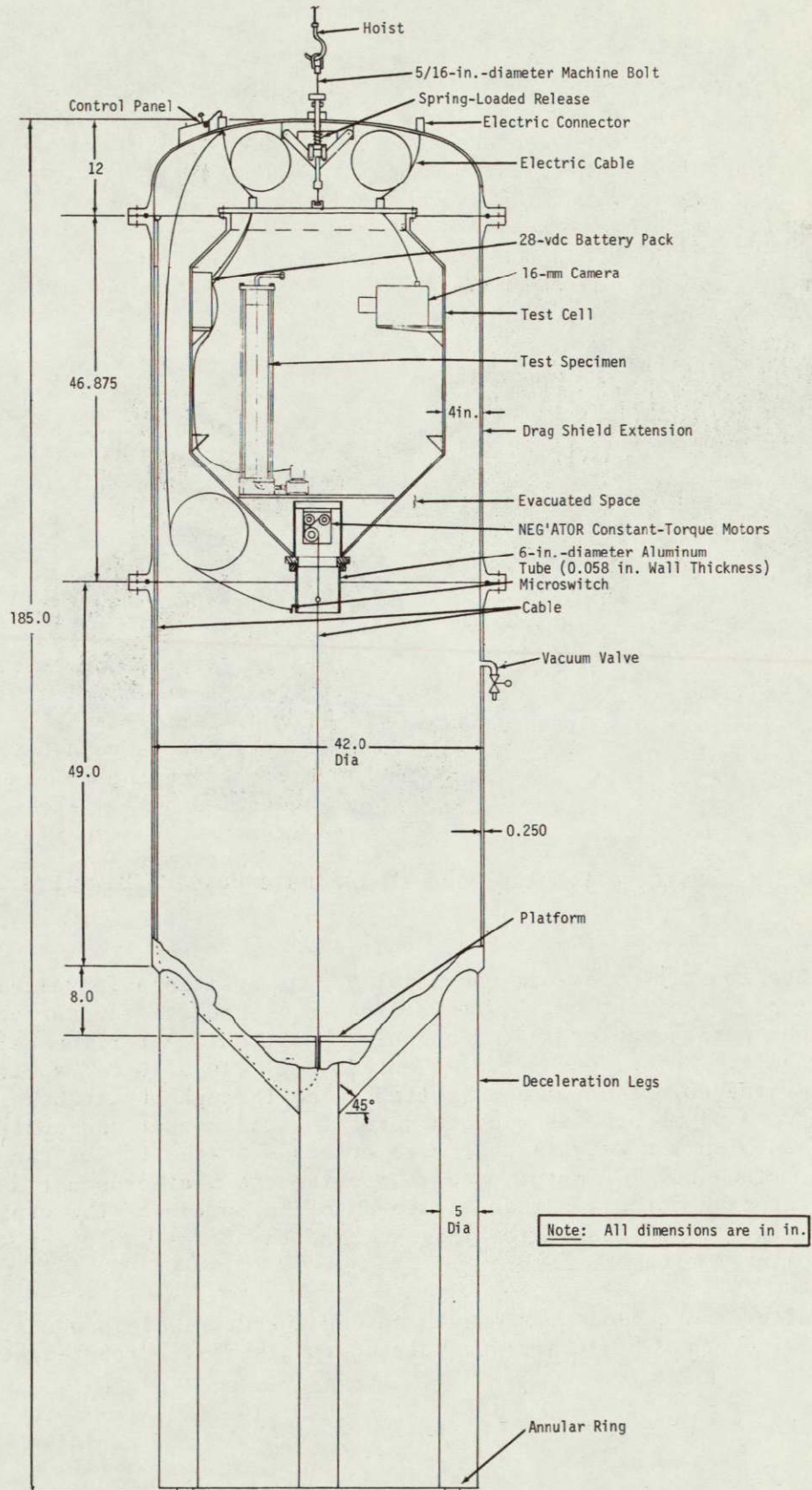


Fig. 8 Low-g Capsule Assembly



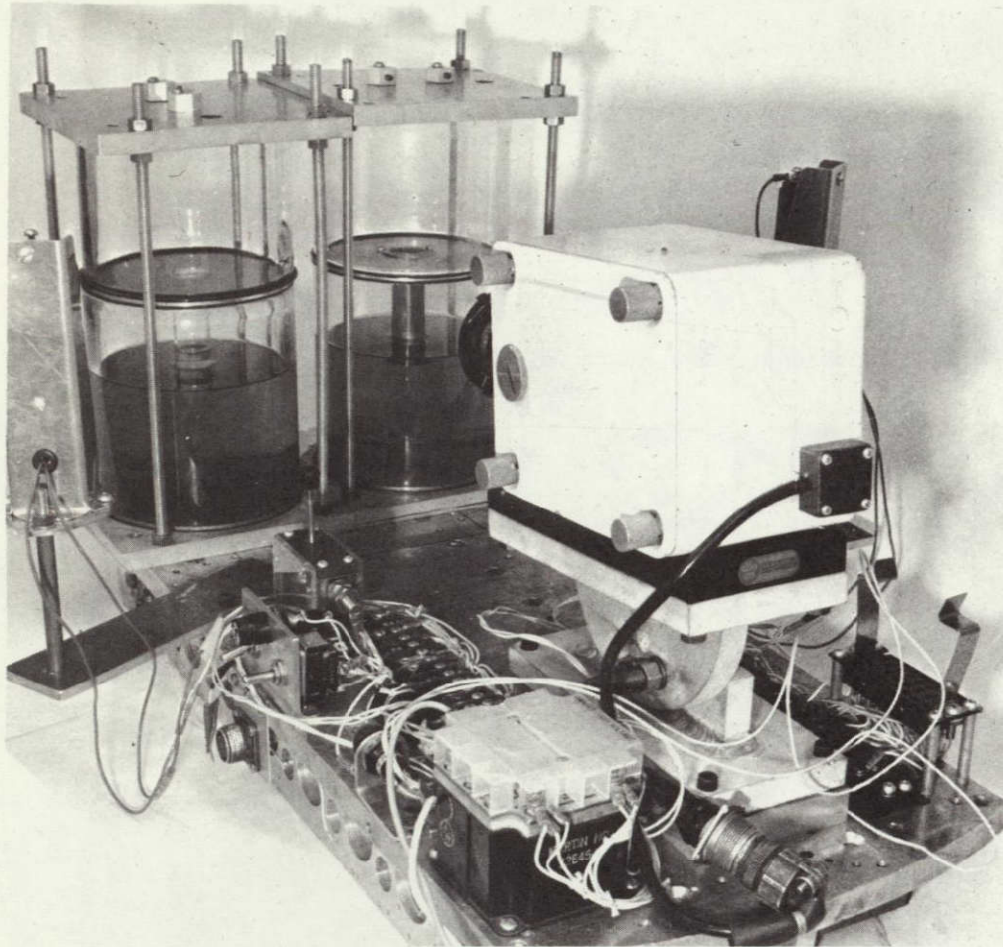
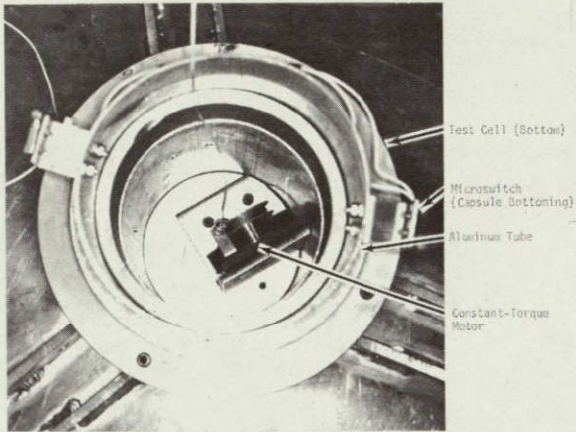


Fig. 9 Basic Test Setup Used to Evaluate Passive Barriers

The mounting platform (see Fig. 9) was positioned parallel to the top of the test cell (within 1/64 in.), and its top surface was set perpendicular to the capsule's vertical centerline using a transit. Before each drop, the test cell was balanced so its centerline coincided with a vertical line through its suspension point. A plumb bob was used to determine the amount and position of the balancing weights that were attached to the top of the test cell. The NEG'ATOR motor used to provide the near-constant axial accelerating force was then attached to the bottom of the capsule (see Fig. 10) on its centerline, so that the force would act along this line during the test.

After the capsule was assembled and the drag shield was evacuated, the capsule package was hoisted to its 75-ft drop height



and held for about 5 minutes to allow itself and its contents to stabilize before being dropped. The camera and lights were activated approximately 1 sec before the capsule was released to permit the 16-mm camera to attain a constant film speed and to provide a 1-g reference.

Fig. 10 NEG'ATOR Constant-Torque Motor  
(Viewing Bottom of Test Cell)



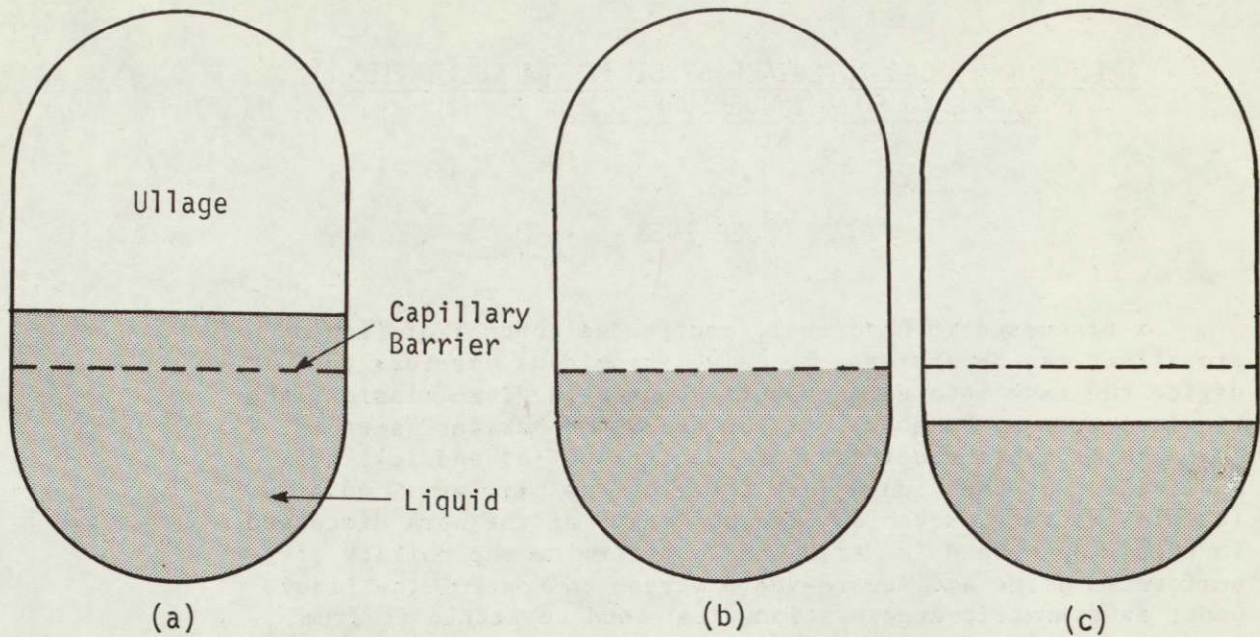


Fig. 11 Propellant Interface Locations

This phenomenon may be explained by referring to Fig. 12. The wetting liquid (meniscus downward) is pictured in the tube after the tube is lifted from the liquid reservoir. Surface tension and gravitational acceleration tend to displace liquid from the tube. The supporting force is provided by the difference in ullage pressure above and below the liquid column. If the tubes are uncapped, the pressure difference,  $P_o - P_1$ , becomes zero and liquid is lost.

If it were possible to cap the tube with no ullage above the liquid column, the maximum supporting pressure difference would be  $P_o - P_v$ , where  $P_v$  is the vapor pressure of the liquid\*. If, however, the tube is capped with an initial ullage pressure  $P_1$ , that is equal to  $P_o$  ( $P_o = P_1$ ), liquid will be lost from the tube until a pressure difference is reached that will provide liquid support:

---

\* This is the condition provided in the drop tests, as discussed later.



### III. LIQUID/GAS INTERFACE STABILITY (ACCELERATION NORMAL TO FORAMINOUS SURFACE)

#### A. OBJECTIVES

As discussed in Chapter I, continuous control of liquid propellant may be achieved by using foraminous barriers to divide the tank into compartments. During a given mission, the liquid level may be above, at, or below the barrier (see Fig. 11). The more probable conditions are Conditions (a) and (c); the possibility of the liquid just covering the barrier, Condition (b), is not very probable. The objective of the work discussed in this chapter and in Ref 8 was to determine the ability of perforated plate and square-weave screen to control the liquid under axisymmetric accelerations that tend to settle it from Conditions (a) and (b) in Fig. 11 through the barrier to the opposite end of the tank. The third case, Condition (c), is treated in Chapter IV.

Passive liquid control is achieved by using the system (ullage) pressure to support the liquid and by allowing the surface tension to stabilize the liquid/ullage interface at the foraminous material (Ref 6). This may easily be checked using simple, open-ended glass tubes of small diameter. By immersing one end of each tube in a wetting liquid, such as methanol\*, and then withdrawing the tube, one finds that liquid will stay in the smaller tubes ( $D < 1/8$  in.) only when the open end that is not immersed is capped off. If the tube is not capped, liquid is lost, regardless of size. For the larger tubes ( $D > 1/8$  in.), liquid is lost even when the tubes are capped.

---

\*Liquids of interest for space applications are considered wetting; i.e., they possess a liquid-to-solid contact angle,  $\theta$ , less than  $90^\circ$  when in contact with metals. Table 1 shows that liquid propellants are extremely good wetters; i.e.,  $\theta \approx 0^\circ$ . If one uses glass tubes in the capillary demonstration, it is best to use a liquid like methanol, instead of water, to simulate the storable propellants and cryogenics, because water tends to be non-wetting to glass.



Table I Physical Properties of Test Liquids and Storable Propellants

PROPELLANTS	TEMPERATURE (°C)	DENSITY, $\rho$ (lb <sub>m</sub> /ft <sup>3</sup> )	SURFACE TENSION, $\sigma$ (x 10 <sup>3</sup> lb <sub>f</sub> /ft)	KINEMATIC SURFACE TENSION, $\beta$ (x 10 <sup>4</sup> ft <sup>3</sup> /sec <sup>2</sup> )	CONTACT ANGLE, $\theta$ (deg)*	VISCOSITY, $\mu$ (x 10 <sup>3</sup> lb <sub>m</sub> /ft- sec)
<b>Fuels:</b>						
Aerazine-50	20	55.5(a)	2.07(a)	12.0	0 to 2(a)	0.581(b) at 21°C
MMH		54.6(c) at 24°C	2.35(c) at 20°C	13.8		0.518(c) at 25°C
UDMH	20	49.4(d)	1.92(d)	12.5	0 to 0.75(d)	0.37(e)
MHF-5	20	63.0(f)	2.64(g)	13.5		1.64(h) at 16°C
JP-4	20	48.4(i)	1.55(d)	10.3		0.712(e)
Hydrogen	-254	4.48(d)	0.162(d)	11.6	0(j)	
<b>Oxidizers:</b>						
Nitrogen Tetroxide	20	90.6(d)	1.88(d)	6.68		0.277(e) at 21°C
Nitric Acid (Fuming)	20	97.2(a)	3.01(a)	9.98	0 to 3(a,d)	0.918(e)
Chlorine Trifluoride	11.7	115.5(k)	1.70(k)	4.74		0.292(l)
Oxygen	-183	71.2(d)	0.908(d) at -192°C	4.10	0(j)	
<b>Monopropellants:</b>						
Hydrogen Pero- xide (90%)	20	87.0(a)	5.41(a)	20.0	1 to 2(a)	0.849(e)
Hydrazine	20	62.4(a)	4.33(a)	22.3	0 to 2(a)	0.654(e)
<b>Test Liquids</b>						
Methanol	20	49.4(i)	1.55(i)	10.1	0(i)	0.453(m)
Carbon Tetrachloride	20	99.6(i)	1.84(i)	5.95	0(i)	0.645(n)
Freon-TF	20	98.6(i)	1.27(i)	4.15	0(i)	0.468(n)

\* Contact angles for storables are for Pyrex, 6061-T6 polished aluminum, 301 polished stainless steel, and ASTM 8348-59T Grade 6 polished titanium alloy; for test liquids, they represent contact with Pyrex.

## References:

- (a) *Summary Report: Studies of Interfacial Surface Energies*. NASA CR-54175. Harris Research Laboratories, Rockville, Maryland, December 1964.
- (b) *Storable Liquid Propellants for Titan II*. LRP 198 (Rev A). Aerojet-General Corp, Sacramento, California, September 30, 1960.
- (c) R. W. Lawrence: *Handbook of Properties of UDMH and MMH*. 1292. Aerojet-General Corp, Sacramento, California, May 1958.
- (d) W. C. Reynolds, M. A. Saad, and H. M. Satterlee: *Capillary Hydrostatics and Hydrodynamics at Low g*. T.R. LG-3. Mechanical Engineering Dept, Stanford University, Stanford, California, September 1964.
- (e) *Liquid Propellants Handbook*. Battelle Memorial Institute, Columbus, Ohio, October 1958.
- (f) *Handbook of Chemistry and Physics*. 44th Edition. Chemical Publishing Co, Cleveland, Ohio.
- (g) *Final Report: Evaluation of Propellant Containment and Venting Devices for Zero-Gravity Applications*. AFRPL-TR-65-118. Bell Aerosystems Co, Buffalo, New York, June 1965.
- (h) S. Tannenbaum et al: *Advanced Propellants Investigation for Pre-Packaged Liquid Engine*. RMD 5046-F. Thiokol Chemical Corp, Danville, New Jersey, June 10, 1965.
- (i) W. J. Masica et al: *Hydrostatic Stability of the Liquid-Vapor Interface in a Gravitational Field*. NASA TN D-2267. May 1964.
- (j) C. E. Siegert et al: *Behavior of the Liquid-Vapor Interface in a Gravitational Field*. NASA TN D-2658. February 1965.
- (k) P. A. Friedman and J. Winkler: *Properties of Fluorine and Fluorine-Based Propellants*. TM-0444-64-8. Martin Marietta Corporation, Denver, Colorado, July 1964.
- (l) A. H. Banks, A. Davies, and A. J. Rudge: "Determination of Surface Tension and Viscosity of Liquid Chlorine Trifluoride." *J. Chemical Society*, 732-5, 1953.
- (m) *Chemical Engineering Handbook*. Third Edition. Edited by J. H. Perry. McGraw-Hill, Inc, New York City, New York, 1950.
- (n) E. J. Bennett and G. J. Roewe, Jr.: *Cleaning Electronic and Space Apparatus with "Freon" Precision Cleaning Agent*. Solvent Bulletin FST-4. E. I. duPont de Nemours & Co, Inc, Wilmington, Delaware.



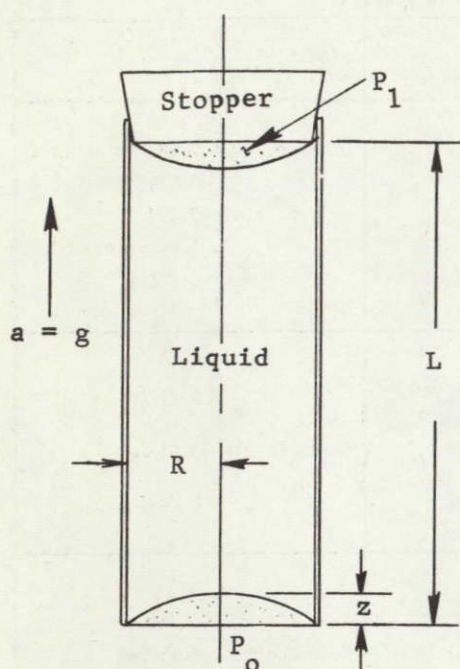


Fig. 12 Wetting Liquid in a Cylindrical Tube

$$W_L \approx \rho_L L \pi R^2 \frac{a}{g_c}; \quad [1]$$

and the supporting pressure force will be

$$f_p = (P_0 - P_1) \pi R^2. \quad [2]$$

As shown in Eq [1] and [2], for a given supporting pressure difference  $(P_0 - P_1)$ , a liquid height ( $L$ ) will be supported regardless of the tube radius ( $R$ ). The tube experiments will verify this, but only to a maximum tube size (about 1/8 in. in diameter for methanol). Beyond this size, the liquid-gas interface at the free surface of the liquid (bottom of the tube) becomes unstable, gas enters, and liquid is displaced.

As pictured in Fig. 12, surface tension tends to stabilize the interface and prevent any liquid from being displaced by gas entering the tube. Let us assume that the gas bubble tending to rise through the liquid due to buoyancy has a height of  $z$ , then we may express its volume,  $V_B$ , as

$$V_B \approx R^2 z, \quad [3]$$

and the buoyant force,  $f_b$ , as

$$f_b \approx (\rho_L - \rho_u) R^2 z \frac{a}{g_c}; \quad [4]$$

or, if we assume  $z \approx R$ ,

$$f_b \approx (\rho_L - \rho_u) R^3 \frac{a}{g_c}. \quad [5]$$



The surface tension force,  $f_\sigma$ , tending to oppose this force can be approximated by

$$f_\sigma \approx 2\pi R \cos \theta, \quad [6]$$

where  $\sigma$  is the liquid/gas surface tension. If we assume that the liquid-to-solid contact angle,  $\theta$ , is near-zero, then

$$f_\sigma \approx 2\pi R. \quad [7]$$

A ratio of the buoyant-to-surface tension forces can then be expressed in the following manner:

$$n = \frac{(\rho_l - \rho_u) a R^2}{\sigma}. \quad [8]$$

For most applications, the gas density ( $\rho_u$ ) is negligible with respect to that for the liquid, and we can express the force ratio as

$$n = \frac{\rho_l a R^2}{\sigma}, \quad [9]$$

where  $\rho$  is the liquid density. This ratio of acceleration-to-capillary forces is commonly referred to as the Bond number,  $Bo$  (Ref 9).

Masica et al (Ref 10) verified experimentally that the critical tube radius can be predicted from the  $Bo$  number. The critical number, delineating stability and instability of the interface, has a value of 0.84 for a totally-wetting liquid ( $\theta = 0^\circ$ ). The critical tube radius,  $R_c$ , may then be calculated as

$$R_c = 0.916 \left[ \frac{\sigma}{\rho a} \right]^{\frac{1}{2}}. \quad [10]$$

Bashforth and Adams, in 1883 (Ref 11), and Maxwell, in 1890 (Ref 12), conducted the first studies of the shape and stability of the liquid/gas interface. Bashforth and Adams developed a method for numerically solving the equation of capillarity and presented the results in rather voluminous tables as a function of fluid properties, gravitational acceleration, and contact angle. The first formal analysis of the stability of the interface between two fluids of different density was presented by Maxwell in his classic *Encyclopedia Britannica* article on capillary action (Ref 12). A review of this previous work is presented in Ref 8 and 13. The latter reference is an extension of NASA CR-92081, *The Literature of Low-g Propellant Behavior*, which was prepared by Lockheed Missiles and Space Company (LMSC) for NASA-MSD in 1967. The LMSC report primarily dealt with the literature from 1959 thru 1965. The Bowman review (Ref 13) covers 1966 to 1969.

Figure 13 shows the basic hydrostatic pore condition that was investigated in Martin Marietta's experimental program. The settling acceleration (a) was normal to the flat foraminous material, and was imposed as a sudden step-wise change from a normal 1-g acceleration to a low-g acceleration. This corresponds to a termination of an engine burn followed by a slight deceleration caused by vehicle drag. Drop tests were conducted under settling accelerations ranging from 0.0013 to 0.055 g. These tests were conducted in cylindrical transparent tanks containing test liquids that simulated a wide range of propellants.

## B. EXPERIMENTAL APPARATUS

Two test specimens (see Fig. 14) were mounted on the inner-capsule test platform in view of the 16-mm movie camera (see Fig. 15) for each drop. Each specimen consisted of two 5½-in.-O.D. transparent cylinders, a perforated-plate or square-weave-screen barrier, aluminum end plates, and tie rods. The longer (6-in.) cylinder served as the bottom portion of the 10-in. specimen and was filled with liquid to provide a 6-in. hydrostatic head for the barrier during the test. The cylinder above the barrier was 4 in. long. For the initial tests, Plexiglas cylinders (¼ in. wall thickness) were used.



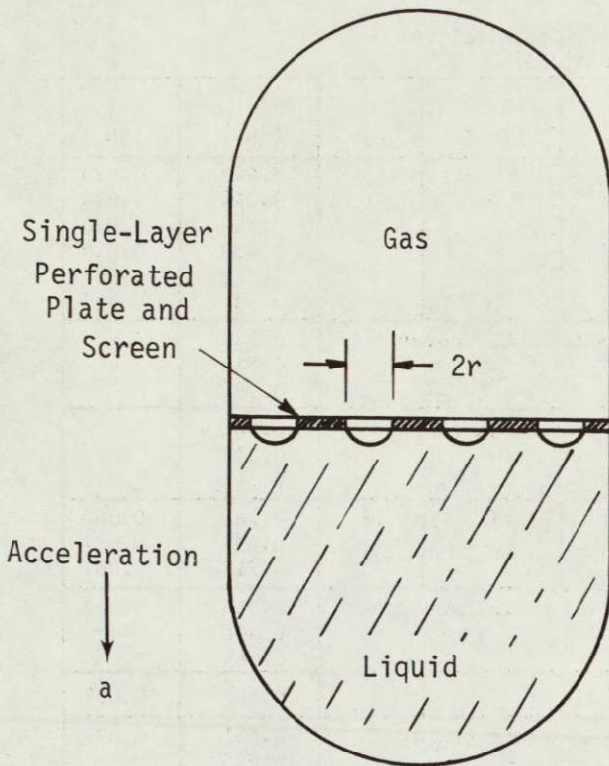


Fig. 13 Basic Hydrostatic Pore Stability Condition Investigated

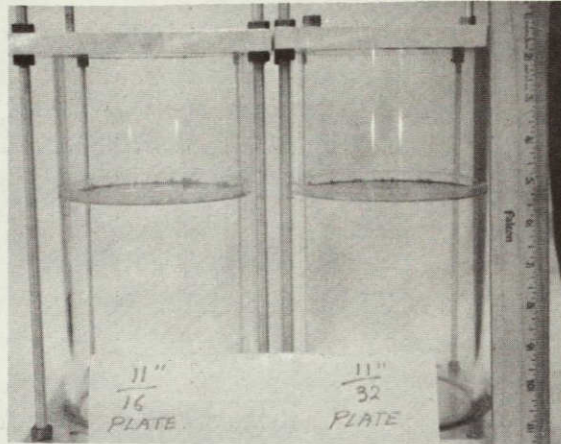


Fig. 14 Cylindrical Test Specimens

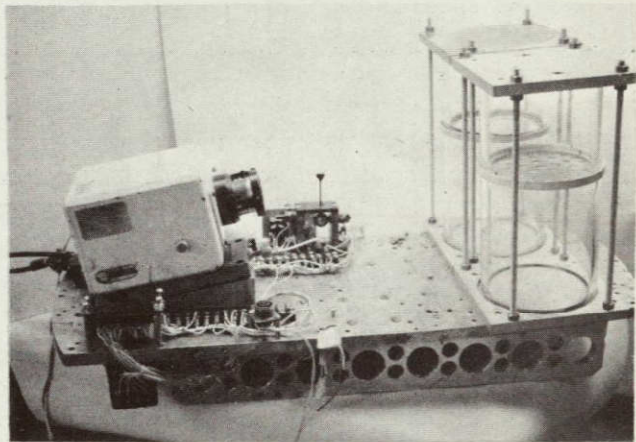


Fig. 15 Typical Test Setup

Contrary to the results noted in a pretest material-compatibility investigation, both Freon-TF and carbon tetrachloride severely attacked the Plexiglas cylinders and rendered them unfit after only one test (the etching action on the inner walls made the cylinders opaque). As a result, Pyrex cylinders were used for the major portion of the program. Flat gaskets made from rubber, Viton A\*, and Dow Corning's Aerospace Sealant were used to seal the cylinders and mating surfaces. The tie rods provided the compressive force to effect the seal.

Fifty-two barriers (39 plates and 13 screens) were used. Pertinent dimensions of these barriers are presented in Tables 2 and 3. The first set of perforated plates was made from stainless steel; all others were aluminum. The latter material was preferred because it has better machinability and allows closer hole toler-

\*Trade name for material made by E. I. duPont de Nemours & Co, Inc, Wilmington, Delaware.



Table 2 Perforated Plate Barrier Specifications  
(see Fig. 18 for Nomenclature)

PLATE NO.	MATERIAL*	R <sub>1</sub> (in.)	N <sub>1</sub>	R <sub>2</sub> (in.)	N <sub>2</sub>	R <sub>3</sub> (in.)	N <sub>3</sub>	d (in.)	T (in.)
1	S.S.	1.38	8					0.688	0.020
2	S.S.	0.80	8	1.37	8	2.05	8	0.344	0.020
3	S.S.	1.64	8					0.812	0.020
4	S.S.	0.81	8	1.65	8			0.438	0.020
5	S.S.	1.93	8					1.062	0.020
6	S.S.	1.05	8	2.11	8			0.531	0.020
7	Al	Has three pore sizes. Largest pore is in center (see Fig. 16).						0.344 0.313 0.281	†
8	Al	Has three pore sizes. Smallest pore is in center (see Fig. 16).						0.281 0.313 0.344	§
9	Al	0.56	6	1.12	12	1.70	18	0.281	0.087
10	Al	0.88	6	1.77	12			0.437	0.087
11	Al	1.44	6					0.719	0.087
12	Al	Has three pore sizes. Largest pore is in center (see Fig. 16).						0.500 0.406 0.344	0.087
13	Al	1.00	6	2.00	12			0.500	0.087
14	Al	Has three pore sizes. Largest pore is in center (see Fig. 16).						0.681 0.625 0.562	0.087
15	Al	1.06	6	2.12	12			0.531	0.087
16	Al	Has three pore sizes. Largest pores (1.75 in. dia) are on inner hole circle. Pores on outer hole circle (3.75 in. dia) are alternately 0.0812 and 0.750 in. (see Fig. 16).						0.875 0.812 0.750	0.087
17	Al	1.35	6					0.625	0.087
18	Al	1.87	6					0.937	0.087
19	Al	0.62	6	1.25	12	1.88	18	0.313	0.087
20	Al	0.86	6	1.75	12			0.375	0.087
21	Al	0.81	6	1.62	12			0.406	0.087
22	Al	1.19	6	1.90	6			0.594	0.087
23	Al	1.12	6	2.00	12			0.562	0.087
24	Al	0.79	6	1.57	12	2.06	18	0.344	0.087
25	Al	0.94	6	1.88	12			0.469	0.087
26	Al	1.56	6					0.781	0.087
27	Al	1.74	6					0.969	0.087
28	Al	1.31	6					0.656	0.087
29	Al	1.62	6					0.812	0.087
30	Al	1.55	5					0.937	0.087
31	Al	1.37	6					0.687	0.087
32	Al	1.80	6					0.906	0.087
33	Al							3.406	0.087
34	Al							3.594	0.087
35	Al							2.156	0.087
36	Al							2.344	0.087
37	Al							2.593	0.087
38	Al							2.781	0.087
39	Al							4.562	0.120

\*Material abbreviations: S.S. = stainless steel;  
Al = aluminum.

†Five plates with same hole layout, but different thicknesses: 0.016, 0.032, 0.087, 0.125, and 0.190 in.

§Same thickness as in Plate 7.



Table 3 Square Weave Screen Barrier Specifications (See Fig. 17)

SCREEN NO.	MATERIAL	MESH	WIRE DIAMETER (in.)	OPENING WIDTH (in.)
S-1	Br	1	0.192	0.808
S-2	S.S.	5/8/2	0.120/0.080	0.505/0.420
S-3	S.S.	2¼/2½/2	0.080/0.080/0.105	0.364/0.320/0.395
S-4	S.S.	2¼	0.092	0.352
S-5	S.S.	1	0.162	0.838
S-6	S.S.	2	0.080	0.420
S-7	S.S.	2	0.092	0.408
S-8	S.S.	1	0.120	0.880
S-9	S.S.	5	0.041	0.159
S-10	S.S.	3½	0.080	0.206
S-11	S.S.	3	0.054	0.279
S-12	S.S.	2½	0.080	0.320
S-13	S.S.	5/8	0.080	0.505
*Material abbreviations: Br = brass; S.S. = stainless steel.				

ances. The holes in the plates were drilled and then reamed to the sizes listed in Table 2. The screen mesh sizes shown in the table are according to the screen manufacturer, Cambridge Wire Cloth Co, Cambridge, Maryland.

The screen and plate barriers are pictured in Fig. 16 thru 18 and are representative of the different hole patterns used in the program. These basic patterns and the dimensions presented in Tables 2 and 3 document the screen and plate specimens.

Three liquids -- methanol, carbon tetrachloride, and Freon-TF -- were selected because they simulate a wide range of propellants. The physical properties considered for similitude were the kinematic surface tension,  $\beta$ , and the liquid-to-solid contact angle,  $\theta$ . The values for the test liquids and propellants (see Table 1) show that the  $\beta$  range of the test liquids ( $4.15$  to  $10.1 \times 10^{-4}$   $\text{ft}^3/\text{sec}^2$ ) covers the oxidizers and extends into the fuels. This is true for both the cryogenics and noncryogenics. It does not cover the monopropellants, such as hydrazine ( $\beta = 22.3 \times 10^{-4}$   $\text{ft}^3/\text{sec}^2$ ).



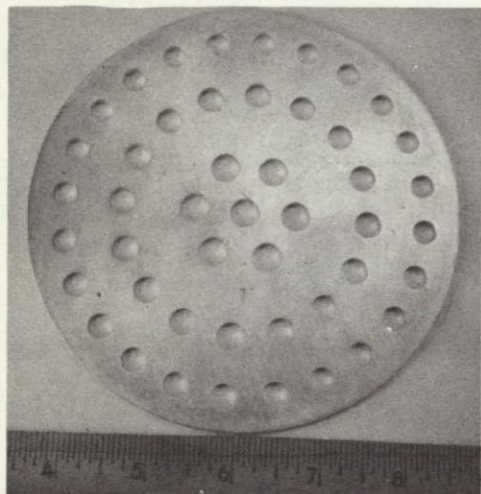


Plate 7

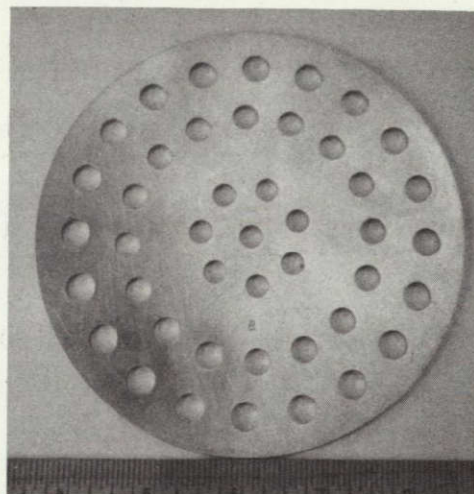


Plate 8

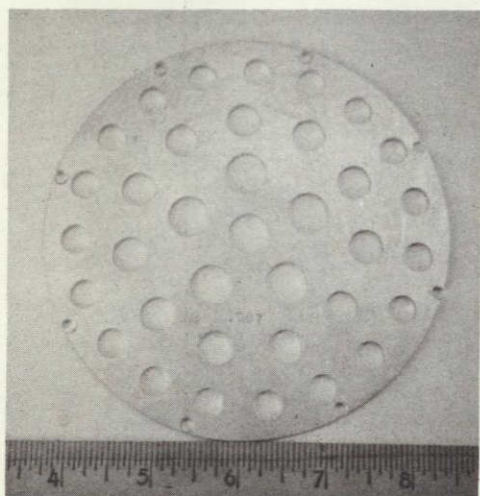


Plate 12

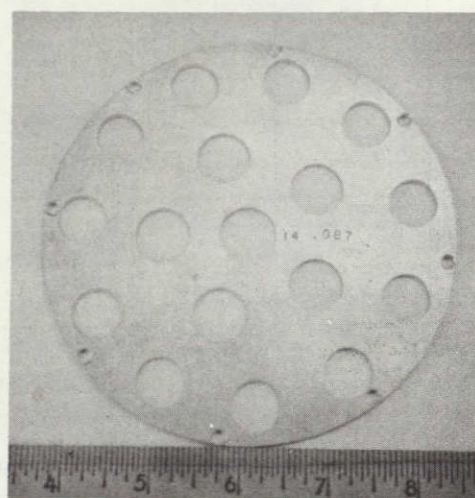


Plate 14

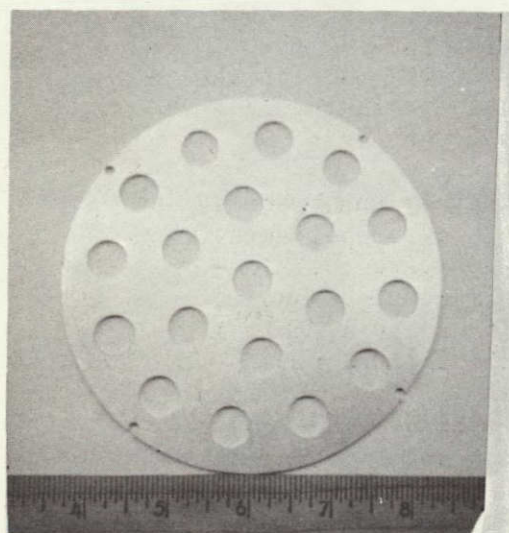


Plate 13

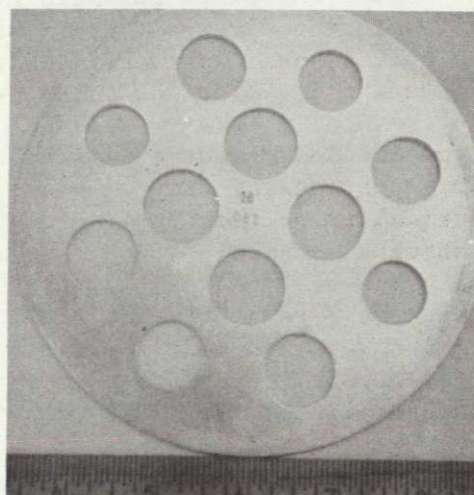
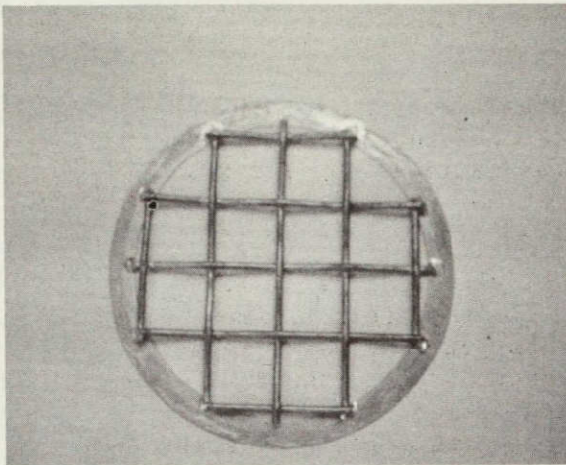
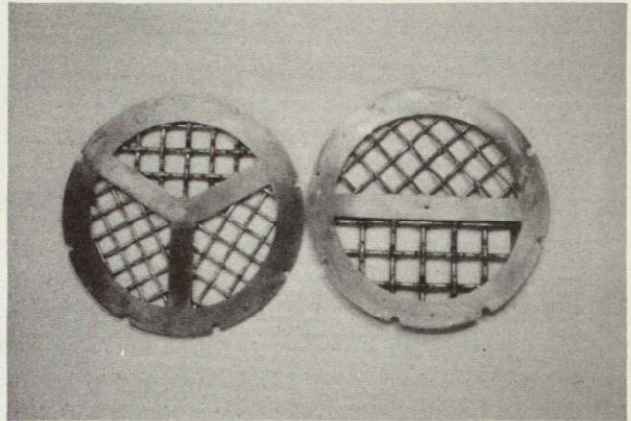


Plate 16

Fig. 16 Perforated Plate Barriers



S-8



S-3

S-2

Fig. 17 Typical Screen Barriers

Note:  $N$  = number of holes per hole circle.

Thickness  $\rightarrow$   $T$

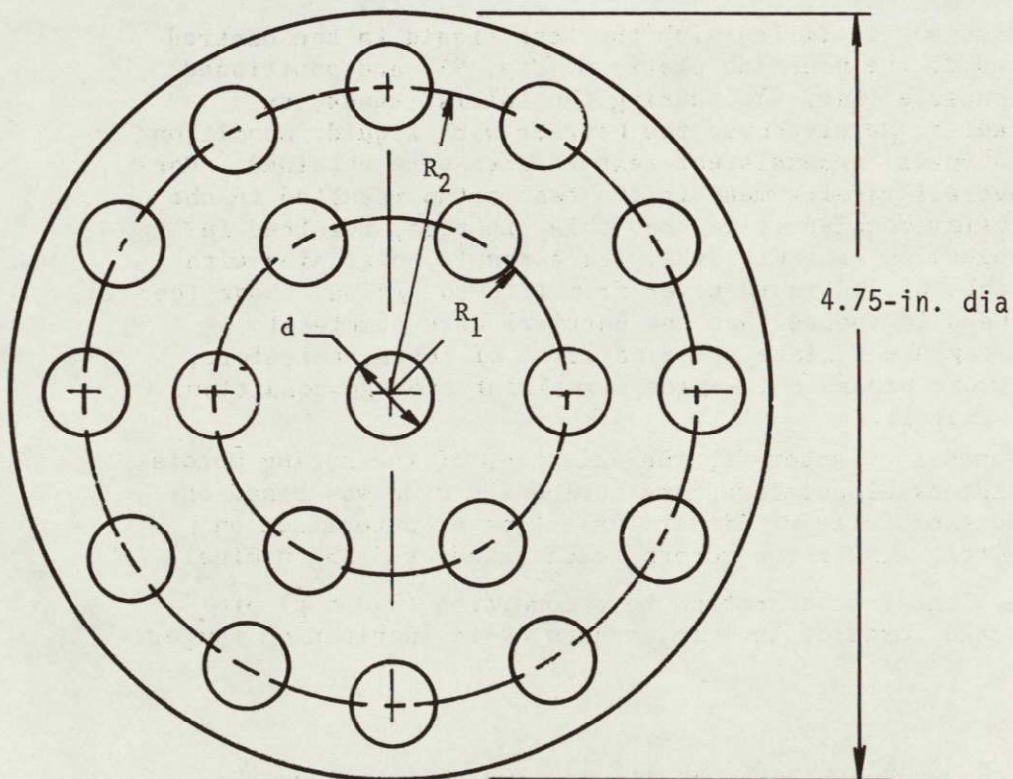


Fig. 18 Typical Hole Layout Pattern for Plates with Constant Hole Size (See Table 2)



Liquid propellants are essentially totally wetting ( $\theta = 0^\circ$ ) to aluminum, titanium, and stainless steel (Ref 14) -- materials commonly used for propellant tanks. Since Plexiglas and Pyrex cylinders were used in these tests to permit visual observation, only liquids with surface tensions less than  $2.67 \times 10^{-3} \text{ lb}_f/\text{ft}$  were selected to ensure wettability of the cylinders (Ref 15). This was the primary reason that monopropellants were not simulated; and although certain liquids, such as water or water-methanol mixtures, could cover the monopropellant  $\beta$  range, their higher surface tensions would make them nonwetting to the cylinders. Since the test liquids were wetting to the foraminous specimens, the test setup simulated the desired wetting condition of a propellant in a metal storage tank.

A small trace of dye was added to the test liquids to provide better photographic quality.

### C. TEST PROCEDURE

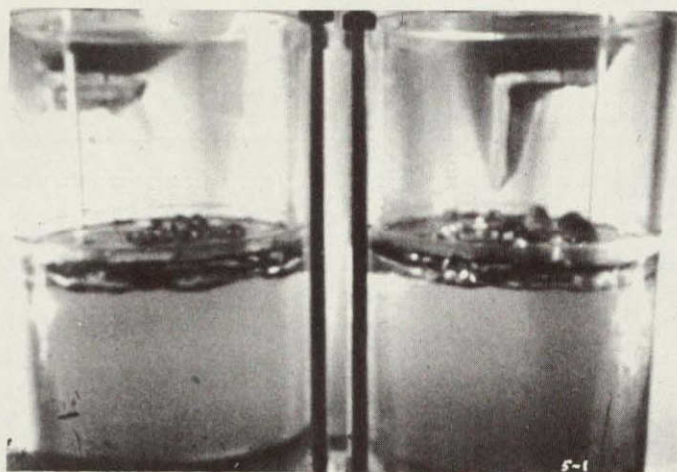
The specimens were filled with the test liquid to the desired level, attached to the mounting platform (Fig. 9), and positioned in the inner capsule (Fig. 8). During the initial tests, an attempt was made to merely cover the barrier with liquid, Condition (b) Fig. 11; however, inconsistent test results were obtained. For most drops, overall misalignment in the test setup resulted in the barriers not being completely wetted; this, in turn, resulted in massive gas ingestion (see Fig. 19). As a result, beginning with Run 7a (see Table 4), a liquid cover from 1/16 to 1/4 in. above the barrier\* was used to ensure that the barriers were completely wetted before capsule release. The majority of tests, therefore, simulated the more probable in-space propellant storage condition, Condition (a) Fig. 11.

As mentioned in Chapter II, the selection of the spring motors used to provide axial accelerations during the drop was based on their constancy of force vs linear deflection as determined on a tensile testor. The three motors (each rated at 5  $\text{lb}_f$  nominal) used for the highest acceleration test condition (0.055 g) provided an average force of 16.5  $\text{lb}_f$  over a 49-in. deflection range,

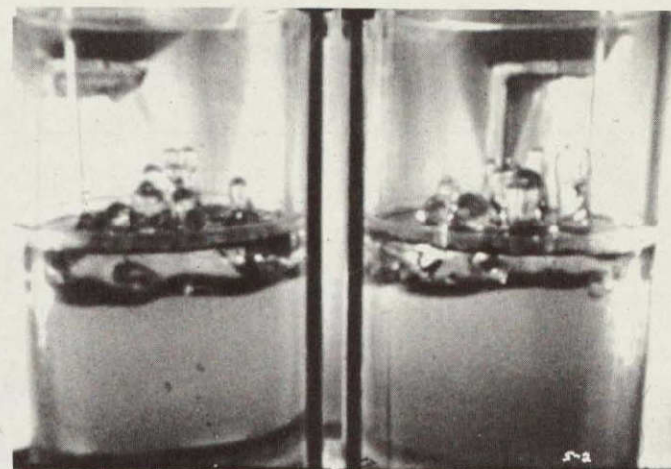
---

\*Two tests were made with the liquid level 1 in. above the barriers.

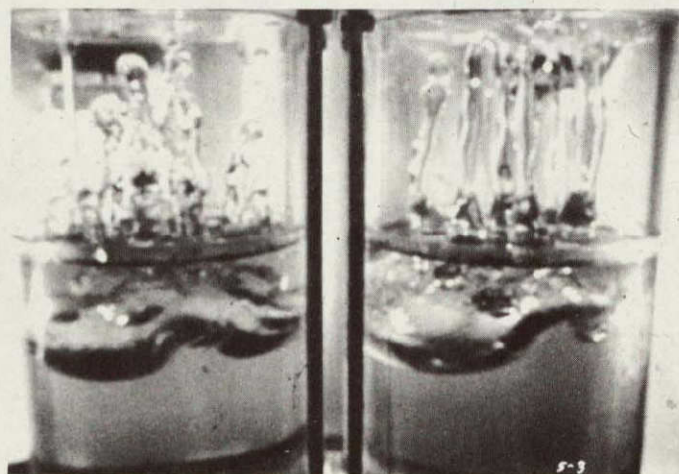




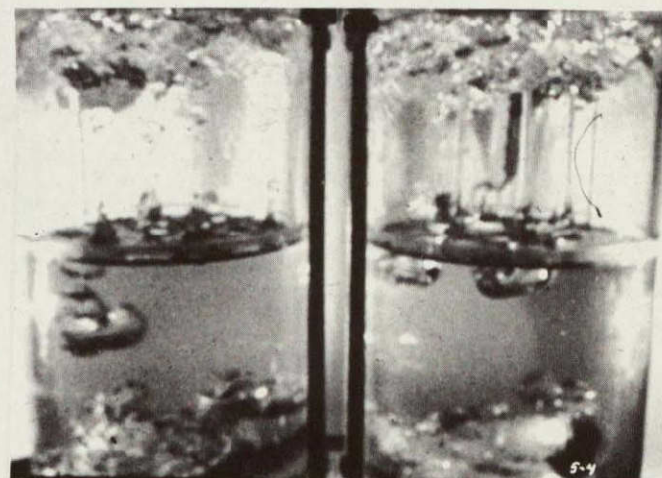
(a)  $\Delta t = 0.595$  sec



(b)  $\Delta t = 0.820$  sec



(c)  $\Delta t = 1.19$  sec



(d)  $\Delta t = 1.98$  sec

Fig. 19 Filmed Sequence of Run 2, Showing Pore Instability Due to Incomplete Wetting of Barriers



Table 4 Summary of Test Results  
(see Tables 2 and 3)

RUN NO.	LIQUID*	BARRIERS				BOND NO.†		STABILITY		ACCE- RATION, a/g
		LEFT CYLINDER		RIGHT CYLINDER		LEFT CYLINDER	RIGHT CYLINDER	LEFT CYLINDER	RIGHT CYLINDER	
		NO.	T (in.)	NO.	T (in.)					
1	F	1	0.020	2	0.020	3.19	0.792	No	No	0.051
2	F	1	0.020	2	0.020	3.26	0.805	No	No	0.051
2a	C	3	0.020	4	0.018	3.14	0.786	No	No	0.051
3a	M	5	0.020	6	0.020	3.16	0.802	No	Yes	0.051
4a	F	S-1	0.192	S-4	0.092	4.46	0.857	No	No	0.051
5a	C	S-5	0.162	S-6	0.080	3.36	0.846	No	No	0.051
6a	M	S-7	0.092	S-8	0.120	0.467	2.190	No	No	0.051
7a	F	1 <sup>5</sup>	0.020	2	0.020	3.26	0.802	No	Yes	0.051
8a	C	4 <sup>5</sup>	0.018	3	0.020	0.782	3.130	Yes	No	0.051
9a	M	6 <sup>5</sup>	0.020	5	0.020	0.802	3.160	No	No	0.051
10a	F	S-1 <sup>5</sup>	0.092	S-4	0.190	4.46	0.859	No	No	0.051
11a	C	S-6 <sup>5</sup>	0.080	S-5	0.162	0.815	3.36	No	No	0.051
12a	M	S-7 <sup>5</sup>	0.092	S-8	0.120	0.466	2.19	No	No	0.051
13a	M	7	0.032	8	0.032	0.331	0.222	Yes	Yes	0.051
						0.287	0.287	Yes	Yes	0.051
						0.222	0.331	Yes	Yes	0.051
14a	M	8	0.016	7	0.016	0.222	0.331	Yes	Yes	0.051
						0.287	0.287	Yes	Yes	0.051
						0.331	0.222	Yes	Yes	0.051
15a	M	8	0.087	7	0.087	0.222	0.331	Yes	Yes	0.051
						0.287	0.287	Yes	Yes	0.051
						0.331	0.222	Yes	Yes	0.051
16a	F	8	0.087	7	0.087	0.543	0.807	Yes	Yes	0.051
						0.675	0.675	Yes	Yes	0.051
						0.807	0.543	Yes	Yes	0.051
17a	F	8	0.016	7	0.016	0.543	0.807	Yes	Yes	0.051
						0.675	0.675	Yes	Yes	0.051
						0.807	0.543	Yes	Yes	0.051
18a	F	7	0.032	8	0.032	0.543	0.807	Yes	Yes	0.051
						0.675	0.675	Yes	Yes	0.051
						0.807	0.543	Yes	Yes	0.051
19a	C	7	0.032	8	0.032	0.561	0.378	Yes	Yes	0.051
						0.464	0.464	Yes	Yes	0.051
						0.378	0.561	Yes	Yes	0.051
20a	C	7	0.016	8	0.016	0.561	0.378	Yes	Yes	0.051
						0.464	0.464	Yes	Yes	0.051
						0.378	0.561	Yes	Yes	0.051
21a	C	7	0.087	8	0.087	0.561	0.378	Yes	Yes	0.051
						0.464	0.464	Yes	Yes	0.051
						0.378	0.561	Yes	Yes	0.051
22a <sup>¶</sup>	M	7	0.032	7	0.087	0.331	0.331	Yes	Yes	0.051
						0.287	0.287	Yes	Yes	0.051
						0.222	0.222	Yes	Yes	0.051
23a <sup>**</sup>	M	7	0.032	7	0.087	0.331	0.331	No	No	0.051
						0.287	0.287	No	No	0.051
						0.222	0.222	No	No	0.051
24a <sup>¶</sup>	F	7	0.032			0.807	0.807	No	No	0.051
						0.675	0.675	No	No	0.051
						0.543	0.543	No	No	0.051
26a	M	7	0.125	7	0.190	0.331	0.331	Yes	Yes	0.051
						0.287	0.287	Yes	Yes	0.051
						0.222	0.222	Yes	Yes	0.051
27a	M	7	0.125	7	0.190	0.331	0.331	Yes	Yes	0.051
						0.287	0.287	Yes	Yes	0.051
						0.222	0.222	Yes	Yes	0.051
28a	F	7	0.125	7	0.190	0.807	0.807	Yes	Yes	0.051
						0.675	0.675	Yes	Yes	0.051
						0.543	0.543	Yes	Yes	0.051
29a	M	12	0.087	14	0.087	0.331	0.874	Yes	Yes	0.051
						0.460	1.085	Yes	Yes	0.051
						0.695	1.325	Yes	Yes	0.051
30a	F	12	0.087	14	0.087	0.805	2.115	No	No	0.051
						1.110	2.560	No	No	0.051
						1.650	3.220	No	No	0.051
30b	F	12	0.087	14	0.087	0.805	2.115	No	No	0.051
						1.110	2.560	No	No	0.051
						1.650	3.220	No	No	0.051
30c	F	12	0.087	14	0.087	0.805	2.115	No	No	0.051
						1.110	2.560	No	No	0.051
						1.650	3.220	No	No	0.051
30d	F	12	0.087	14	0.087	0.805	2.115	No	No	0.051
						1.110	2.560	No	No	0.051
						1.650	3.220	No	No	0.051
30e	F	12	0.087	14	0.087	0.805	2.115	No	No	0.051
						1.110	2.560	No	No	0.051
						1.650	3.220	No	No	0.051
30f	F	12	0.087	14	0.087	0.805	2.115	No	No	0.51
						1.110	2.560	No	No	0.051
						1.650	3.220	No	No	0.051
30g	F	12	0.087	14	0.087	0.805	2.115	No	No	0.051
						1.110	2.560	No	No	0.051
						1.650	3.220	No	No	0.051
30h	F	12	0.087	14	0.087	0.805	2.115	No	No	0.051
						1.110	2.560	No	No	0.051
						1.650	3.220	No	No	0.051
31a	C	12	0.087	14	0.087	0.560	1.490	Yes	No	0.051
						0.780	1.855	Yes	No	0.051
						0.885	2.245	Yes	No	0.051



Table 4 (concl)

RUN NO.	LIQUID*	BARRIERS				BOND NO. <sup>†</sup>		STABILITY		ACCELERATION, a/g
		LEFT CYLINDER		RIGHT CYLINDER						
		NO.	T (in.)	NO.	T (in.)	LEFT CYLINDER	RIGHT CYLINDER	LEFT CYLINDER	RIGHT CYLINDER	
31b	C	12	0.087	14	0.087	0.560 0.780 0.885	1.490 1.855 2.245	Yes Yes Yes	No No No	0.051 0.051 0.051
31c	C	12	0.087	14	0.087	0.560 0.780 0.885	1.490 1.855 2.245	No No No	No No No	0.051 0.051 0.051
31d	C	12	0.087	14	0.087	0.560 0.780 0.885	1.490 1.855 2.245	Yes Yes Yes	No No No	0.051 0.051 0.051
32a	M	S-3	0.080 0.080 0.105	S-2	0.120 0.080	0.369 0.285 0.432	0.710 0.494	Yes Yes Yes	Yes Yes Yes	0.051 0.051 0.051
33a	F	S-3	0.080 0.080 0.105	S-2	0.120 0.080	0.895 0.695 1.052	1.750 1.210	No No No	No No No	0.051 0.051 0.051
34a	C	S-3	0.080 0.080 0.105	S-2	0.120 0.080	0.624 0.484 0.744	1.220 0.840	No No No	No No No	0.051 0.051 0.051
35	C	14	0.190	14	0.032	1.485 1.855	1.485 1.855	No No	No No	0.051 0.051
36	F	12	0.190	12	0.032	0.805 1.108	0.805 1.108	No No	No No	0.051 0.051
37	F	12	0.032	12	0.190	0.870 1.192	0.870 1.192	No No	No No	0.055 0.055
38	F	12	0.032	12	0.190	0.870	0.870	No	No	0.055
39	F	8	0.087	12	0.190	0.584 0.675	0.870	Yes Yes	No No	0.055 0.055
40	M	16	0.087	18	0.087	1.640 1.990 2.310	2.640	No No No	No No No	0.055 0.055 0.055
41	M	11	0.087	13	0.087	0.890	0.745	Yes	Yes	0.055
42	F	9	0.087	10	0.087	0.577	2.520	Yes	No	0.055
43	C	21	0.087	22	0.087	0.845	1.805	No	No	0.055
44	M	15	0.087	17	0.087	0.858	1.178	No	No	0.055
45	F	19	0.087	20	0.087	0.726	1.040	Yes	No	0.055
46	C	10	0.087	23	0.087	0.985	1.624	No	No	0.055
47	M	21	0.087	22	0.087	0.962	1.074	No	No	0.055
48	F	24	0.087	21	0.087	0.872	1.30	No	No	0.055
49	C	25	0.087	15	0.087	1.122	1.450	No	No	0.055
50	M	26	0.087	27	0.087	0.666	1.034	Yes	Yes	0.020
51	F	25	0.087	28	0.087	0.578	1.132	Yes	No	0.020
52	C	15	0.087	11	0.087	0.570	1.030	Yes	Yes	0.020
53	M	29	0.087	30	0.087	0.716	0.970	Yes	Yes	0.020
54	F	13	0.087	17	0.087	0.645	1.041	Yes	Yes	0.020
55	C	23	0.087	31	0.087	0.642	0.963	Yes	Yes	0.020
56	M	11	0.087	32	0.087	0.815	0.939	Yes	Yes	0.020
57	F	15	0.087	22	0.087	0.839	0.941	Yes	No	0.020
58	C	22	0.087	28	0.087	0.708	0.880	Yes	Yes	0.020
65	M	33	0.087	34	0.087	0.899	1.008	Yes	Yes	0.0014
66	F	35	0.087	36	0.087	0.864	0.996	Yes	Yes	0.0014
67	C	37	0.087	38	0.087	0.880	1.015	Yes	Yes	0.0014
77	F	S-12	0.080	S-11	0.054	0.680	0.505	No	No	0.0483
77a	F	S-9	0.041	S-10	0.080	0.164	0.254	Yes	Yes	0.0483
78	C	S-12	0.080	S-7	0.092	0.473	0.752	No	No	0.0483
78a	C	S-6	0.080	S-4	0.092	0.792	0.565	No	No	0.0483
79	M	S-5	0.162	S-1	0.192	1.870	1.750	No	No	0.0483
79a	M	S-13	0.080	S-6	0.080	0.677	0.466	No	No	0.0483
80	F	S-5	0.162	S-1	0.192	1.655	1.540	No	No	0.0175
80a	F	S-13	0.080	S-6	0.080	0.596	0.415	No	Yes	0.0175
81	C	S-1	0.192	S-5	0.162	1.540	1.655	No	No	0.0175
81a	C	S-6	0.080	S-13	0.080	0.289	0.416	Yes	Yes	0.0175
83	M	33	0.087	39	0.120	0.810	1.460	Yes	No	0.00127

\*Liquid designation: F = Freon T. F.; C = Carbon Tetrachloride; M = Methanol.

<sup>†</sup>Bond numbers listed are based on pore radius.<sup>§</sup>The barriers used for these tests were coated with a thin film of Teflon.<sup>§</sup>Liquid level was initially 1.0 in. above the plate.<sup>\*\*</sup>Liquid level was initially 1.0 in. below the plate.



which corresponded to the relative travel between the capsules during the test. Their force variation was less than  $\pm 0.25 \text{ lb}_f$ .

The two motors (each rated at  $3 \text{ lb}_f$  nominal) used for the mid-range acceleration condition ( $0.02 \text{ g}$ ) provided an average force of  $6.0 \text{ lb}_f$ , and the variation was less than  $\pm 0.25 \text{ lb}_f$  over a deflection range of 24 in. The single  $0.375\text{-lb}_f$  (nominal) motor used for the lowest acceleration condition ( $0.0013 \text{ g}$ ) provided an average force of  $0.435 \pm 0.015 \text{ lb}_f$  over its 6-in. deflection range.

The calibrations were made at a deflection rate of 10 in. per minute, or about one order of magnitude less than that for the drops; however, based upon previous test experience, the calibration results are applicable. The motors were checked between drops by using a simple spring scale to determine if any gross changes in operating characteristics had occurred.

Low-g initiation and termination were signalled by flash bulbs positioned in the test cell in view of the 16-mm camera. A check on the average acceleration of the inner capsule for the entire drop interval was provided by the total low-g time and relative travel of the capsules. The axial acceleration occurring during the initial tests was verified by using a simple caged-ball device attached to the mounting platform (see Fig. 20). The vertical travel vs time for a single 0.813-in. steel ball was measured on a CEC Model 5-123 recorder. The parallel tie rods served as guide rails and restrained the ball from moving in any direction except vertically. As the ball passed between the light source and the diode, it interrupted the current flowing in separate photodiode circuits. Successive graphical differentiations of the drop distance vs drop time showed that the axial acceleration was near-constant\* during the drop interval.

---

\*As discussed on p 13 of MCR-67-247 (Issue 4), *Monthly Progress Report for October 1967*, a second-order polynomial resulted in the best curve fit. The accelerations determined in this manner were within  $\pm 7\%$  of those calculated using the average spring force and the mass of the test cell. The deviations between the measured distances and the distances calculated using the polynomial ranged from 0.15 to 0.50%, which tends to indicate that the axial acceleration was nearly constant.



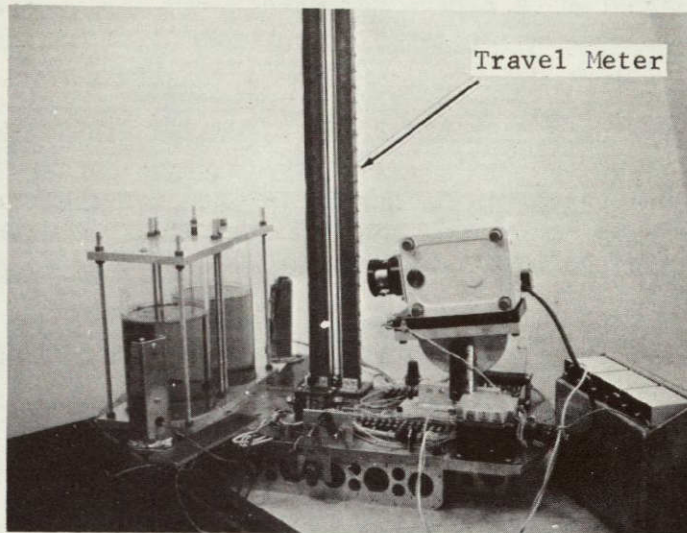


Fig. 20 Drop Test Setup, Showing Vertical Ball Travel Meter

The general test plan was to determine the critical pore size at nominal settling accelerations ranging from 0.0013 to 0.055 g. This acceleration range was dictated by the limitations of the drop test. The plan was to test a stable barrier in one cylindrical specimen while testing an unstable barrier for the same liquid in the other cylinder. Subsequent tests were then made after reducing the pore sizes in the unstable plate and enlarging the holes in the stable plate. The minimum change in hole size was selected as 1/32 in. The tests were to continue in this manner until the critical size was determined.

#### D. EXPERIMENTAL RESULTS

In all, 77 drop tests were made -- 14 to evaluate the pore stability of various square-weave screens and 63 to evaluate the effect of different plate configurations.

The test results are summarized in Table 4. The foraminous barriers and test liquids are listed for each test. The average acceleration level calculated from the average NEG'ATOR spring force and the mass of the test cell, the stability results, and the Bo numbers are also presented. The Bo numbers shown for the perforated plates are based upon the pore radius; and those for the square-weave screens, on half of the open dimension. The physical property data listed in Table 1 were used for the three test liquids and were not corrected to compensate for temperature and pressure. The average accelerations listed were used to calculate the Bo numbers.

The interface stability criteria used to evaluate the test results were that the pore was stable:

- 1) When no gas was ingested through the barrier during the drop interval; or
- 2) When the liquid-gas interface configuration showed no time-dependence during the drop interval.

The first criterion was used for the higher acceleration test conditions; the second, for the lowest acceleration test condition.

The test results for bare, uncoated, perforated-plate barriers are presented in Fig. 21. The pore radii tested are plotted against the ratio of kinematic surface tension ( $\beta$ )-to-average acceleration.

The straight line shown on the plot tends to separate the stable and unstable regions, and is based on a Bo number of 0.84 (based on pore radius). There is some experimental scatter, particularly at the lowest acceleration test condition of 0.0013 g; however, the data show good verification of the Bo number criterion for pore stability and also fairly good agreement with the critical Bo number value of 0.84.

The stability data for the square-weave screens are presented similarly in Fig. 22. As mentioned earlier, considerably fewer tests were conducted for screens, and the results are less conclusive than those for the perforated plates. Again, the data tend to verify the Bo number criterion, but the critical Bo number is considerably less than the value for perforated plates. A value of 0.450, based on one-half the screen opening, is indicated. The pore size, as presented in Fig. 22, is one-half the opening width of the square-weave screens.



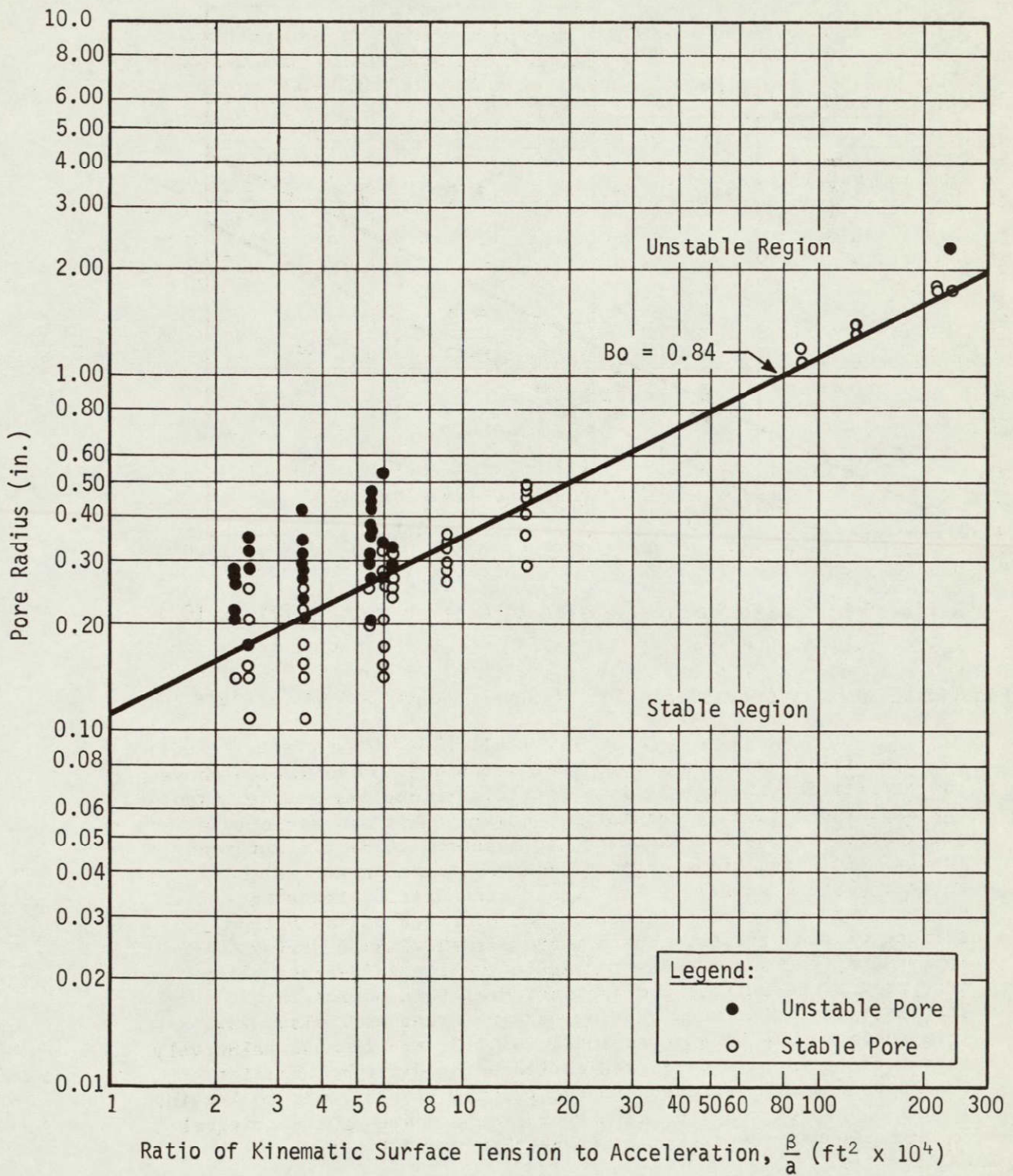


Fig. 21 Stability Characteristics of Perforated Plate Barriers

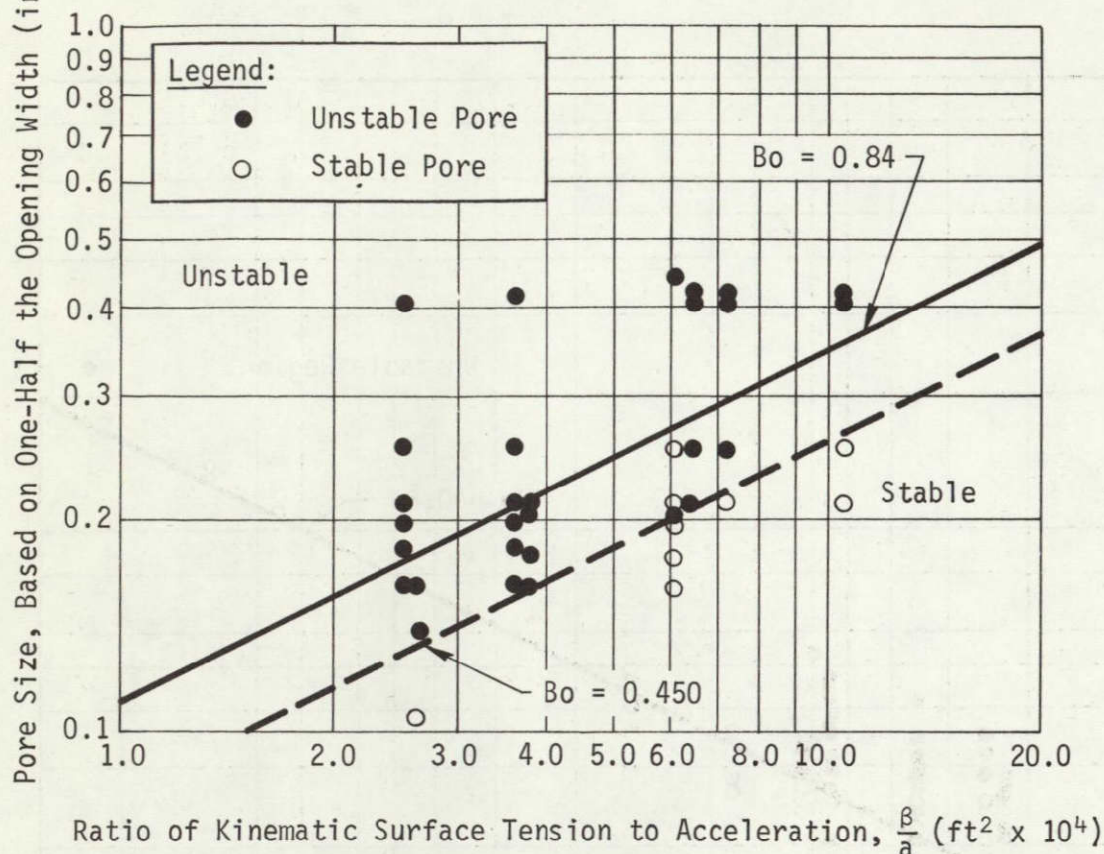


Fig. 22 Stability Characteristics of Square Weave Screen Barriers

The filmed results showed that the liquid accumulation above the barrier for the stable interface conditions was greater than the amount provided by the initial cover. This was strictly a qualitative evaluation; however, it appeared to be a consistent result. This additional liquid appeared to be greater with thicker plates, as well. The liquid accumulation tends to suggest that the stable interface was provided at the bottom surface of the barrier. The momentum of the liquid during emptying of the pores tends to reduce the liquid/gas stability criterion since surface tension must damp this motion to stabilize the interface. Viscous shear forces will also slow this motion. The data presented in Fig. 21 and 22 show relatively good correlation, as discussed earlier, for different barrier thicknesses and a variation in the initial liquid cover to 1/4-in. It was concluded that the effect of liquid cover on the critical  $Bo$  number under the axisymmetric settling conditions was negligible.



Two tests, Runs 22a and 24a (see Table 4), were made with the initial liquid level 1 in. above the barrier. The results for Run 22a are pictured in Fig. 23. Both plates were stable at a Bo number of 0.331. Run 22a was the only valid test for a liquid cover greater than 1/4-in. For Run 24a, a sidewise force was observed during the drop and the gas ingestion was indicative of interface instability under a lateral acceleration. Breakdown was along one edge of the plates only.

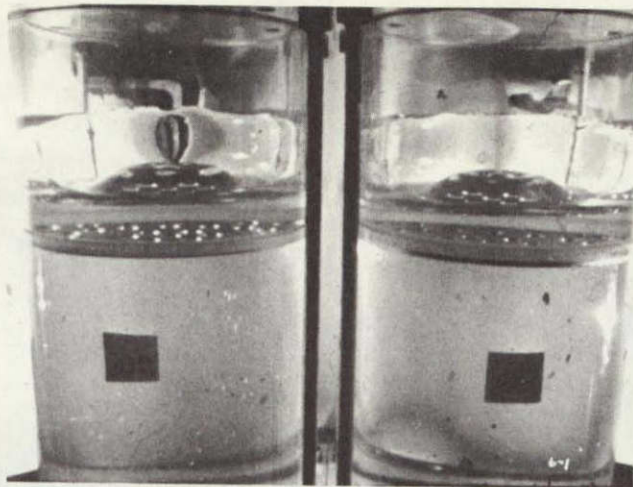
The motion of the liquid above the barrier was similar to that studied by Dr. T. E. Bowman during the CLEO Program. Liquids tended to settle to the top of the test specimens by flowing along the wall and by moving in a central liquid column or dome. The latter formation at the higher low-g conditions resulted in liquid covering the central portion of the barriers. Breakdown or pore instability, in general, occurred only in the pores in the largest pore circle (nearest the wall). Consequently, plates such as No. 7 and 8 (see Table 2), which had different pore sizes, did not provide the results desired (the growth and existence of the liquid dome prevented gas-liquid interfaces at the pores in the central region of the plate) and instead of obtaining test data for three different Bo numbers for each plate, we only obtained stability data for the pores on the outer circle.

Tests were also conducted to assess the effect on pore stability of: (1) low-surface-energy coatings; (2) plate thickness-to-hole size ratio; and (3) liquid depth beneath the barrier (hydrostatic head).

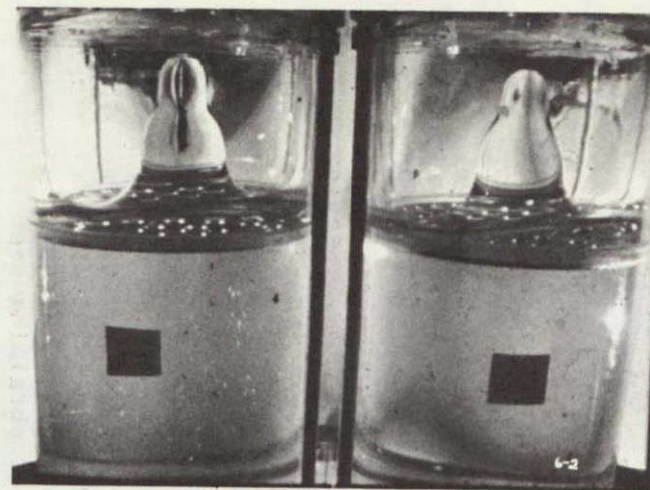
The effect of a Teflon coating on the performance of plate and screen barriers was briefly investigated during Tests 7a thru 12a. A 0.001-in.-thick coat of Teflon was applied to the barriers. Two forms of application were used. A Teflon resin, E. I. duPont 850-204, requiring a bake period of 4 hr, was applied to the barriers used in Tests 7a and 9a. A fluorocarbon spray coating, Miller-Stephenson Chemical Co M.S. 122, was applied to the barriers used in Run 8a and Runs 10a thru 12a.

The results of these tests were inconclusive. A comparison of the results from Runs 2a and 8a seems to indicate that the Teflon coating promoted stability (see Fig. 24). Barrier #4 was stable with the Teflon coating and unstable without. The Bo was 0.786 (unstable) and 0.782 (stable). (The slight difference in the Bo values was due to a difference in test cell mass.)

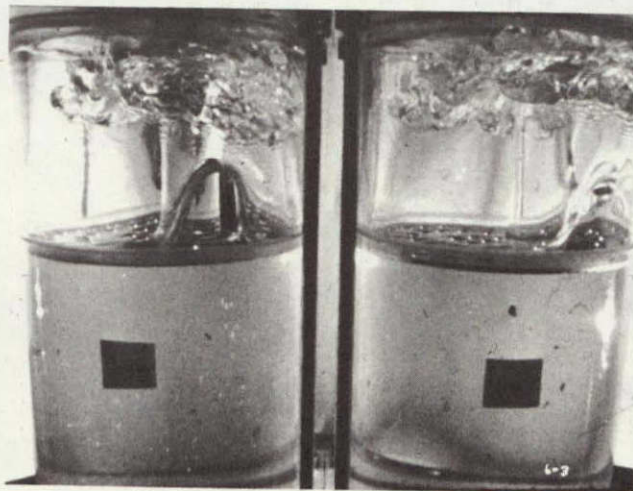




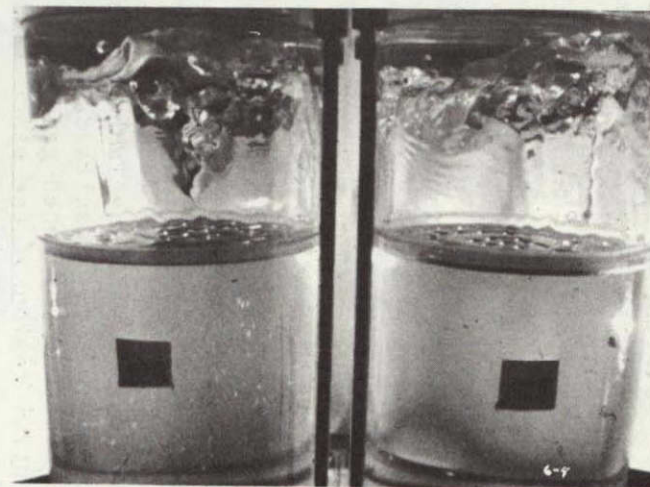
(a)  $\Delta t = 0.440$  sec



(b)  $\Delta t = 0.820$  sec

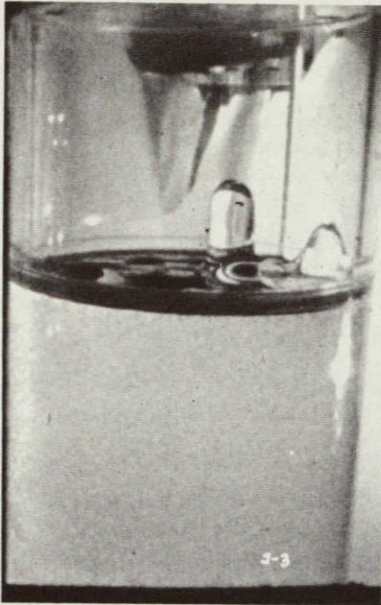
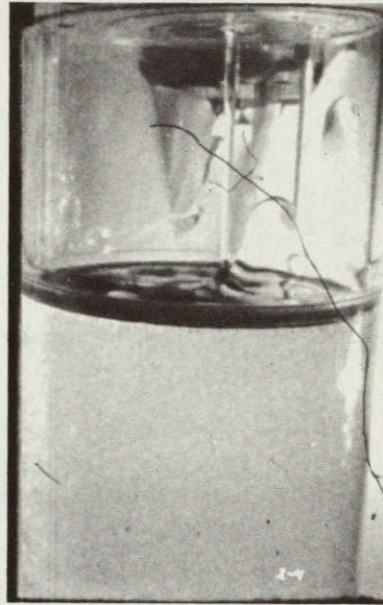


(c)  $\Delta t = 1.22$  sec

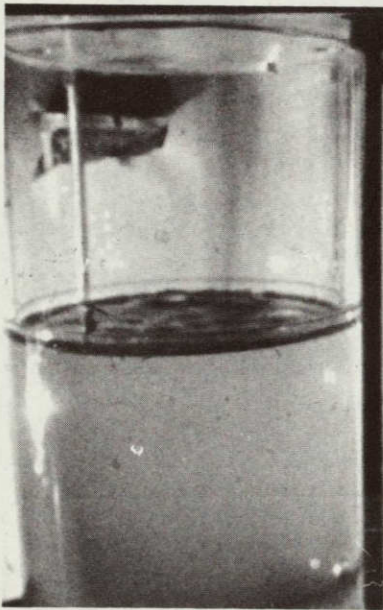
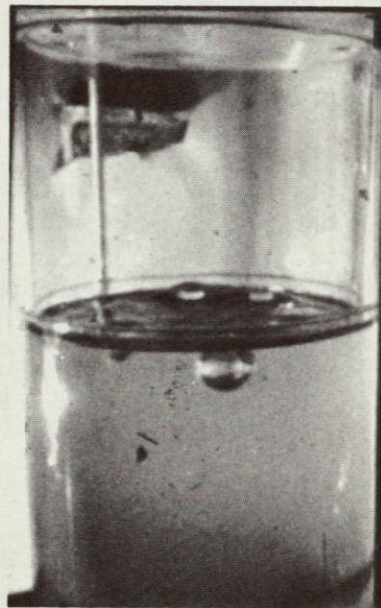


(d)  $\Delta t = 1.81$  sec

Fig. 23 Sequence Showing Pore Stability from Run 22a

 $\Delta t = 1.31 \text{ sec}$  $\Delta t = 1.91 \text{ sec}$ 

(a) Run 8a -- Teflon-Coated Barrier #4  
(Pore Stability)

 $\Delta t = 1.45 \text{ sec}$  $\Delta t = 2.04 \text{ sec}$ 

Run 2a -- Bare (Uncoated) Stainless Steel Barrier #4  
(Pore Instability)

Fig. 24 Test Results from Runs 2a and 8a  
(Test liquid is  $\text{CCl}_4$  and acceleration  
level is 0.051-g).



The results from Runs 3a and 9a showed that stability occurred when plate #6 was uncoated ( $Bo = 0.802$ ), but that instability occurred at the same  $Bo$  value when the same plate was coated. This contradicts the results for Runs 2a and 8a. (All of the screen samples tested, both with and without coatings, were unstable.) Since only a few tests were made with low-surface-energy coatings, no conclusions may be drawn; however, since Teflon coatings showed no definite improvement, their use is not recommended.

The effect of different plate thickness-to-pore size ratios on interface stability was evaluated in several tests using Plates 7 and 8. These plates had the same three pore sizes (0.281, 0.313, and 0.344 in.), but different plate thicknesses (0.016, 0.032, 0.087, and 0.190 in.). The different plate thickness-to-pore size ratios did not noticeably affect the interface stability. However, the amount of liquid that accumulated above the barriers during stable conditions was greater with the thicker plates. This result tends to support the conclusion stated earlier that the liquid-gas interface formed at the bottom surface of the plates. This interface location was further supported by the test results which showed that the thicker plates required more time to break down. As an example, for Run 35, the thicker plate (0.190 in.) appeared to break down after about 1.15 sec, whereas the thinner plate (0.032 in.) broke down at approximately 0.90 sec. The  $Bo$  condition was the same for both plates, Table 4.

A 6-in. hydrostatic head was provided for all runs except Runs 37, 38, and 39; for these runs, the head was 4 in. No effect due to the hydrostatic head was observed. The zero ullage condition provided in these tests is similar to the  $P_1 = P_v$  case for the capped tubes discussed earlier in Section A of this chapter. Before vaporization of liquid will occur for the low-g test conditions, the hydrostatic head must be on the order of hundreds of feet (of test liquid).

#### E. DISCUSSION OF RESULTS

The procedure for the drop tests called for a near-instantaneous transition from one g (positive) to an axial, low-g (negative) con-



dition.\* Since the resulting impulse tends to cause the liquid beneath the foraminous barriers to settle through the flat barriers to the opposite end of the tank, these tests simulated the condition that occurs following an engine shutdown, except that the change in acceleration produced during the tests occurs much faster than it would in space. For example, the thrust of the Titan Transtage's main engine tails off over a 1-sec interval, and typically decays from 16,000 to 2,000 lb<sub>f</sub> during the initial 0.4 sec. In the drop tests, however, the capsule is released by shearing a bolt that supports the capsule package; this causes a near-instantaneous change in acceleration that tends to interact with possible fluid motion caused by liquid-compression and structural-relaxation phenomena and minimize pore stability.

Compressing a liquid is analogous to compressing a spring. If a compressed liquid is released quickly, potential energy is transformed entirely to kinetic energy and the liquid jumps. However, if the liquid is released more slowly, it tends to adjust to the changing force, and merely expands. This second phenomenon, structural relaxation, results when a load-bearing material deflects and attains a new equilibrium position.

In the hydrostatic stability tests, both phenomena tend to cause unwanted initial motion in the test fluid. The films of the tests, however, showed that there was little or no fluid motion during the early phases of each drop. This is because the test liquids have relatively short compression-response times and correspondingly small maximum velocities (on the order of 0.5 msec and 0.09 in./sec, respectively), based on the analytical method outlined in Ref 16. Furthermore, the drop-capsule hardware was built to minimize relaxation effects (Ref 17), and the foraminous barriers (see Tables 2 and 3) and the thick-walled ( $\frac{1}{4}$  in.) cylindrical specimens were also relatively stiff and rigid.

The magnitude of the acceleration change (1 g) recorded during the drop tests corresponds to that occurring in space, again based on Transtage data. (The Transtage has a mass of 28,000 lb<sub>m</sub> when loaded and a mass of 5,000 lb<sub>m</sub> at burnout. Its acceleration is, therefore, on the order of 0.57 to 3.2 g during an engine burn.)

---

\*The terms positive and negative are used to denote the direction of the acceleration vector. Negative accelerations tend to relocate liquid from beneath the barrier to the opposite end of the cylindrical specimen, whereas positive accelerations act in the opposite direction and tend to prevent liquid from passing through the barrier.



The liquid-settling flow regimes observed during the test program tend to substantiate the axisymmetric case. For the majority of the tests, the motion of the liquid was symmetrical, which tends to suggest that the accelerating force was axisymmetric (to within  $1^\circ$ ), based upon the liquid-resettling results obtained under Contract NAS8-11328 for the CLEO Program. (During this latter program, off-axis accelerations of  $1^\circ$  caused definite unsymmetric liquid motion during resettling.)

The method suggested in Ref 18 for single-sample experiments was used to estimate the reliability of the test results.

The Bo number can be determined from

$$Bo = \frac{\rho f_N r^2}{M \sigma}, \quad [11]$$

where  $\rho$  is the density of the liquid,  $f_N$  is the average NEG'ATOR spring force,  $r$  is the pore radius,  $M$  is the mass of the drop capsule, and  $\sigma$  is the surface tension at the liquid-vapor interface.

Equation [12] was used to estimate the accuracy of the Bo number:

$$w_{Bo} = \left[ \left( \frac{\partial Bo}{\partial \sigma} w_\sigma \right)^2 + \left( \frac{\partial Bo}{\partial M} w_M \right)^2 + \left( \frac{\partial Bo}{\partial r} w_r \right)^2 + \left( \frac{\partial Bo}{\partial f_N} w_{f_N} \right)^2 + \left( \frac{\partial Bo}{\partial \rho} w_\rho \right)^2 \right]^{1/2}, \quad [12]$$

where  $w$  is the uncertainty interval, plus or minus, associated with the Bo number and the variables in Eq [11]. Equation [12] is valid only when the uncertainties associated with each variable are based upon the same odds. The uncertainties for the variables in Eq [11] are presented for various low-g test conditions in Table 5, and are based upon probable odds of 20:1. In other words, the best value for each variable is the average value, and the odds are 20:1 that the true value lies within the uncertainties listed in this table.

A partial differentiation of Eq [11] with respect to each of the variables, and a subsequent non-dimensionalization of Eq [12] by dividing it by the Bo number yields

$$\frac{w_{Bo}}{Bo} = \left[ \left( \frac{w_\sigma}{\sigma} \right)^2 + \left( \frac{w_M}{M} \right)^2 + \left( \frac{2w_r}{r} \right)^2 + \left( \frac{w_{f_N}}{f_N} \right)^2 + \left( \frac{w_\rho}{\rho} \right)^2 \right]^{1/2}. \quad [13]$$

Table 5 Pertinent Variables and Their Uncertainty Intervals

VARIABLE	SYMBOL	AVERAGE VALUE	UNCERTAINTY INTERVAL (w)
Representative of 0.051 g Condition			
Accelerating Force	$f_N$	16.5 lb <sub>f</sub>	$\pm 0.25$ lb <sub>f</sub>
Mass of Test Cell	m	324.0 lb <sub>m</sub>	$\pm 1.0$ lb <sub>m</sub>
Liquid Density	$\rho$	49.4 lb <sub>m</sub> /ft <sup>3</sup>	$\pm 0.5$ lb <sub>m</sub> /ft <sup>3</sup>
Surface Tension at Liquid-Gas Interface	$\sigma$	22.6 dyne/cm	$\pm 1.0$ dyne/cm
Pore Radius	r	0.141 in.	$\pm 0.003$ in.
Representative of 0.020 g Condition			
Accelerating Force	$f_N$	6.0 lb <sub>f</sub>	$\pm 0.25$ lb <sub>f</sub>
Mass of Test Cell	m	300.0 lb <sub>m</sub>	$\pm 1.0$ lb <sub>m</sub>
Pore Radius	r	0.391 in.	$\pm 0.003$ in.
Representative of 0.0014 g Condition*			
Accelerating Force	$f_N$	0.435 lb <sub>f</sub>	$\pm 0.015$ lb <sub>f</sub>
Mass of Test Cell	m	300.0 lb <sub>m</sub>	$\pm 1.0$ lb <sub>m</sub>
Pore Radius	r	1.703 in.	$\pm 0.003$ in.
*Values for liquid density and surface tension are the same at all g levels. The test liquid is methanol.			



The average values and uncertainty intervals given in Table 5 can be substituted for each of the variables to obtain the estimated accuracy of the Bo number at each of the three basic low-g test conditions. The uncertainties are listed below.

<u>Uncertainty</u>	<u>Acceleration</u>
±6.3%	0.051 g
±6.2%	0.020 g
±5.6%	0.0014 g

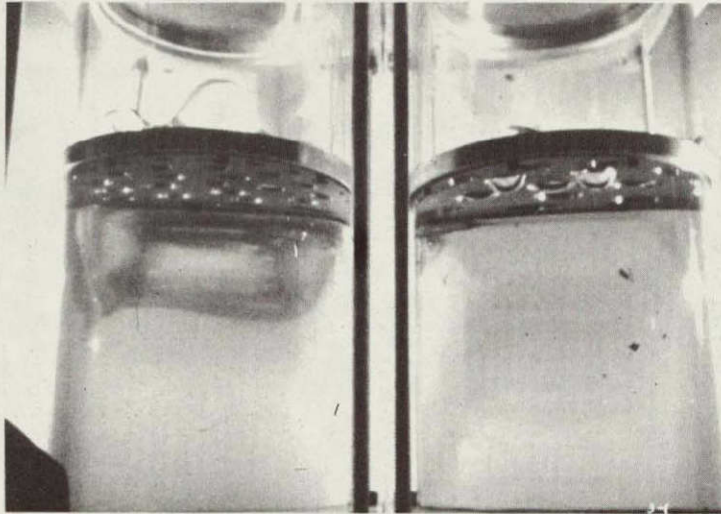
The numbers were calculated using the properties for methanol and the smallest pore sizes used with methanol for tests. The ranges are representative of the other test liquids and pore sizes, as well.

It is interesting to note that, at the lowest g-level, the probable inaccuracies in the surface tension and the acceleration force were the more significant, and contributed about equally to the uncertainty of the Bo number. At 0.02 g, this again was the case. On the other hand, at 0.051 g, the variations in the pore size and the surface tension were the critical variables in determining the reliability of the Bo number.

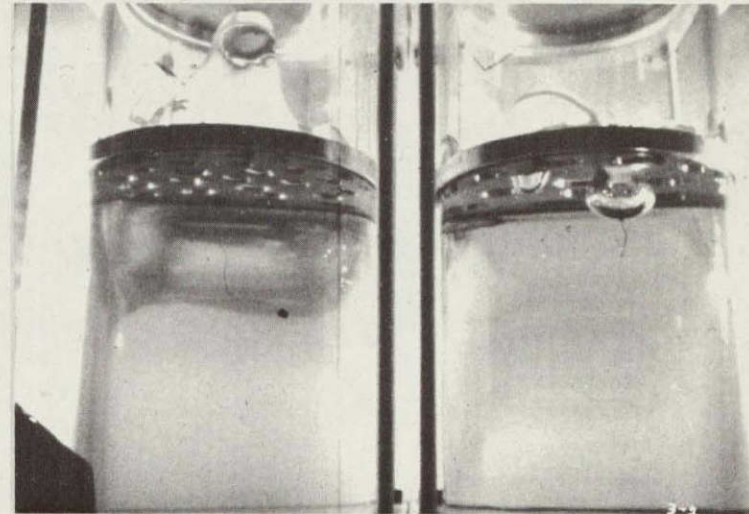
The stability or instability of a given foraminous barrier was determined from the 16-mm color film documenting the entire drop-test interval. The stability criteria were, by definition, either that no gas was ingested through the pores of the foraminous material into the liquid beneath the material or that the interface configuration was independent of time during the drop interval.

Typical of the gas-ingestion criterion is the photo sequence presented in Fig. 25. Several bubble sites are evident in the cylinder at the right at  $\Delta t = 0.976$  sec; however, as shown in the subsequent photos, only one bubble grew and detached. Other runs showing gas ingestion were similar, except that only two or three bubbles from a number of initial bubbles grew to critical size (bubble radius equal to the effective pore radius) and detached.

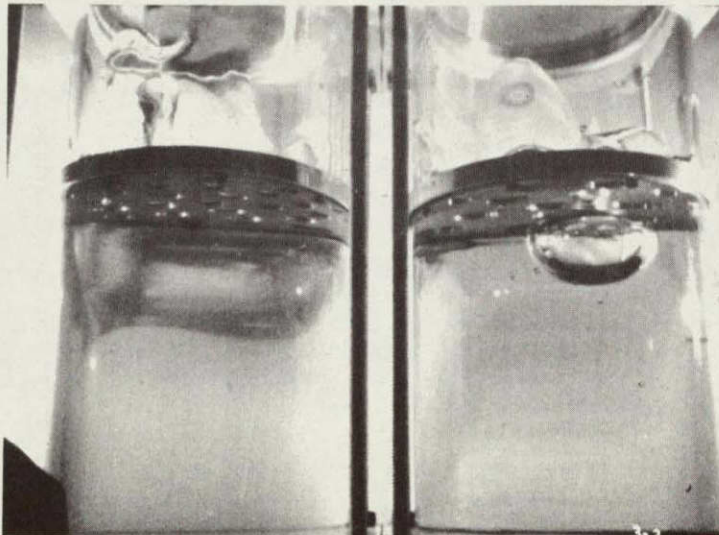




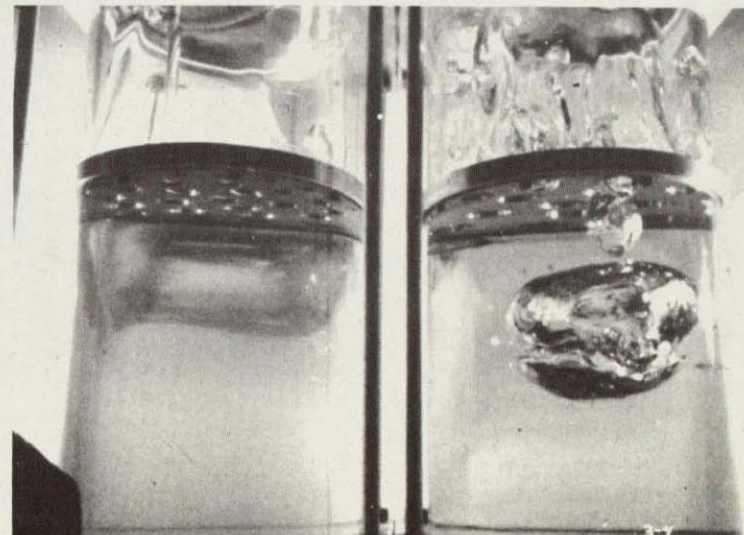
(a)  $\Delta t = 0.976$  sec



(b)  $\Delta t = 1.23$  sec



(c)  $\Delta t = 1.45$  sec



(d)  $\Delta t = 1.90$  sec

Fig. 25 Bubble Formation Due to Pore Instability, Run 31d



The liquid-gas interface changed during the drop because the interfacial elastic membrane tended toward its minimum gas-liquid area (minimum surface energy) and because the buoyant force acted on the curved interface at each pore of the barrier. Due possibly to slight variations in pore size, and/or uneven liquid cover over the barrier, one, or at most, several, gas bubbles tend to reach the critical bubble size at about the same time.

The bubble pressure is inversely proportional to the radius of curvature (Ref 19):

$$(\Delta P)_B = \sigma \left( \frac{1}{b_1} + \frac{1}{b_2} \right) \cos \theta; \quad [14]$$

and for a spherical interface ( $b = b_1 = b_2$ ), the pressure difference across the bubble surface,  $(\Delta P)_B$ , is simply

$$(\Delta P)_B = \frac{2\sigma}{b} \quad [15]$$

if we neglect contact-angle effects.

When the test capsule is dropped, there is little or no curvature of the pore interface (the radius of curvature approaches infinity) and the bubble pressure is near-zero. As the low-g condition continues, the interface becomes curved and its radius of curvature decreases until the differential bubble pressure reaches a maximum. This occurs when the radius of curvature equals the effective pore radius. Once this pressure condition is attained, the curvature moves towards a spherical shape and the bubble tends to detach.

Once a bubble leaves, as shown in Fig. 25, bubbles tend to continue to break through at that site and no new instability areas tend to form. As discussed in Ref 20, a supplementary force due to the detachment and motion of the bubbles that have already left the barrier surface acts on the new bubbles that are being formed.

This type of bubble breakthrough was observed, except at the lowest acceleration condition (0.00127 to 0.0014g). Because of the relatively large pore sizes (see Table 2) and the 5-in.-ID test specimens used in these tests, the perforated-plate barriers could contain only a single pore, and the type of instability was different. Rather than observe the gas breakthrough, we observed the interface configuration from the filmed

data to determine whether it was independent of time. If it was, we considered the pore to be stable. Conversely, the pore was judged unstable when the interface was time-dependent during the drop-test interval. Both the configuration of the interface and the motion of the liquid up the walls of the container were observed to establish the time-dependence. Of the two, the liquid motion along the walls could be determined more accurately from the filmed results. When this velocity slowed to zero, the interface configuration was assumed to be stable. Conversely, when the liquid layer continued to move upward along the walls, the interface configuration was assumed to be unstable.



#### IV. SCHEMES TO PREVENT PASSAGE OF SETTLED PROPELLANTS THROUGH FORAMINOUS BARRIERS

##### A. OBJECTIVES

The objective of the drop tower tests discussed in this section and in Ref 21 was to qualitatively evaluate the ability of various passive barriers to prevent liquid from passing through them under an axisymmetric settling condition. This is the condition pictured in Fig. 11(c). During these tests, the axial acceleration is applied normal to the barrier and tends to force liquid through the barrier to the opposite end of the cylindrical tank.

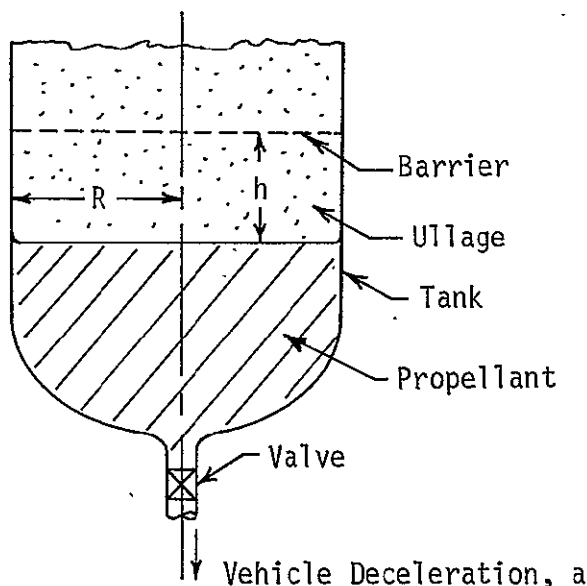


Fig. 26 Passive Barrier Control Problem

The damping and control problem studied is presented in Fig. 26, and is representative of the condition that exists following an engine shutdown. The liquid level is initially some distance,  $h$ , below the passive barrier, and it is assumed that, initially, the surface of the liquid is flat ( $Bo \gg 1000^*$ ). Following an engine shutdown, drag forces acting on the vehicle result in an axisymmetric deceleration,  $a$ , that tends to settle propellant away from the tank outlet. Although the drag force is relatively small and dependent on the orbital altitude, weight of the vehicle, and area, a deceleration of  $10^{-4}$  to  $10^{-7}$  g, or less (Ref 22), is probable.†

\*As noted in the previous chapter, the thrust of the Titan Transtage's main engine decays from 16,000 to 2,000  $lb_f$  in 0.4 sec and to zero in the next 0.6 sec. The Transtage has a mass of 28,000  $lb_m$  when loaded and a mass of 5,000  $lb_m$  at burnout. Its acceleration is, therefore, on the order of 0.57 to 3.2 g during an engine burn. The nitrogen tetroxide tank is 63.1 in. in diameter and the Aerozine-50 tank is 46.5 in. in diameter. The Bo numbers during an engine burn are calculated to be greater than  $1.9 \times 10^5$  for the oxidizer and  $5.8 \times 10^4$  for the fuel.

†Figure 12 of Ref 23 shows that the deceleration during coast for the AS-203 was  $1.8 \times 10^{-6}$  g. The settling Bo for the  $LH_2$  tank ( $R = 10.75$  ft) is calculated to be 5.74.

Figure 27 presents the settling Bo numbers for different cylindrical tank diameters in this deceleration range. The dashed curves are representative of a fuel ( $\beta = 12.0 \times 10^{-4} \text{ ft}^3/\text{sec}^2$ ); the solid lines represent an oxidizer ( $\beta = 6.7 \times 10^{-4} \text{ ft}^3/\text{sec}^2$ ). The kinematic surface tensions for liquid propellants are presented in Table 1. As seen from Fig. 27, the settling Bo range of practical interest is for  $Bo < 1000$ ; and for tanks less than 10 ft in diameter, it is for  $Bo < 120$ .

The axisymmetric propellant-settling studies conducted under Contract NAS8-11328 (Ref 24) categorized fluid motion into five different regimes as a function of a settling Bond number based on the radius of a cylindrical tank. This categorization is presented in Fig. 28. The settling data were compiled from drop tests conducted in Martin Marietta's free-fall facility. As shown in the figure, no flow was observed for Bo numbers less than one; and for  $1 < Bo < 20$ , the flow was along the walls of the cylinder. A central dome appears during settling at the high end of this Bond number range and tends to grow to a certain size and then remain stationary until the bulk liquid is depleted due to flow along the walls. At higher settling Bo numbers (to 500, or so), the central liquid dome continues to grow.

The propulsion engineer usually knows, or at least can estimate values for  $h$  and  $a$  (see Fig. 26) for a given application. In addition, he knows the tank radius ( $R$ ) and the liquid-propellant properties (surface tension, density, and liquid-to-solid contact angle). After calculating the initial and the settling Bond numbers to bracket the particular propellant-control problem, he needs additional criteria to select the best barrier design that will provide the damping and propellant control required.

This brief discussion shows the magnitude and scope of the propellant-control problem addressed by this program. As a result, this experimental investigation should only be regarded as a preliminary evaluation based on the following assumptions:

- 1) The only accelerating force tending to settle propellant is axisymmetric;
- 2) Its magnitude corresponds to probable levels caused by vehicle drag ( $10^{-7}$  to  $10^{-4} \text{ g}$ );
- 3) The propellant tanks are cylindrical;
- 4) The Bo number is the criterion for categorizing fluid motion during settling;

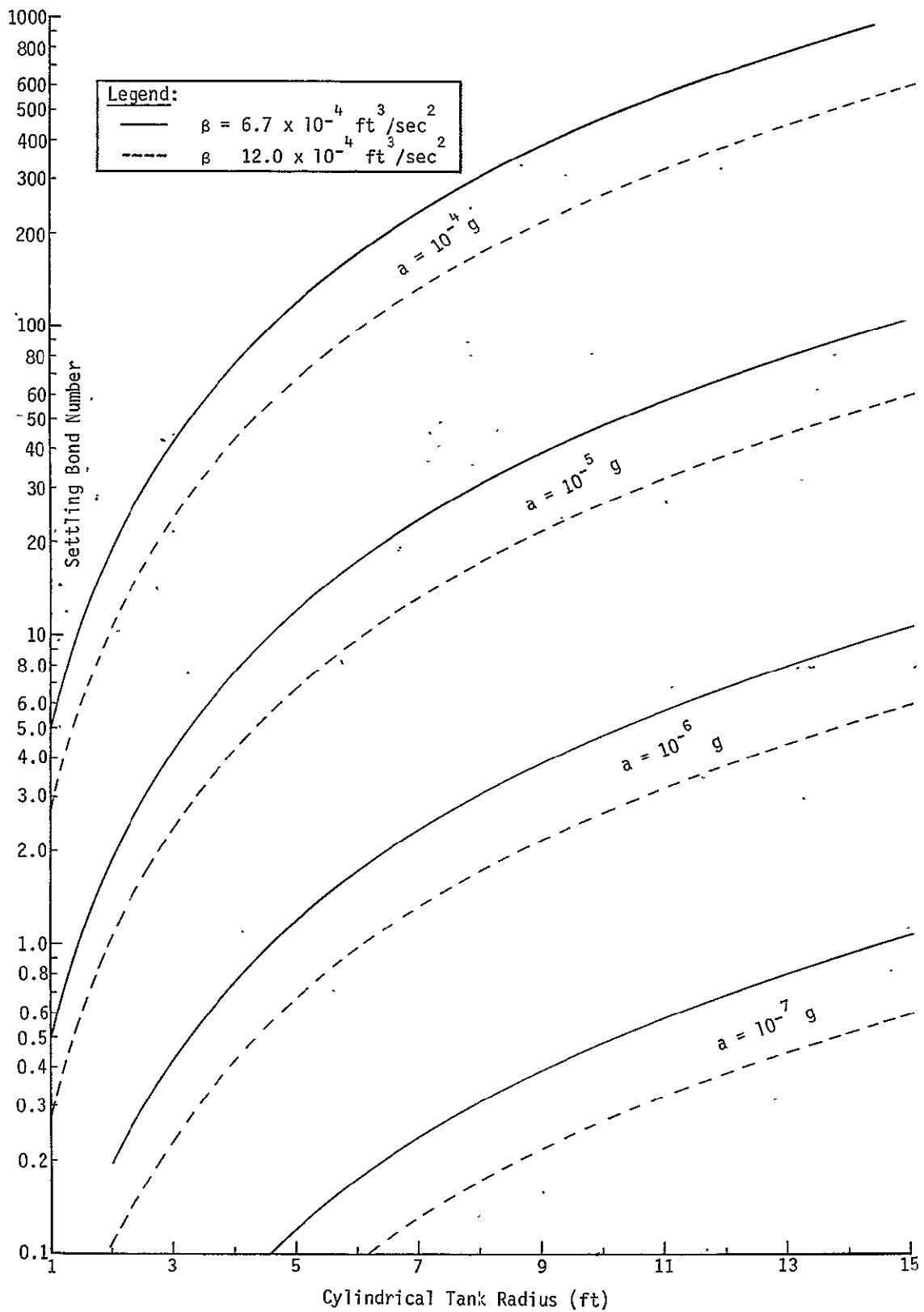


Fig. 27 Settling Bond Number vs Cylindrical Tank Radius



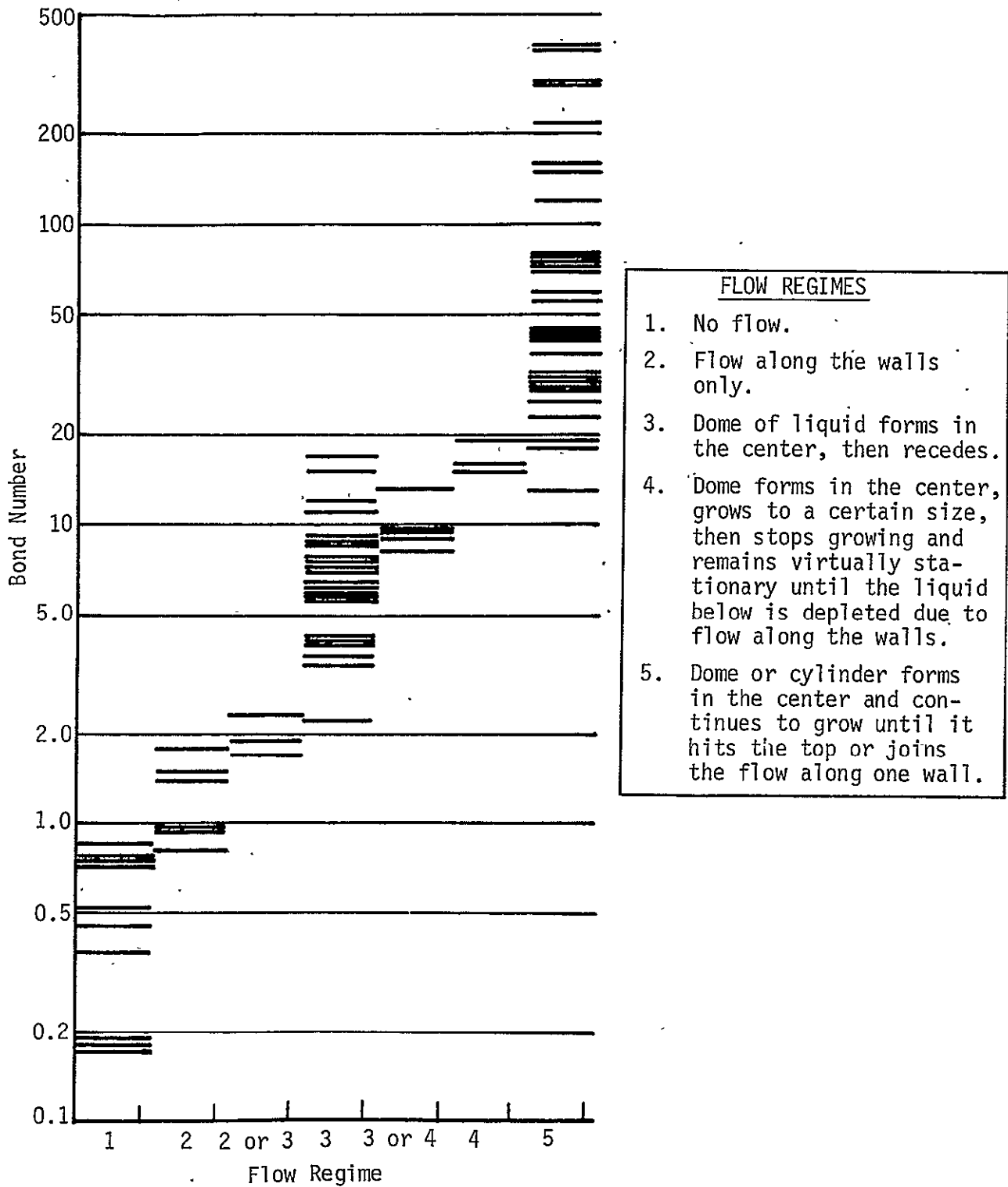


Fig. 28 Categorization of Flow Regimes During Settling  
(Data Compiled under Contract NAS8-11328)

- 5) The settling  $Bo$  range is less than 1000 for the propellant kinematic-surface-tension range shown in Table 1 and for the settling accelerations due to vehicle drag, and less than or equal to 120 when the tank radius is less than 5 ft;
- 6) The initial interface of the continuous liquid mass tending to be settled is flat ( $Bo \gg 1000$ );
- 7)- Control is to be achieved via flat passive barriers positioned normal to the settling acceleration.

## B. EXPERIMENTAL APPARATUS

The experimental apparatus was similar to that discussed in Chapter III. Cylindrical glass specimens 10 in. tall were positioned vertically, side-by-side, in view of the 16-mm camera, as shown in Fig. 15. Each contained a passive barrier positioned 6 in. from the bottom of the 4.97-in.-I.D. cylinder. The same three test liquids were used, i.e., methanol, carbon tetrachloride, and Freon-TF.

The following passive barrier schemes were evaluated:

- 1) Single-layer perforated plate;
- 2) Two perforated plates separated by an 0.087-in. gap;
- 3) Single-layer square-weave screen;
- 4) Two square-weave screens separated by an 0.087-in. gap;
- 5) Single-layer Dutch-twill screen;
- 6) Single-layer perforated plate with single and multitube inserts.

These passive barriers are described in Tables 6 and 7. The perforated plates were 0.032, 0.087, and 0.125-in. thick and had uniform pore diameters ranging from 0.125 to 0.376 in. The open-to-closed area ratio,  $\xi$ , ranged from 0.105 to 0.575. The double-plate specimens comprised two 0.087-in.-thick aluminum plates separated by an 0.087-in. gap, as shown in Fig. 31. The plates were skewed so as to provide no open area to flow normal to the flat configuration.

Table 6 Perforated Plate Barriers

BARRIER NO.	MATERIAL*	PLATE THICKNESS (in.)	PORE DIA. (in.)	PORE LAYOUT		$\epsilon^\dagger$	ADDITIONAL DESCRIPTION
				FIG.	$L$ (in.)		
1	Al	0.087	0.125	29	0.250	0.176	
1A	Al	0.032	0.125	29	0.250	0.176	
1B	Al	0.125	0.125	29	0.250	0.176	
2	Al	0.087	0.187	29	0.375	0.153	
2A	Al	0.032	0.187	29	0.375	0.153	
2B	Al	0.125	0.187	29	0.375	0.153	
3	Al	0.087	0.253	29	0.250	0.155	
4	Al	0.087	0.376	29	0.750	0.141	
5	Al	0.087	0.271	29	0.500	0.178	Tubes (L/D = 4.41) protrude 0.25 in. above plate.
6	Al	0.087	0.183	29	0.375	0.145	Tubes (L/D = 4.02) protrude 0.25 in. above plate.
7	Al	0.087	0.065	Centered - Single Pore		0.030	Tubes are 3 in. long and open-ended. Upper end is flush with top of plate.
8	Al	0.087	0.937	Centered - Single Pore		0.035	Screen tube (200x1400 mesh) is 2.75 in. long and closed at bottom. Upper end is flush with top of plate.
9	Al	0.087	0.256	29	0.625	0.105	
10	Al	0.087	0.256	30	0.313	0.575	
11	Al	0.087	0.191	29	0.469	0.106	
12	Al	0.087	0.191	30	0.250	0.430	
13	Al	0.087	0.253	30	0.625	0	Used with Barrier 9; barriers are separated by 0.087 in. (Fig. 31)
14	Al	0.087	0.187	30	0.469	0	Used with Barrier 11; barriers are separated by 0.087 in. (Fig. 31)
15	Al	0.087	0.271	29	0.500	0.178	Same as for Barrier 5, but with tubes flush with bottom of plate.
16	Al	0.087	0.183	29	0.375	0.145	Same as for Barrier 6, but with tubes flush with bottom of plate.

\*Al = aluminum.

$^\dagger$ Ratio of open-to-closed area (flow normal to barrier).

Table 7 Screen Barriers

BARRIER NO.	MATERIAL*	WEAVE	MESH SIZE	PORE OPENING (in.)	WIRE DIA. (in.)	$\epsilon^\dagger$
17	S.S.	Dutch Twill	325 x 2300	0.000473		0
18	S.S.	Dutch Twill	200 x 1400	0.000709		0
19	S.S.	Dutch Twill	165 x 800	0.001380		0
20	S.S.	Square	50 x 50	0.010000	0.010	0.250
21	S.S.	Square	30 x 30	0.020300	0.013	0.371
22	S.S.	Square	12 x 12	0.065300	0.018	0.608
23	S.S.	Square	12 x 12	0.065300	0.018	0.608
24	S.S.	Square	30 x 30	0.020300	0.013	0.371
28	S.S.	Square	100 x 100	0.005500	0.0045	0.302
29	S.S.	Square	200 x 200	0.002900	0.0021	0.336
30	S.S.	Dutch Twill	30 x 250	0.002760		0
31	S.S.	Dutch Twill	24 x 110	0.00551		0

\*S.S. = stainless steel.

$^\dagger$ Ratio of open-to-closed area (flow normal to barrier).

$^\ddagger$ Two layers of screen separated by an 0.087-in. spacer.



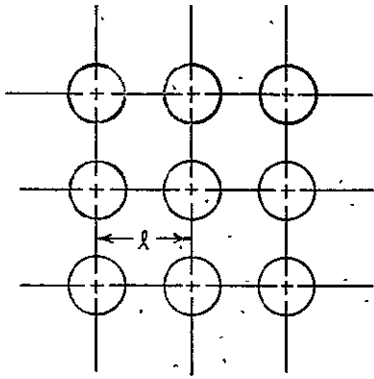


Fig. 29 Square Hole Pattern

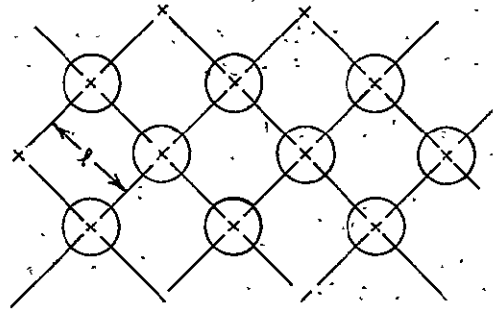


Fig. 30 Staggered Hole Pattern

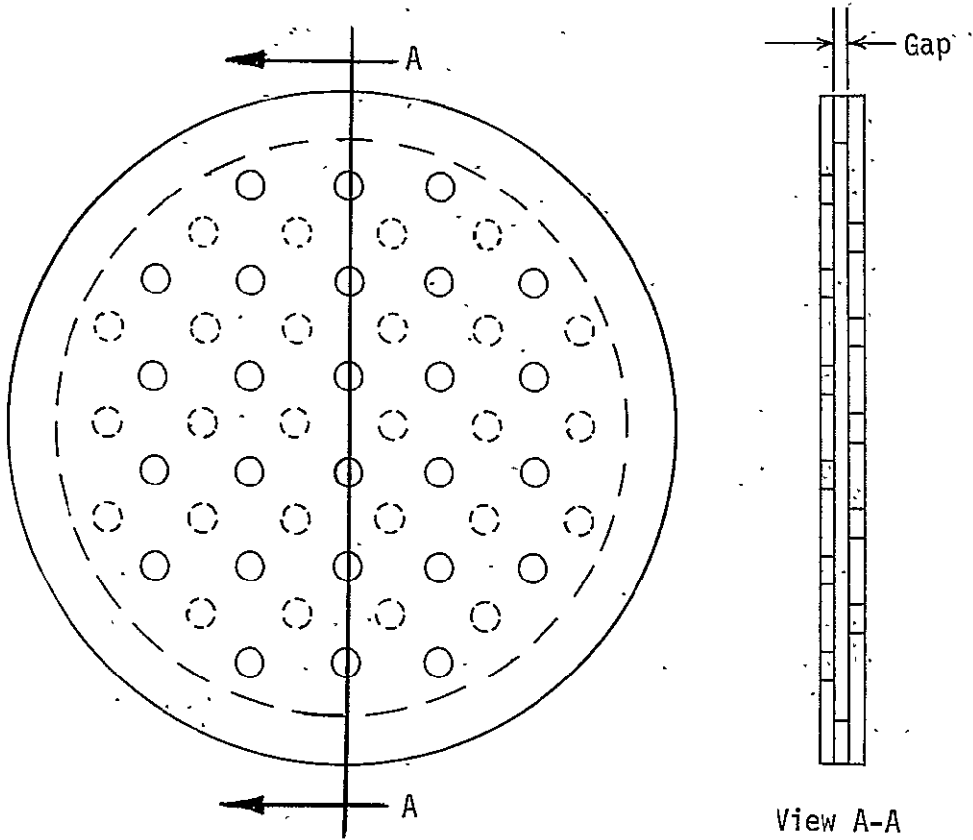


Fig. 31 Double-Plate Barrier with Offset Pores

The square-weave barriers had mesh sizes of 12, 30, 50, 100, and 200, with corresponding pore openings of 0.0653, 0.0203, 0.0100, 0.0055, and 0.0029 in., respectively. The pore sizes are those supplied by the screen supplier, Pyramid Screen Co, New York, New York. The double-screen specimens were composed of either two 12-mesh or two 30-mesh screens, separated by an 0.087-in. gap.

The flat twilled cloth tested had mesh sizes of 24 x 110, 30 x 250, 165 x 800, 200 x 1400, and 325 x 2300. The corresponding pore openings used for all calculations are 0.00551, 0.00276, 0.00138, 0.00709, and 0.000473 in., respectively. These sizes correspond to the lower values for the absolute micron rating ranges specified by the Western Filter Co, Gardena, California, and Kressilk Products, Inc, Monterey Park, California (see Table 8). The lower values were used since no forming or fabrication was required.

The twilled and square-weave barriers were made of stainless steel. The twilled cloth had no open area to flow normal to its flat surface. The open area-to-closed area ratios for the square-weave screen ranged from 0.250 to 0.608 (see Table 7).

The multitube barriers consisted of an 0.087-in. aluminum plate and either 0.271-in.-I.D. ( $L/D = 4.4$ ) or 0.183-in.-I.D. ( $L/D = 4.0$ ) open-ended tubing (see Fig. 32). The open area-to-closed area ratios were 0.178 and 0.143, respectively.

Table 8 Dutch-Twill Micron Ratings

<u>Mesh Size</u>	<u>Absolute Micron Rating</u>
24 x 110	140 to 175
30 x 250	70 to 100
165 x 800	35 to 40
200 x 1400	18 to 25
325 x 2300	15 to 18

The single-tube barriers are No. 7 and 8, as listed in Table 6. Barrier 7 had a single 0.865-in.-I.D., 3-in.-long glass tube (see Fig. 33). Barrier 8 was similar, except that a 0.937-in.-I.D., 2.75-in.-long screen tube was used in place of the glass tube. The screen device is pictured in Fig. 34. A flat, non-perforated aluminum plate was fitted flush with the open end of the glass or screen tube, as shown in Fig. 33.

Except for Barriers 7 and 8 and the pie-tin barrier pictured in Fig. 35, all barriers were flat (horizontal).

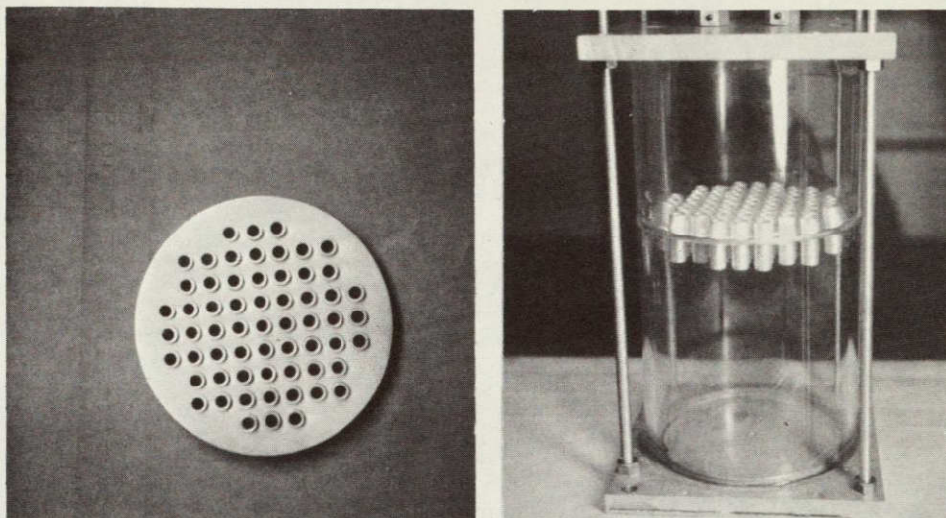


Fig. 32 Multitube Insert Barrier (Tubes did not protrude below the barrier for some tests, as shown on left).

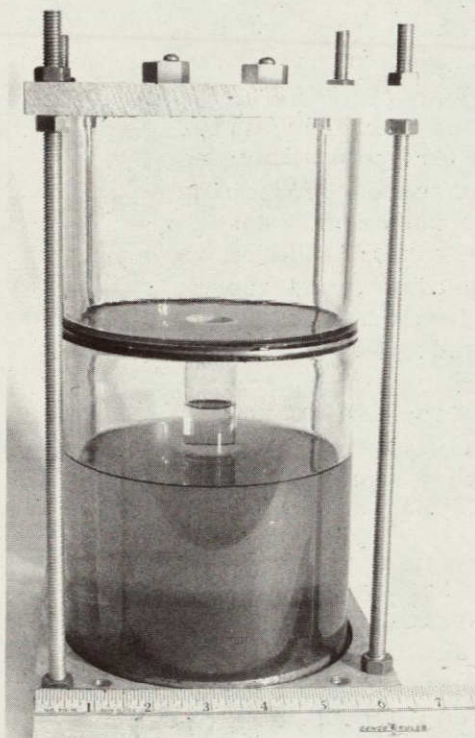


Fig. 33 Barrier 7

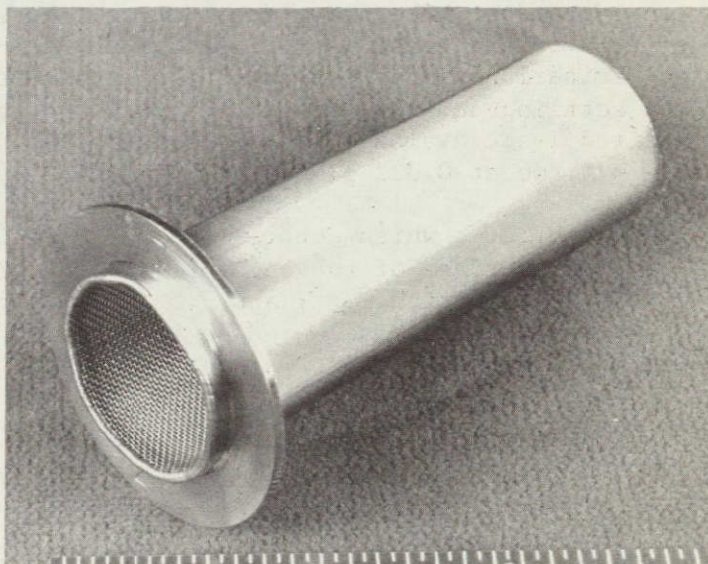


Fig. 34 Screen Tube Used in Barrier 8



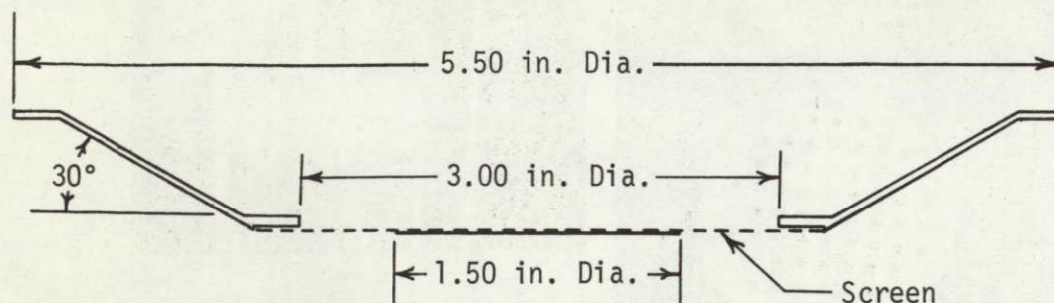


Fig. 35 Pie-Tin Barrier

### C. TEST PROCEDURE

As mentioned earlier, determining the ability of various barrier schemes to damp and control the liquid during settling was of prime consideration. The experimental approach was to observe the damping effects for at least 1 sec during the 2.1-sec test duration. Based on limitations with respect to the drop capsule, the magnitude of the settling acceleration, the size of the test specimen, and the desired 1-sec evaluation period, the following  $h/R$  values were used:  $h/R = 0.806$  at  $0.022$  g; and  $h/R = 1.205$  at  $0.031$  and  $0.040$  g.

The  $h$  term, which denotes the distance between the liquid and the lower surface of the barrier (see Fig. 26), was 2.0 in. for the lowest acceleration level and 3.0 in. for the other accelerations. The  $h/R$  ratios were selected so that the central liquid column made contact with the barrier in approximately 1 sec.

The drop tests were conducted over a settling  $Bo$  range from 30.4 to 135.0, based upon the radius of the cylindrical tank. The three axial accelerations were 0.022, 0.031, and 0.040 g (nominal), respectively. The settling condition we desired to obtain in order to permit the best correlation of test results is that described as Regime 5 in Fig. 28; this regime is characterized by liquid flowing along the wall of the cylindrical specimen and in a single central column, as shown in Fig. 36. In this figure,



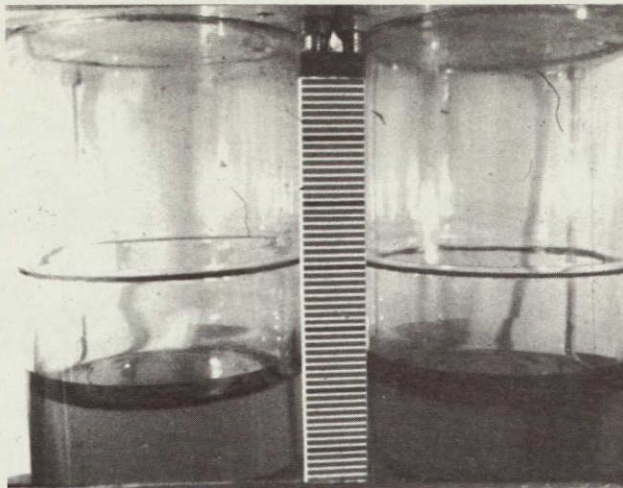
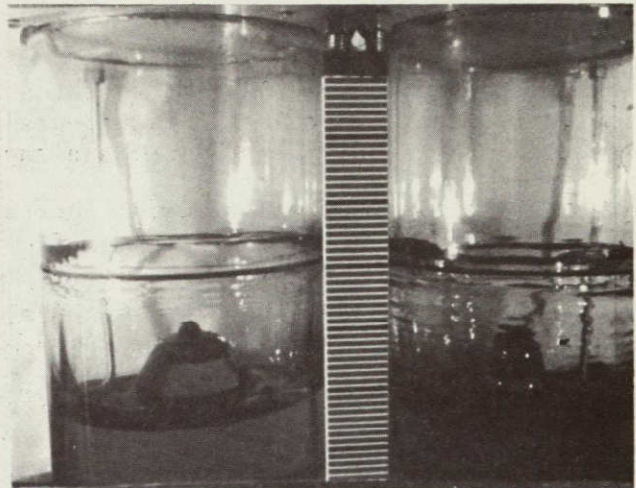
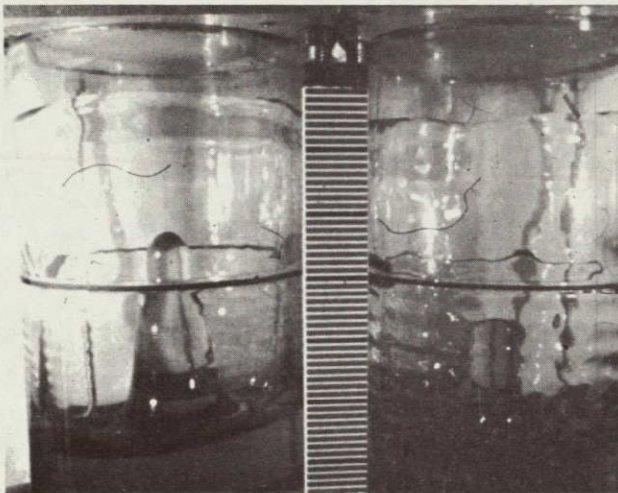
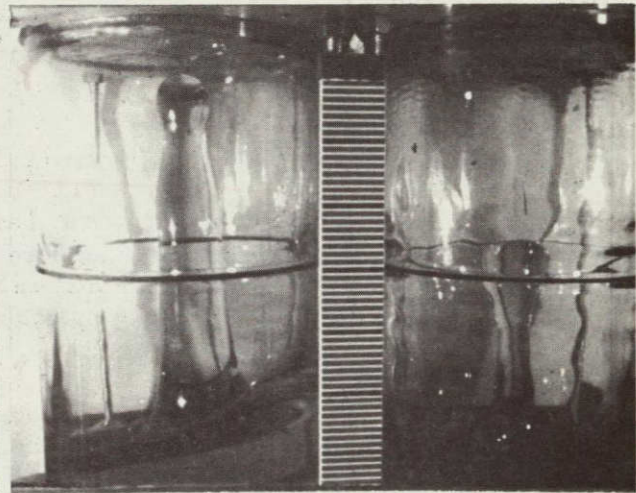
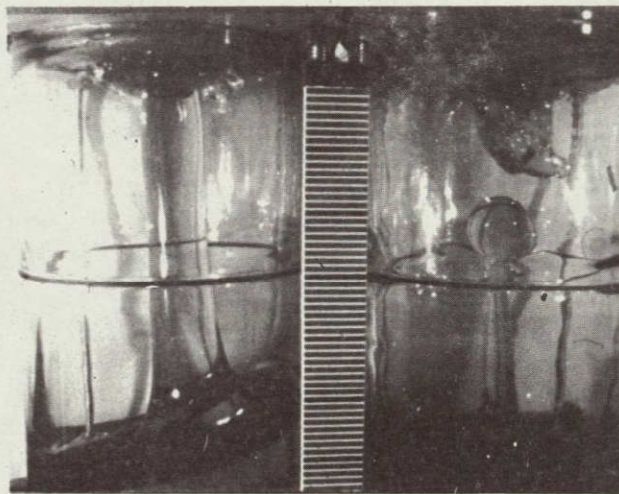
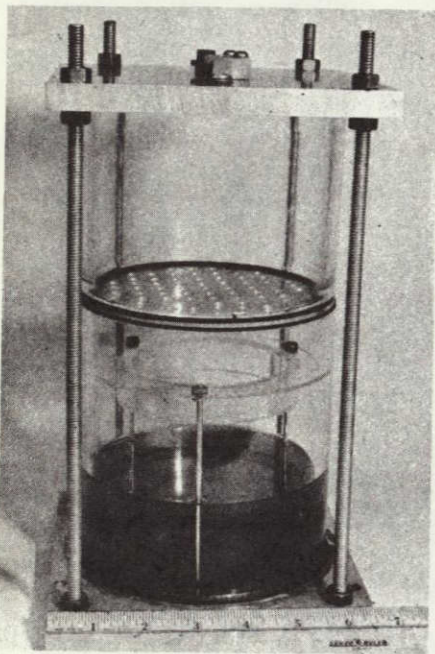
(a)  $\Delta t = 0.2$  sec(b)  $\Delta t = 1.0$  sec(c)  $\Delta t = 1.4$  sec(d)  $\Delta t = 1.8$  sec(e)  $\Delta t = 2.0$  sec

Fig. 36 Settling Results for Run 60  
(Freon TF in left cylinder;  
methanol in right;  $a = 0.022g$ )



the test specimen on the left contains Freon-TF and the other holds methanol; the initial liquid-gas interface is flat. The settling  $Bo$  is 30.4 for the methanol and 74.0 for the Freon-TF.

A film analyzer and recorder (Boscar Model N-1) was used to measure the wall-flow and columnar-flow displacements as a function of test time. A single 16-mm film frame was projected on a 20 x 20-in. screen containing a set of movable cross-wires. The displacements were translated into coded signals that were stored and displayed digitally on command. A movement of 0.002 in. corresponded to one machine count. A vertical scale was photographed with each test and used to calibrate the machine readings. The latter, in 1-in. increments from the initial level of the liquid to the barrier, were determined before measuring the displacement. The test interval was determined by counting the film frames and the timing pips (20 pips = 1 sec) on the margin of the film. Velocity data could then be obtained by graphically differentiating the flow histories.



Cylindrical specimens were filled from the bottom so that the barrier would not be wetted before beginning the drop test. Some tests were conducted with a transparent annular baffle (see Fig. 37) positioned below the barrier to prevent it from being wetted due to wall flow, instead of by the central column. The majority of tests, however, were made without the deflector baffle. When a barrier provided relatively good damping without the baffle, it was to be tested with the baffle so the results could be compared.

Fig. 37 Test Specimen with Perforated Plate and Annular Deflector Ring

#### D. EXPERIMENTAL RESULTS

The tests showed that, over the settling  $Bo$  range of 30.4 to 135.0, the liquid flowing up the wall always made contact with the barrier before the central liquid column; consequently, the barrier was always either partially, or completely, wetted before the central column impinged on it.



In a few tests, we noted that the liquid flowing up the wall would first wet the barrier and then converge and redirect itself back towards the central column (as the methanol did in Fig. 36). This redirected flow was undesirable since it tended to damp the central liquid column and make it extremely difficult to measure the velocity with which the column made contact with the barrier. The usual result was that the test was nullified. This redirected-wall-flow problem was observed for less than 10 runs, and only for tests in which methanol was used.

The flow of liquid along the cylinder wall and in the central column was observed for each test, and the velocity for each was determined. The columnar velocity was the more important since it was used to calculate the Weber ( $We$ ) number, a dimensionless ratio of liquid inertia-to-capillary forces. This impingement ( $We$ ) number was used to correlate the different liquid-damping and control regimes that were observed.

The columnar impingement velocity data are presented in Fig. 38 and include tests conducted with and without the annular baffle. The nine separate sets of data represent results for the three test liquids at the three nominal axial-settling accelerations. In general, the baffle tended to redirect the wall flow back toward the lower portion of the central settling column and accelerate the column. The scatter in the data is attributed to variations in the force from the NEG'ATOR motors, the initial level of the liquid, the alignment of the test specimen, free surface disturbances, and wall-flow interference. (The latter was discussed earlier.)

Variations in the initial level of the liquid were less than  $\pm 1/16$  in., since for each test the desired liquid volume was measured before filling the test specimens and the fill level was then checked. These variations were most critical at the 0.022-g condition, since the distance to the undersurface of the barrier was only 2 in. ( $h/R = 0.806$ ), and were less important at the two higher accelerations, since the travel distance was 3 in. ( $h/R = 1.205$ ).

The variations in the accelerating force provided by the NEG'ATOR motors were discussed in Chapter II. These variations, though small, did contribute some to the velocity scatter.

The primary reasons for the difference in impingement velocity at a given settling  $Bo$  were misalignment and free-surface disturbances prior to, and during, capsule release.



Slight lateral accelerations, in addition to the axial acceleration, were observed in approximately half of the tests. Differences in columnar velocities were determined for identical test specimens (except for the foraminous barriers) during the same drop test.

The maximum impingement velocity,  $v_c$ , for columnar flow can be described as

$$v_c = K_c (2ah)^{1/2}, \quad [16]$$

where the constant  $K_c$  can be determined from Fig. 39. The maximum velocities were obtained from Fig. 38.  $K_c$  varied from 0.495 to 0.601 for methanol and carbon tetrachloride at the two different liquid-level conditions ( $h/R = 0.806$  and  $h/R = 1.205$ ). The values for Freon-TF ranged from  $0.622 \leq K_c \leq 0.905$ , and were considerably higher than those for the other fluids.

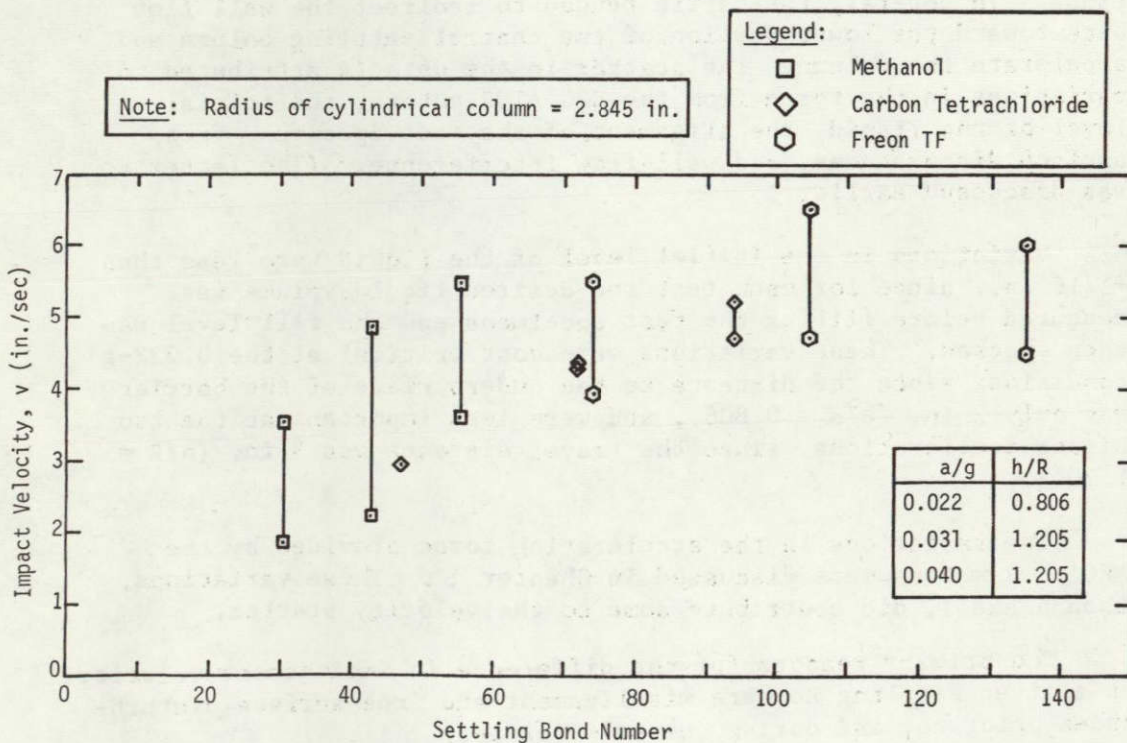


Fig. 38 Impact Velocity of Liquid Column vs Settling Bond Number

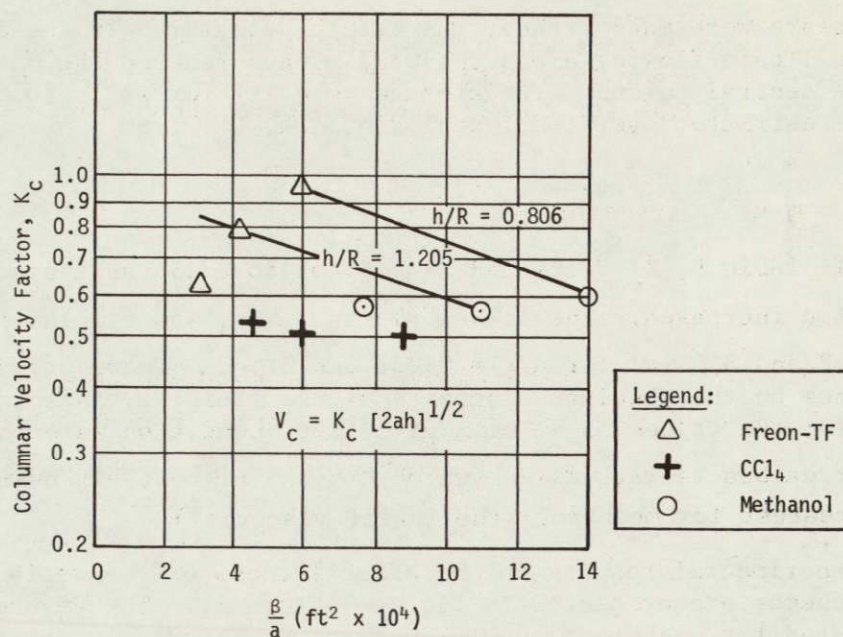


Fig. 39 Columnar Velocity Factor

The formation, shape, and flow characteristics observed for the central liquid column were different for the Freon-TF, as is somewhat evident in Fig. 36. The test liquids, methanol and Freon-TF, first begin to flow up the walls of the containers, and as the low-g acceleration continues, a central liquid dome forms in the Freon-TF and moves upward. Subsequent surface-wave phenomena then cause the cross-sectional area of the central dome to neck down forming a smaller-diameter dome to be accelerated upward. This effect tended to produce columnar impingement velocities for Freon-TF that were generally greater than those for methanol and carbon tetrachloride, particularly at the two lower acceleration test conditions. As shown in Fig. 36, after about 2 sec into the drop the Freon-TF has already made contact with the closed end of the 10-in.-tall container, while the central column of methanol has climbed only about mid-way toward the top of the cylinder.



Most tests were made without the baffle detector. In these cases, the liquid flowing along the wall always reached the barrier before the central column. The average velocity for wall flow,  $v_w$ , can be estimated over its travel distance,  $L_v$ , from

$$v_w = K_w (2aL_v)^{1/2}.$$

As noted in Table 9,  $K_w$  decreased from 0.402 to 0.256 as the axial acceleration increased. The travel distance,  $L_v$ , was 2.0 in. for  $a/g = 0.022$  and 3.0 in. for  $a/g = 0.031$  and 0.040. There was also a dependence on the absolute viscosity of the fluid,  $\mu$ , as shown in Table 10; the values of  $K_w$  at a given test condition were the lowest for carbon tetrachloride (which had the highest viscosity), and the greatest for methanol (the lowest viscosity).

The experimental results on the effectiveness of the various barrier schemes are presented in Tables 11 thru 16. The We numbers are presented for each test run, along with the barrier's damping performance. The impingement We number was calculated from

$$We = \frac{(v_c)^2 r}{\beta}, \quad [18]$$

where  $v_c$  is the impingement velocity of the central column. The pore radii ( $r$ ) for the perforated-plate and square-weave barriers were assumed to be one-half the open-pore dimensions. For Dutch-twill screens, an effective radius of one-half the pore openings listed in Table 7 was used.

The performance exhibited by the barriers was categorized against the following damping regimes, which are pictured in Fig. 40. The regimes were arbitrarily selected and are described below.

<u>Regime</u>	<u>Description</u>
A	No liquid passes through the barrier
B	A relatively small amount of liquid passes through the barrier during wetting of the barrier by liquid settling along the wall of the cylindrical container;

Table 9 Liquid-Wall-Flow Velocity Factors,  $K_w$ 

TEST LIQUID	ACCELERATION CONDITION		
	a/g = 0.022	a/g = 0.031	a/g = 0.040
Methanol	0.402	0.380	0.324
$\text{CCl}_4$	0.318	0.318	0.256
Freon-TF	0.372	0.351	0.304

Table 10 Physical Properties of Test Liquids\*

TEST LIQUID	TEMPERATURE (°C)	DENSITY, $\rho$ ( $\text{lb}_m/\text{ft}^3$ )	SURFACE TENSION, $\sigma$ ( $\times 10^3 \text{ lb}$ )	KINEMATIC SURFACE TENSION, $\beta$ ( $\times 10^4 \text{ ft}^3/\text{sec}^2$ )	ABSOLUTE VISCOSITY, $\mu$ ( $\times 10^4 \text{ lb}_m/\text{ft-sec}$ )	CONTACT ANGLE, $\theta$ (deg)
Methanol	20	49.4	1.55	10.1	4.02	0
Carbon Tetra- Chloride	20	99.6	1.84	5.95	6.51	0
Freon-TF	20	98.6	1.27	4.15	4.70	0

\*J. A. Salzman, T. L. Labus, and W. J. Masica: *An Experimental Investigation of the Frequency and Viscous Damping of Liquids during Weightlessness*. TN-D-4132. NASA, August 1967.

- C The dome of the central liquid column penetrates the barrier, resulting in a sessile globule, or recedes completely;
- D The central liquid penetrates the barrier as one or two columns that pinch off and remain above the barrier, but no additional liquid passes;
- E Similar to Regime D, but the columns are not completely pinched off;
- F A considerable amount of liquid penetrates the barrier as a number of columns (streamers)
- G A massive amount of liquid passes through the barrier with no apparent damping.



Table 11 Summary of Single-Layer Perforated Plate Tests

RUN NO.	a/g	(Bo) <sub>s</sub>	DEFL-ECTOR	CYLINDER 1								CYLINDER 2							
				TEST LIQUID*	h (in.)	R (in.)	v <sub>c</sub> (in./sec)	$\beta/v_c^2$ (in.)	We	BAR-RIER	DAMP-ING CATE-GORY	TEST LIQUID*	h (in.)	R (in.)	v <sub>c</sub> (in./sec)	$\beta/v_c^2$ (in.)	We	BAR-RIER	DAMP-ING CATE-GORY
22	0.031	43.0	No	M	3.0	2.485	4.84	0.0745	1.255	2	B,C	M	3.0	2.485	4.84	0.0745	1.691	3	B,C
23	0.031	43.0	Yes	M	3.0	2.485	3.34	0.157	0.598	2	F	M	3.0	2.485	4.03	0.107	0.806	3	F
24	0.031	43.0	Yes	M	3.0	2.485	3.60	0.135	0.463	1	E	M	3.0	2.485	3.60	0.135	1.392	4	F
29	0.022	30.4	No	M	2.0	2.485	1.93	0.469	0.200	2	B,C	M	2.0	2.485	2.15	0.378	0.334	3	C
30	0.022	30.4	No	M	2.0	2.485	2.03	0.424	0.148	1	B	M	2.0	2.485	2.93	0.424	0.434	4	B,C
31	0.040	55.5	No	M	3.0	2.485	3.61	0.134	0.467	1	B,E	M	3.0	2.485	4.49	0.0866	2.172	4	B,F
32	0.040	55.5	No	M	3.0	2.485	5.02	0.069	0.903	1	B,C	M	3.0	2.485	5.02	0.069	2.715	4	B,F
33	0.040	55.5	No	M	3.0	2.485	4.48	0.087	1.469	9	B,C	M	3.0	2.485	4.48	0.087	1.469	10	B,G
34	0.031	43.0	No	M	3.0	2.485	4.13	0.102	1.251	9	B,C	M	3.0	2.485	4.13	0.102	1.251	10	B,G
35	0.022	30.4	No	M	2.0	2.485	2.22	0.354	0.361	9	B	M	2.0	2.485	2.22	0.354	0.361	10	B,G
37	0.031	43.0	No	M	3.0	2.485	4.82	0.075	1.271	11	B	M	3.0	2.485	4.82	0.075	1.271	12	B,F
72	0.022	47.0	No	CT	2.0	2.485	2.95	0.118	0.528	1	B,C	CT	2.0	2.485	2.95	0.118	0.790	2	B,C
73	0.031	72.0	No	CT	3.0	2.485	4.27	0.057	1.106	1	B,D	CT	3.0	2.485	4.33	0.055	1.738	11	B,D
74	0.040	94.0	No	CT	3.0	2.485	4.68	0.047	1.329	1	B,E	CT	3.0	2.485	4.68	0.047	2.031	11	B,D
74A	0.040	94.0	No	CT	3.0	2.485	5.21	0.038	1.647	1	B,F	CT	3.0	2.485	5.21	0.038	2.464	2	B,F
75	0.022	30.4	No	M	2.0	2.485	3.11	0.180	0.346	1A	B	M	2.0	2.485	3.52	0.141	0.444	1B	B
76	0.031	43.0	No	M	3.0	2.485	4.18	0.100	0.626	1	B,C	M	3.0	2.485	4.18	0.100	0.626	1B	B
77	0.040	55.5	No	M	3.0	2.485	5.13	0.066	0.943	1A	B,C	M	3.0	2.485	5.13	0.066	0.943	1B	B,D
78	0.031	43.0	No	M	3.0	2.485	4.25	0.097	0.647	1A	B,C	M	0.25	2.485				1	B,C
79	0.022	30.4	No	M	2.0	2.485	2.78	0.226	0.414	2	B,C	M	2.0	2.485	2.48	0.284	0.330	2B	B,C
80	0.031	43.0	No	M	3.0	2.485	4.45	0.088	1.061	2A	B,D	M	3.0	2.485	4.45	0.088	1.061	2B	B,D
81	0.040	55.5	No	M	3.0	2.485	5.24	0.064	1.471	2A	B,D	M	3.0	2.485	5.24	0.064	1.471	2B	B,D
82	0.022	30.4	No	M	2.0	2.485	5.78	0.052	1.790	2A	B,C	M	0.25	2.485				2	B
83	0.040	55.5	No	M	3.0	2.485	4.49	0.087	1.479	9	B,D	M	3.0	2.485	4.49	0.087	1.102	11	B,D
84	0.022	47.0	No	CT	2.0	2.485	3.24	0.098	1.305	9	B,C	CT	2.0	2.485	3.24	0.098	0.974	11	B,C

\*Liquid designations: M = methanol;

CT = carbon tetrachloride



Table 12 Summary of Double-Layer Perforated Plate Tests

RUN NO.	a/g	DEFL-ECTOR	CYLINDER 1								CYLINDER 2							
			TEST LIQUID*	Bo	h (in.)	R (in.)	V <sub>c</sub> (in./sec)	$\delta/v_c^2$ in	We	DAMPING CATEGORY	TEST LIQUID*	Bo	h (in.)	R (in.)	V <sub>c</sub> (in./sec)	$\delta/v_c^2$ (in.)	We	DAMPING CATEGORY
38	0.040	No	M	55.5	3.0	2.485	5.47	0.058	2.160	A	M	55.5	3.0	2.485	5.47	0.058	1.603	A
39	0.022	No	M	30.4	2.0	2.485	1.88	0.494	0.255	A	M	30.4	2.0	2.485	1.88	0.494	0.189	A
40	0.031	No	M	43.0	3.0	2.485	4.77	0.077	1.643	A	M	43.0	3.0	2.485	4.77	0.077	1.219	A
41	0.040	No	M	135.0	3.0	2.485	4.89	0.030	4.202	C	F	135.0	3.0	2.485	4.62	0.034	2.783	D
43	0.031	No	F	104.5	3.0	2.485	5.34	0.025	5.011	D	F	104.5	3.0	2.485	5.34	0.025	3.719	D
56	0.022	No	F	74.0	2.0	2.485	1.68	0.254	0.496	A	F	74.0	2.0	2.485	1.68	0.254	0.368	A
57	0.031	No	F	104.5	3.0	2.485	4.72	0.032	3.915	C	F	104.5	3.0	2.485	4.72	0.032	2.905	A
99	0.031	Yes	M	43.0	3.0	2.485	3.32	0.158	0.796	A	F	104.5	3.0	2.485	6.20	0.019	5.013	A
100	0.040	Yes	M	55.5	3.0	2.485	3.64	0.132	0.957	A	F	135.0	3.0	2.485	3.55	0.057	1.643	A

\*Liquid designations: M = methanol;  
F = Freon-TF

Category A is most desired; Regimes B and C also show good damping and liquid control. Categories F and G display negligible damping. Categories D and E separate the damped and undamped regimes and were the most difficult to determine; there was little or no problem in determining the damping associated with the other categories.

#### E. DISCUSSION OF RESULTS

Figures 41 thru 44 show the damping performance of single- and double-layer perforated plate barriers and of single-layer square-weave and Dutch-twill screen barriers. The results verify that the impingement We is an important dimensionless parameter for correlating liquid damping. The results shown in Fig. 41 and 43 are for tests made without the baffle deflector. In these tests, some liquid (Category B) always passed through the barrier when it was initially wetted.

The results shown in Fig. 42 and 44 are for tests made both with and without the baffle deflector, since the initial condition (wetted or non-wetted) of the barrier had no noticeable effect on its damping performance. This was true only for these two barrier configurations and not for the other barriers.



Table 13 Summary of Single-Layer Square Weave Barrier Tests

RUN NO.	a/g	DEFLECTOR	CYLINDER 1										CYLINDER 2									
			TEST LIQUID*	Bo	h (in.)	R (in.)	$v_c$ (in./sec)	$\beta/v_c^2$ (in.)	We	BARRIER	DAMPING CATEGORY	TEST LIQUID*	Bo	h (in.)	R (in.)	$v_c$ (in./sec)	$\beta/v_c^2$ (in.)	We	BARRIER	DAMPING CATEGORY		
49	0.022	Nc										M	30.4	2.0	2.485	2.24	0.348	0.014	20	B		
50	0.040	Nc										F	135.0	3.0	2.485	4.50	0.035	0.141	20	B,E		
52	0.040	Nc	F	135.0	3.0	2.485	4.58	0.034	0.296	21	B,F	F	135.0	3.0	2.485	5.23	0.026	1.244	23	B,G		
58	0.040	Nc	F	135.0	3.0	2.485	4.91	0.030	0.341	21	B,G											
59	0.040	Nc	F	135.0	3.0	2.485	5.70	0.022	1.477	23	B,G											
61	0.022	Nc	F	74.0	2.0	2.485	3.96	0.046	0.022	21	B,C	F	74.0	2.0	2.485	3.96	0.046	0.715	23	B,G		
62	0.031	Nc	M	43.0	3.0	2.485	3.63	0.132	0.008	21	B	M	43.0	3.0	2.485	3.63	0.132	0.247	23	B,F		
63	0.022	Nc	M	30.4	2.0	2.485	2.30	0.330	0.003	21	B	M	30.4	2.0	2.485	2.30	0.330	0.099	23	B,D		
64	0.040	Nc										M	55.5	3.0	2.485	3.75	0.124	0.042	20	B,D		
67	0.022	Nc										F	74.0	2.0	2.485	4.50	0.035	0.141	20	B,D		
94	0.031	Nc	M	43.0	3.0	2.485	3.39	0.152	0.018	28	B,C											
95	0.040	Nc	M	55.5	3.0	2.485	4.10	0.104	0.027	28	B,D											
96	0.040	Nc	M	55.5	3.0	2.485	3.77	0.123	0.012	29	B											
97	0.022	Nc	F	74.0	2.0	2.485	5.50	0.024	0.061	29	B,D											

\*Liquid designations: F = Freon-TF;  
M = methanol.

Table 14 Summary of Double-Layer Square Weave Screen Tests

RUN NO.	a/g	TEST LIQUID*	Bo	CYLINDER 1					CYLINDER 2				
				$v_c$ (in./sec)	$\beta/v_c^2$ (in.)	We	BARRIER	DAMPING CATEGORY	$v_c$ (in./sec)	$\beta/v_c^2$ (in.)	We	BARRIER	DAMPING CATEGORY
68	0.040	F	135.0	5.49	0.024	0.420	24	B,D	5.49	0.024	1.366	22	B,G
70	0.031	M	43.0	2.21	0.357	0.028	24	B,C	2.21	0.357	0.091	22	B,D
71	0.031	F	104.5	6.48	0.017	0.586	24	B,D	6.06	0.020	1.665	22	B,G

\*Liquid designations: F = Freon-TF;  
M = Methanol.

Table 15 Summary of Multitube Barrier Tests

RUN NO.	a/g	TEST LIQUID*	Bo	CYLINDER 1					CYLINDER 2				
				$v_c$ (in./sec)	$\beta/v_c^2$ (in.)	We	BARRIER	DAMPING CATEGORY	$v_c$ (in./sec)	$\beta/v_c^2$ (in.)	We	BARRIER	DAMPING CATEGORY
27†	0.031	M	43.0	2.88	0.210	0.644	5	G	2.31	0.327	0.280	6	G
28	0.031	M	43.0	2.63	0.252	0.537	5	F	2.63	0.252	0.363	6	D
44	0.040	M	55.5	4.48	0.087	1.558	15	B,F	4.48	0.087	1.052	16	B,D
46	0.040	F	135.0	5.00	0.029	4.725	15	B,F	5.00	0.029	3.190	16	B,F

\*Liquid Designations: M = Methanol;  
F = Freon-TF.

†Deflector used.



Table 16 Summary of Single-Layer Dutch Twill Barrier Tests

RUN NO.	a/g	TEST LIQUID*	Bo	h (in.)	R (in.)	DEFL-ECTOR	CYLINDER 1					CYLINDER 2				
							$v_c$ (in./sec)	$\delta/v_c^2$ (in.)	We	BARRIER	DAMPING CATEGORY	$v_c$ (in./sec)	$\delta/v_c^2$ (in.)	We	BARRIER	DAMPING CATEGORY
48	0.040	F	135.0	3.0	2.485	No	5.59	0.023	0.0103	17	A	5.31	0.026	0.0155	18	A
49	0.022	M	30.4	2.0	2.485	No	2.24	0.348	0.0020	19	A					
50	0.040	F	135.0	3.0	2.485	No	4.78	0.031	0.0220	19	A					
53	0.031	M	43.0	3.0	2.485	No	4.11	0.103	0.0023	17	A	4.11	0.0103	0.0034	18	A
54	0.022	M	30.4	2.0	2.485	No	3.48	0.144	0.0017	17	A	3.48	0.144	0.0025	18	A
64	0.040	M	55.5	3.0	2.485	No	3.75	0.124	0.0056	19	A					
65	0.040	M	55.5	3.0	2.485	No	4.48	0.087	0.0027	17	A	4.48	0.087	0.0041	18	A
67	0.022	F	74.0	2.0	2.485	No	4.50	0.035	0.0195	19	A					
94	0.031	M	43.0	3.0	2.485	No						3.39	0.152	0.0182	31	C
95	0.040	M	55.5	3.0	2.485	No						4.10	0.104	0.0266	31	C
96	0.040	M	55.5	3.0	2.485	No						3.77	0.123	0.0112	30	A
101	0.022	M	30.4	2.0	2.485	Yes	3.02	0.191	0.0019	18	A	3.02	0.191	0.0036	19	A
102	0.031	M	43.0	3.0	2.485	Yes	4.62	0.082	0.0043	18	A	3.32	0.158	0.0044	19	A
103	0.040	M	55.5	3.0	2.485	Yes	4.78	0.076	0.0047	18	A	4.78	0.0076	0.0090	19	A

\*Liquid designations: F = Freon-TF;  
M = methanol.

A drastic performance difference was observed for single-layer plate barriers tested with and without the baffle deflector. For example, the same barrier used in Run 76 (see Table 11), which showed Category B damping at  $We = 0.626$  without the deflector, displayed Category E damping with the deflector in Run 24 at  $We = 0.463$ . Similar results were observed for Barrier 3: Category C damping was observed at  $We = 1.691$  (Run 22), but Category F damping was observed at a lower  $We$  number (0.806) in Run 23 (see Table 11). The test results for Run 23 are pictured in Fig. 45; Barrier 2 is on the left; Barrier 3, on the right. The need to have the wall flow wet the perforated-plate barrier before the central column impinges on the barrier is evident in the photo sequence (Category F damping for both barriers).

The open-to-closed area ratio ( $\xi$ ) is another important criterion for predicting liquid damping. The results shown in Fig. 41 are for  $\xi \leq 0.176$ . Poor damping (Categories F and G only) was observed for barriers having greater  $\xi$  values -- e.g., for  $\xi = 0.430$  (Barrier 12) and  $\xi = 0.575$  (Barrier 10) (Table 6). The damping performance of Barriers 9 and 10, and 11 and 12, which had identical pore sizes but different  $\xi$  values, is presented in Table 11. Note the poor performance for Barriers 10 and 12 for Runs 33, 34, 35 and 37. Barriers 9 and 11 ( $\xi = 0.106$ ) for the same test runs show damping Categories B and C. The barriers





Category A



Category B



Category C



Category D



Category E



Category F or G

Fig. 40 Damping Categories A thru G

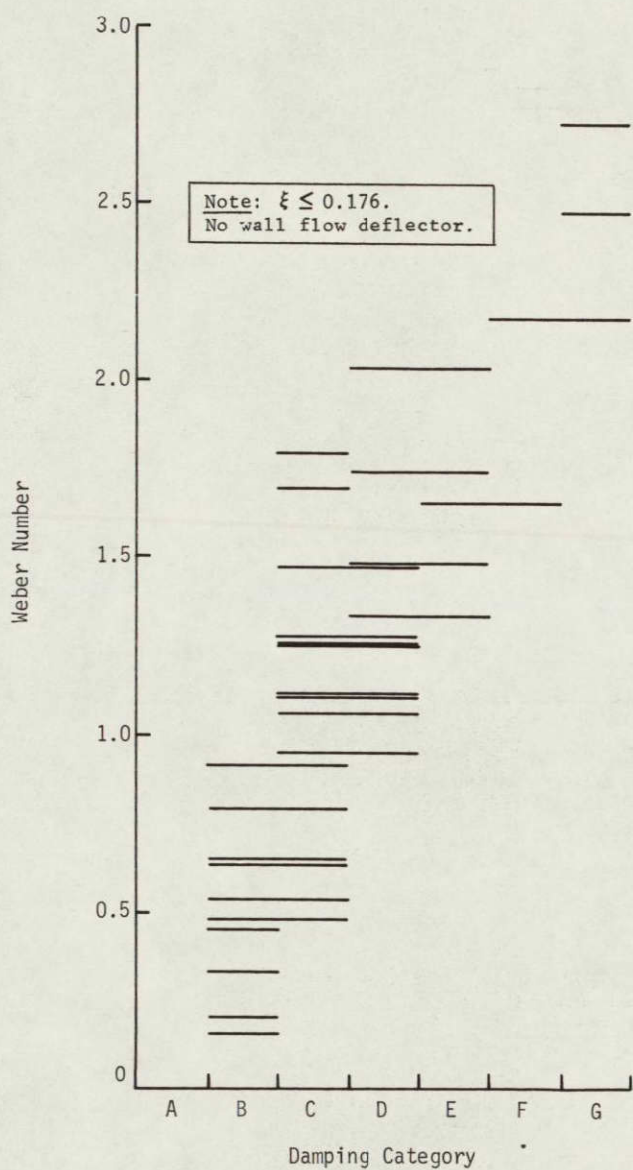


Fig. 41 Damping Performance of  
Single-Layer Perforated Plate Barriers

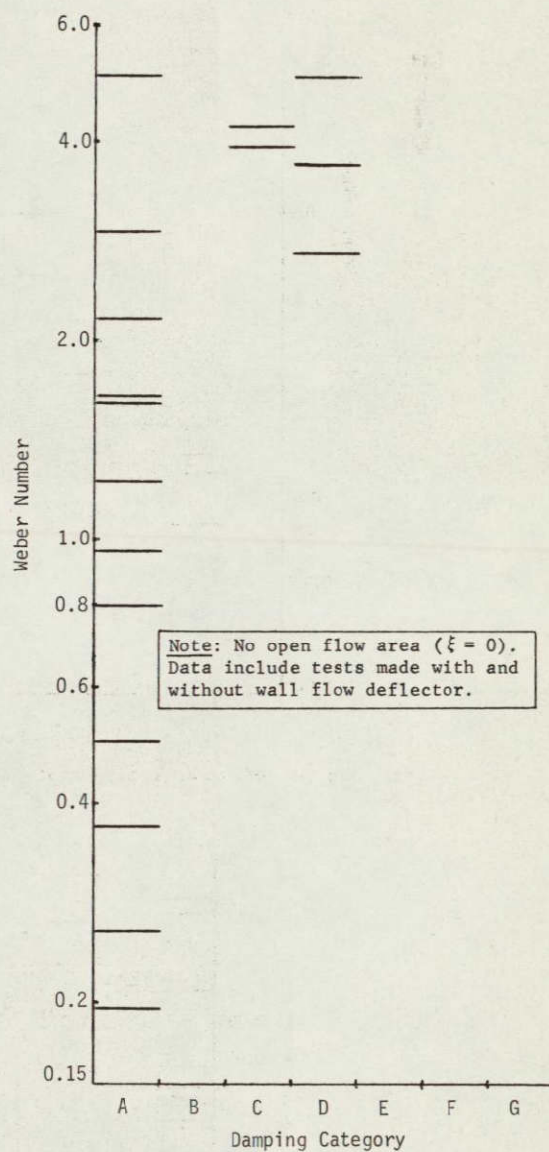


Fig. 42 Damping Performance of  
Double-Layer Perforated Plate Barriers



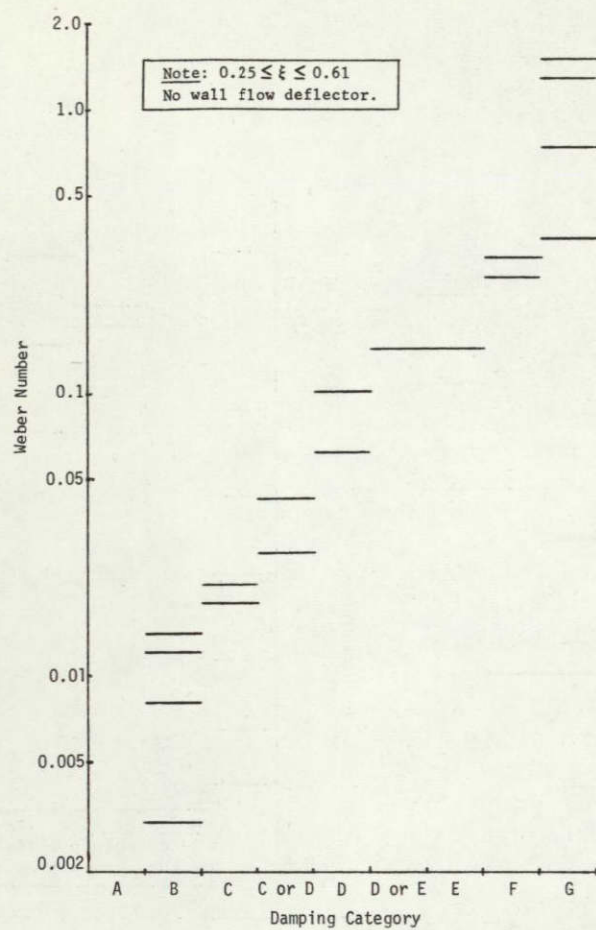


Fig. 43 Damping Performance of Single-Layer Square Weave Barriers

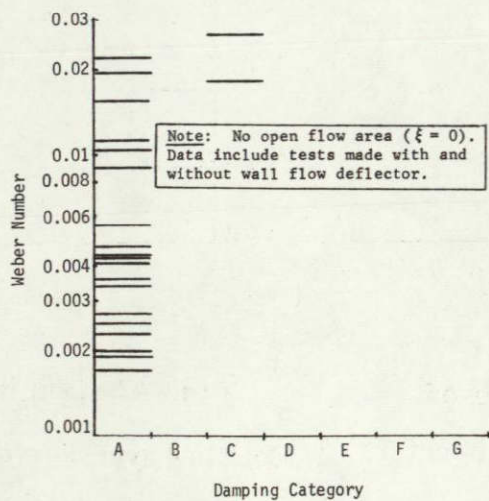


Fig. 44 Damping Performance of Single-Layer Dutch Twill Barriers

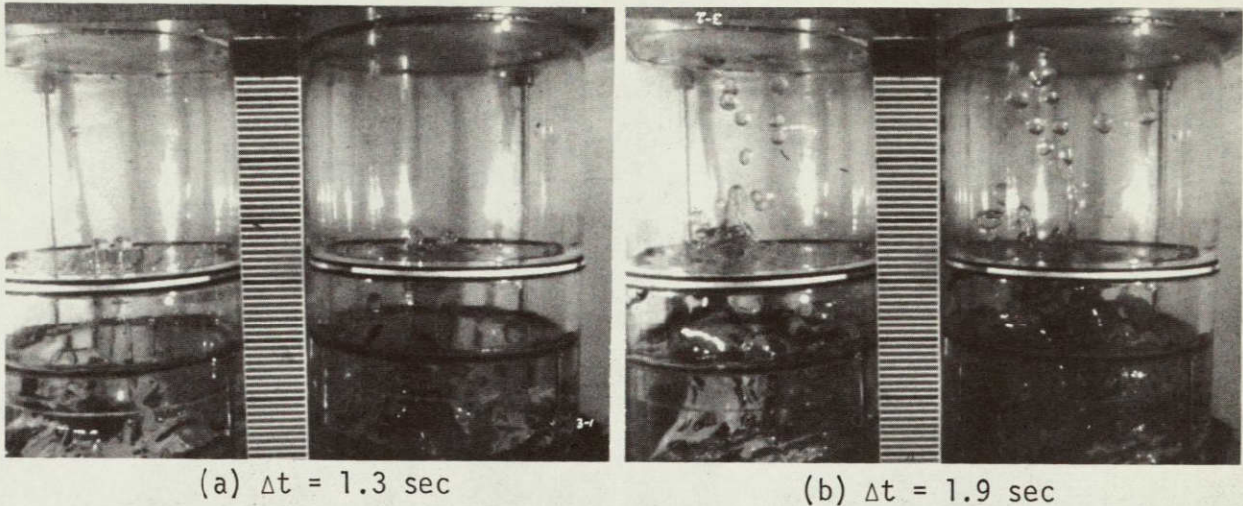


Fig. 45 Test Results for Run 23 (see Table 11)

with greater porosity afforded less restriction to the settled liquid, as shown in Fig. 46. The test specimen on the left in the sequence contains Barrier 11; the other, Barrier 12. Barrier 11 ( $\xi = 0.106$ ) shows good damping performance (Category B), but Barrier 12 ( $\xi = 0.430$ ) does not (Category F). The B and F damping categories listed in Table 11 for Barrier 12 mean that in addition to the poor damping, Category F, some liquid passed through the barrier (Category B) due to wall flow. More data are needed to establish the effect on damping performance for values of  $\xi$  greater than 0.176 for the single-perforated plates.

The Dutch-twill barriers and the double-layer perforated barriers displayed Category A damping in nearly all tests (see Fig. 42 and 44). For both kinds of barriers,  $\xi = 0$ , i.e., there is no open area to flow normal to the flat barriers. The double-layer perforated plates were separated by an 0.087-in. gap and were skewed as shown in Fig. 31. The twilled cloth is woven in such a manner that liquid flowing through the material must proceed along a tortuous path, as shown in Fig. 47: the fluid must first flow into the cloth by entering between the tightly woven shuttle wires; after a  $90^\circ$  turn, the flow path is a capillary network between wires that leads to a second  $90^\circ$  bend; then the path continues between the shuttle wires out to the other surface of the cloth. As a result, both barriers, in addition to providing a tortuous path for fluid passage, also possess an internal capillary network that aids wetting of the barrier. Once wetted, this internal network tends to keep the barrier wetted and prevents it from drying out. A barrier that is not completely wetted offers a flow resistance only to the settled liquid. On the other hand, a wetted barrier separates the tank into discrete volumes, and the damping and control that result from the surface-tension force acting at the pores of the material, from



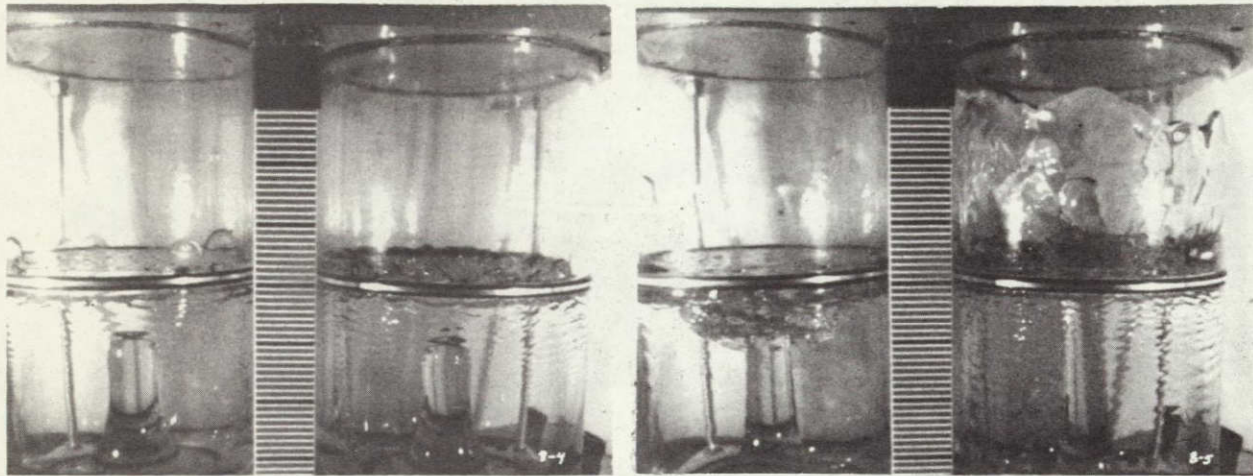
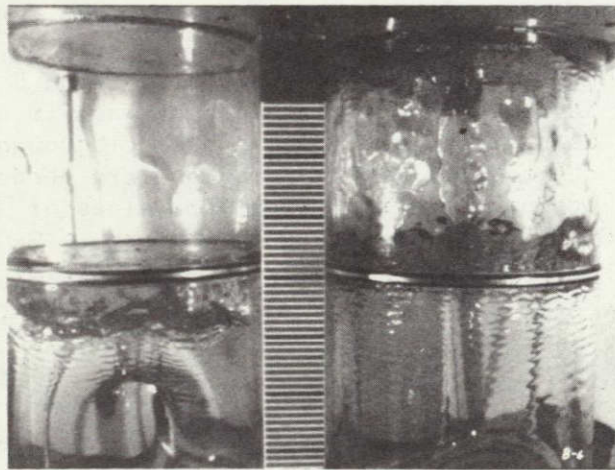
(a)  $\Delta t = 1.0$  sec(b)  $\Delta t = 1.5$  sec(c)  $\Delta t = 1.8$  sec

Fig. 46 Test Results for Run 37  
(see Table 11)

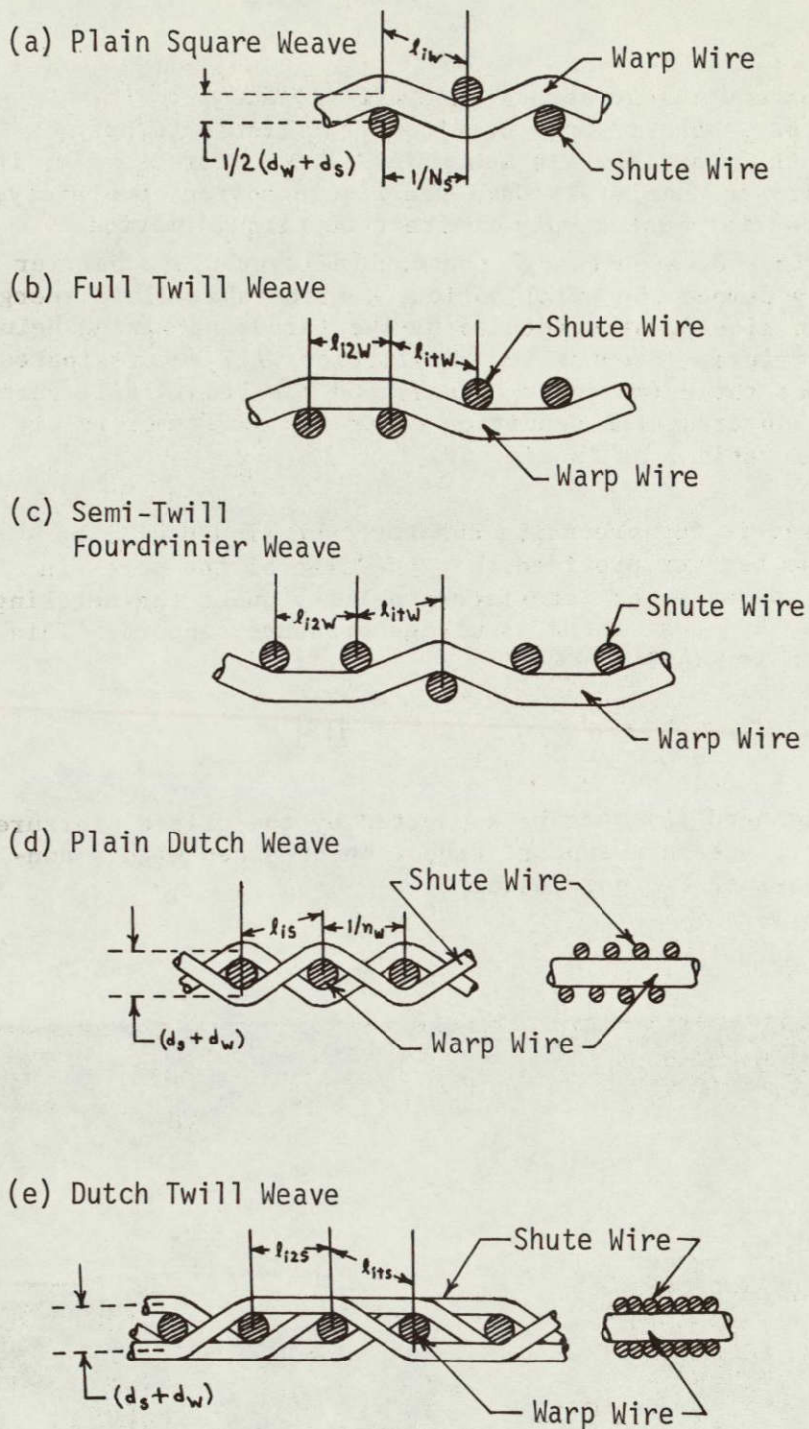


Fig. 47 Cross-Sectional Views of Various Screen Weaves  
(Ref. J. C. Armour and J. N. Cannon: "Fluid Flow Through Woven Screens," *AIChE Journal*, May 1968)



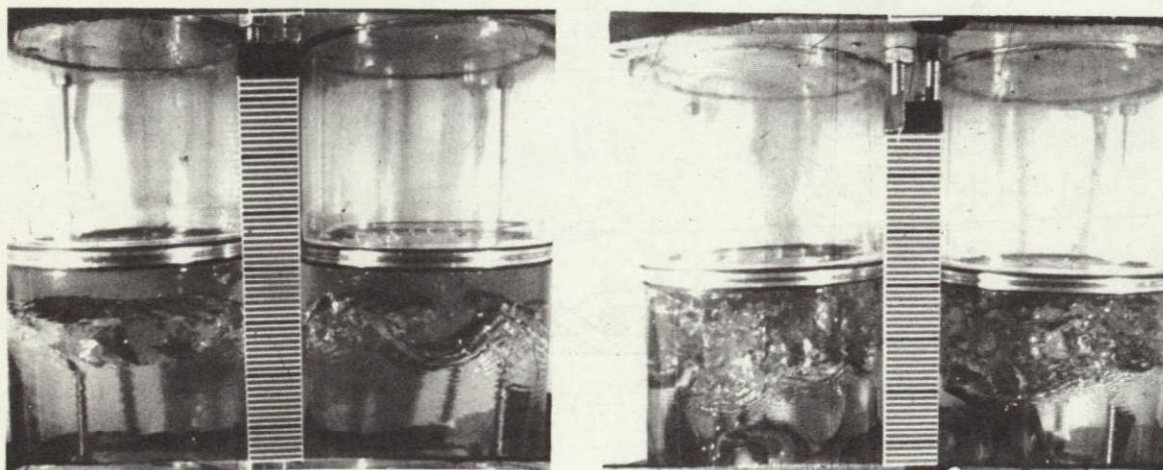
the ullage pressure change across the barrier, and from the viscous flow loss, make it more difficult for liquid to pass through the wetted barrier. As shown in Fig. 48, for example, it is not necessary to completely damp the liquid motion completely; instead, the barrier must simply redirect the liquid motion.

As shown in Fig. 48, even though the double-layer plate barrier has completely damped the axial motion, considerable fluid energy remains in the liquid, as evidenced by the turbulent mixing below the wetted barriers. Eventually, this motion will be dissipated through viscous shear (momentum change) and the liquid will reach the quiescent, hydrostatic condition under the axisymmetric settling acceleration, as in Fig. 49.

As discussed in the preceding chapter, the liquid will be contained by the barrier provided that the size of the pores in the barrier is adequate for interface stability under the settling acceleration,  $a$ , and that there is ullage pressure support. This latter criterion is simply:

$$P_o - P_1 \geq \rho \frac{a}{g_c} L; \quad [19]$$

i.e., the liquid head ( $L$ ) must be supported by the ullage pressure difference. This pressure support cannot be obtained with a non-wetted barrier, since  $P_o$  would equal  $P_1$ .



(a)  $\Delta t = 1.9$  sec

(b)  $\Delta t = 1.9$  sec

Fig. 48 Test Results for Runs 38 (on left) and 56 (see Table 12)



Typical damping results for the preferred double-plate and twilled-cloth barriers are presented in Fig. 48 and 50. Figure 48 shows Category A damping for the plate configuration, Runs 38 and 56 (Table 12). Typical performance of the screen barriers, Runs 48, 49, 50 and 64 (Table 16), is pictured in Fig. 50. In Run 48, there is a 325 x 2300-mesh screen in the left cylinder and a 200 x 1400-mesh screen in the right one. In Runs 49, 50, and 64, there is a 165 x 800-mesh screen in the left cylinder and a 50 x 50-mesh square-weave screen in the one on the right. (The relatively poor damping performance shown in Runs 50 and 64 is typical of that for square-weave screens. Only Run 49 produced fairly good results, Category B damping.) Figure 50 shows the Category A damping achieved for the twilled cloth barriers in

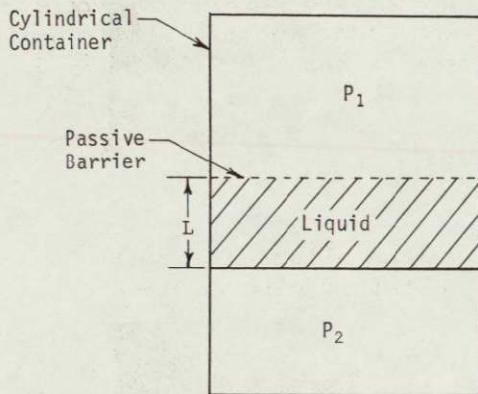


Fig. 49 Hydrostatic Condition Following Damping

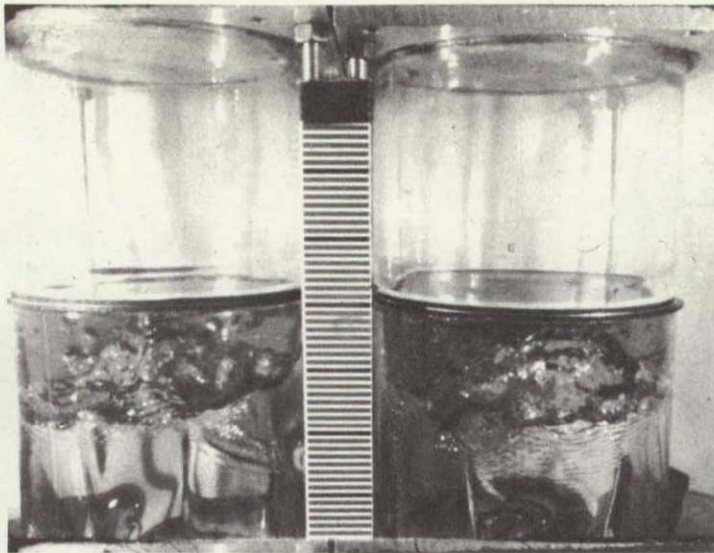
all but two drop tests (see Table 16). It is interesting to note that the Category C damping observed at  $We = 0.018$  (see Fig. 44) compares to that for the single square-weave screen (Fig. 43).

Although the effects of gap distance and  $\xi$  were not determined for the double-layer perforated-plate configuration, it would appear that since the gap distance can be varied, this configuration may be preferred over the twilled cloth barrier due to tank loading considerations. Wicking of the twilled cloth, even under one-g, tends to present problems of trapped, unwanted gas pockets

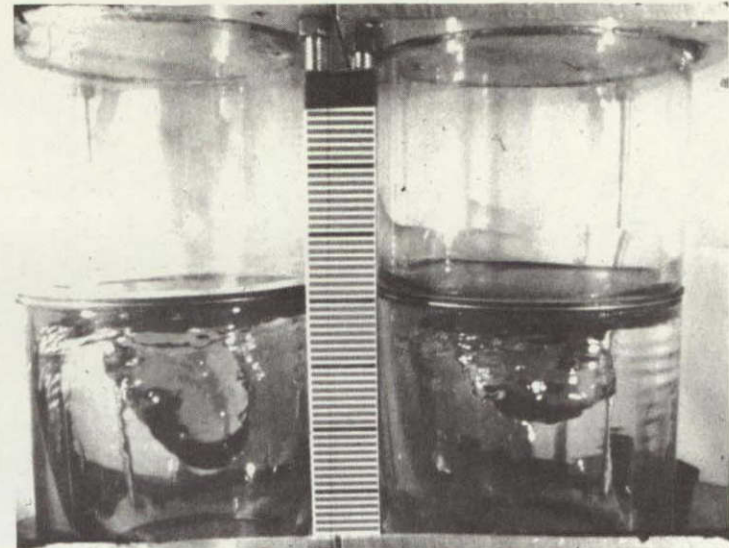
during loading, since the size of the internal capillary network is on the order of microns.

The damping performance of single-layer square-weave screens is listed in Table 13; that of double-layer square-weave screens in Table 14. As shown in Table 7, the double-layer square-weave screens were separated by an 0.087-in. gap; little or no improvement in performance was observed with the double-layer over the single-layer configuration. For example, Barrier 23, a 12 x 12-mesh single-layer screen, and Barrier 22, a 12 x 12-mesh double-layer screen, showed essentially the same, poor damping performance at comparable  $We$  numbers (for Runs 59 and 68,  $We \approx 1.4$ , and for Runs 63 and 70,  $We \approx 0.09$ ).

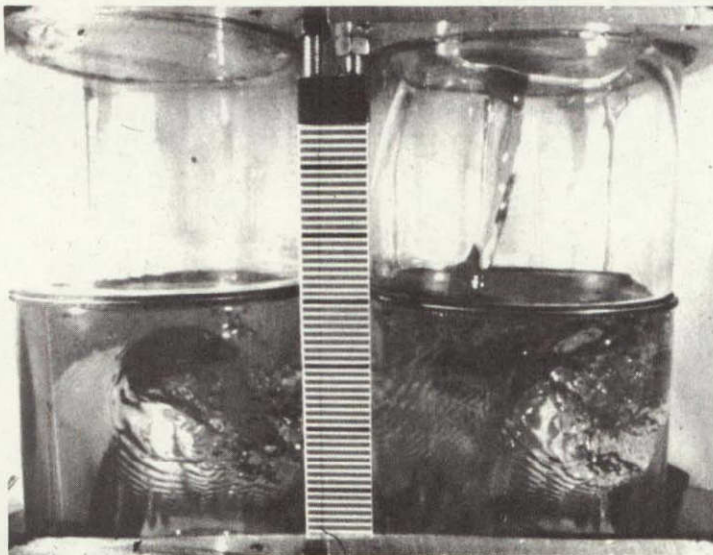




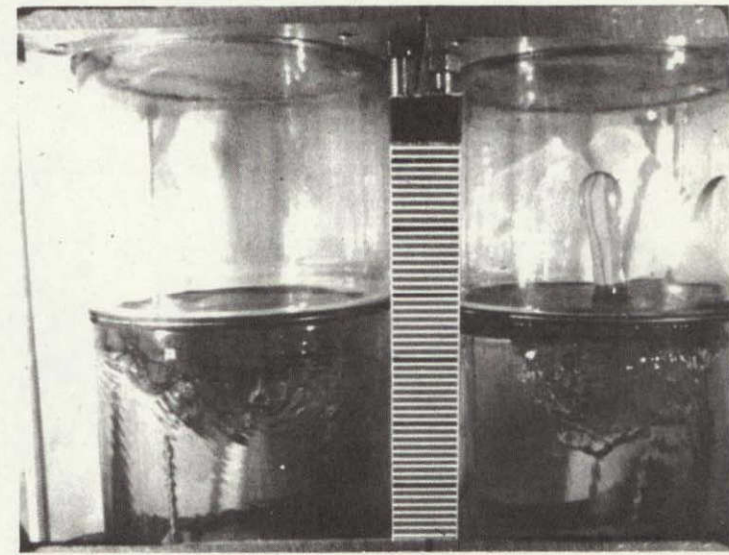
(a) Run 48;  $\Delta t = 1.9$  sec  
(325 x 2300 Mesh on Left; 200 x 1400 on Right)



(b) Run 49;  $\Delta t = 1.9$  sec  
(165 x 800 on Left; 50 x 50 on Right)



(c) Run 50;  $\Delta t = 1.9$  sec  
(165 x 800 on Left; 50 x 50 on Right)



(d) Run 64;  $\Delta t = 1.9$  sec  
(165 x 800 on Left; 50 x 50 on Right)

Fig. 50 Typical Screen Containment Results



The single-tube and multitube barriers (see Fig. 32, 33 and 34) were studied: (1) to evaluate the effect of plate thickness; and (2) to evaluate the feasibility of using one or more tubes that would extend into the liquid reservoir to effect a hydrostatic, rather than a hydrodynamic, control condition. The effect of plate thickness was studied by positioning many tubes flush with the bottom of the baffle plate (Fig. 32). Other tests were made with the tubes extending below the baffle but not in contact with the liquid before the test (Fig. 32). One drop test was made with a single tube in contact with the liquid.

The single-tube and multitube designs were not given serious consideration, primarily because they are heavier and more complex than the double-plate and Dutch-twill configurations. As a result, only four tests were made (Table 15). The test results shown for Run 46 (see Fig. 51) were typical of those for the multitube configuration. In Fig. 51, Barrier 15 is on the left and Barrier 16 on the right; poor damping (Category F) was obtained. Barrier 15 and 16 did not protrude below the baffle-plate (Table 6). Barriers 5 and 6 did; however their performance was equally poor (Categories G and F) as summarized in Table 15.

Additional test results were obtained to evaluate plate thickness (pore length) effects using single perforated plates. Plates were tested whose thickness ranged from 0.032 to 0.125 in. and whose pore size was the same (Table 6). For example, Barrier 1 was 0.087 in. thick, Barrier 1A was 0.032 in. thick, and Barrier 1B was 0.125 in. thick. The pore diameter was 0.125 in. for these three barriers. Damping performance, as presented in Table 15, appeared to be unaffected, however.



Fig. 51 Test Results for Run 46,  $\Delta t = 1.9$  sec  
(see Table 15)



The single test made with the single-tube barriers (No. 7 and 8, Table 6) was a zero-g test. The single tubes were in contact with the test liquid before the capsule was dropped. The test did produce an interesting phenomenon. During the 1 hr period between filling the test specimens with methanol and the dropping of the capsule, the vapor pressure of the methanol pumped liquid up the tubes into the upper ullage region. Prior to capsule release there was about  $\frac{1}{2}$  in. of liquid above each baffle. No additional liquid was pumped from the reservoir into the ullage above the tube during the test since the distance the liquid rose in the tube as a result of capillary pumping was limited by a resultant increase in the ullage pressure above the tube. The liquid pumping observed, however, would tend to preclude consideration of this type of barrier for propellant storage applications.

The pie-tin barrier configuration is shown in Fig. 35. Due to the magnitude of the experimental effort expended during this qualitative program, only two tests were made to assess the effect of barrier shape on liquid control. The barrier was positioned in the cylindrical specimens so that liquid flowing up the wall during settling would be redirected into the central liquid column, thus tending to dissipate its energy. Although our results were inconclusive, this type of barrier configuration is considered attractive: the solid portions of the barrier tend to redirect the wall and central-liquid-column flow, and the perforated annular region permits pressurization gas to enter the compartment (below the barrier) and expel liquid on demand.

The method suggested in Ref 18 for single-sample experiments was used to estimate the reliability of the test results. The settling Bo calculation is similar to that described in the previous chapter. Substituting the average values and uncertainty intervals from Table 17 for each of the variables provided the following Bo uncertainty limits at the three nominal low-g test conditions: 5.5% at 0.040g; 5.8% at 0.031g; and 6.5% at 0.022g. The reliability of the impingement we was calculated in a similar manner:

$$\frac{w_{We}}{We} = \left[ \left( \frac{w_{\sigma}}{\sigma} \right)^2 + \left( \frac{w_{\rho}}{\rho} \right)^2 + \left( \frac{2w_v}{v_c} \right)^2 + \left( \frac{w_r}{r} \right)^2 \right]^{\frac{1}{2}}, \quad [20]$$

for We based on pore radius, r. The average values and their uncertainty intervals are presented in Table 18. The uncertainty interval for the liquid-column velocity, as determined with the Boscar ballistic film analyzer and recorder (Model N-1) and from



Table 17 Uncertainty Intervals for Pertinent Variables Used to Calculate  $B_o$ 

VARIABLE	SYMBOL	AVERAGE VALUE	UNCERTAINTY INTERVAL ( $\pm w$ )
REPRESENTATIVE OF 0.040-g CONDITION			
Accelerating Force	$f_N$	11.0 $lb_f$	0.25 $lb_f$
Mass of Test Cell	M	274.0 $lb_m$	1.0 $lb_m$
Liquid Density	$\rho$	49.4 $lb_m/ft^3$	0.5 $lb_m/ft^3$
Surface Tension	$\sigma$	22.6 dyne/cm	1.0 dyne/cm
Radius of Cylinder	R	2.485 in.	0.030 in.
REPRESENTATIVE OF 0.031-g CONDITION			
Accelerating Force	f	8.5 $lb_f$	0.25 $lb_f$
REPRESENTATIVE OF 0.022-g CONDITION			
Accelerating Force	f	6.0 $lb_f$	0.25 $lb_f$

Table 18 Uncertainty Intervals for Pertinent Variables Used to Calculate Impingement  $We$ 

VARIABLE	SYMBOL	AVERAGE VALUE	UNCERTAINTY INTERVAL ( $\pm w$ )
Liquid Density	$\rho$	49.4 $lb_m/cu\ ft$	0.5 $lb_m/cu\ ft$
Surface Tension	$\sigma$	22.6 dyne/cm	1.0 dyne/cm
Liquid Velocity	$v_c$	1.8 in./sec	0.1 in./sec
Pore Radius	r	0.625 in.	0.003 in.



time histories determined from timing pips (20 pps) on the 16-mm film, is estimated to be less than  $\pm 0.1$  in./sec over the range of velocities obtained (1.9 to 6.5 in./sec). The velocity term is the critical variable. The We uncertainty limits determined using Eq [20] are less than 13.0%, based on the values listed in Table 18.

Although the test results are qualitative for the schemes evaluated, they do show that capillary barriers are feasible for controlling liquid propellants. The two most promising configurations tested were the double-plate and Dutch-twill barriers. Passive barriers using these types of foraminous material are recommended.

More data are needed to provide quantitative results. For example, with the double-plate configuration, additional testing is required to assess the effect of gap thickness, hole size, and open area on liquid-control performance. However, the data do show the importance of the We number and the need for the foraminous material to redirect the liquid and wet the barrier to provide propellant control.

## V. LIQUID/GAS INTERFACE STABILITY (ACCELERATION PARALLEL TO FORAMINOUS SURFACE)

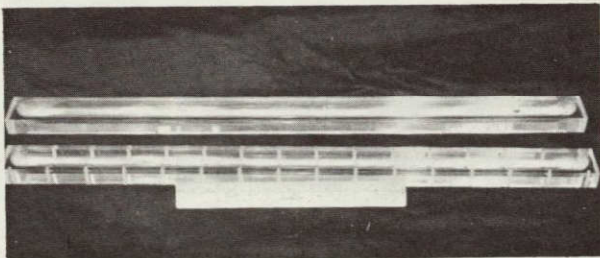
### A. OBJECTIVES

The stability of the liquid/gas interface at the surface of foraminous material has been investigated by Paynter (Ref 25), Hollister (Ref 26), and Gille (Ref 27), who performed simple bench tests either under a 1-g lateral acceleration or with the gravitational acceleration vector normal to the material. The purpose of this experimental phase of the current program was to evaluate the interface stability at the surface of perforated plates and screens over a range of lateral accelerations, with a near-zero acceleration normal to the material.

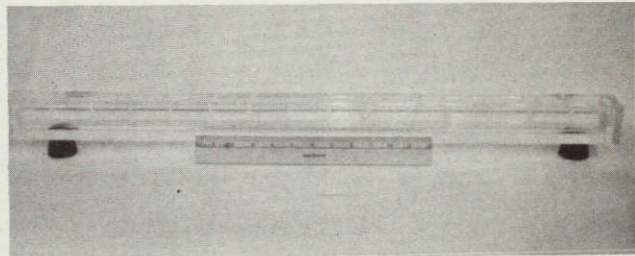
When designing a capillary device, stability under a lateral acceleration is usually more critical than when the acceleration is normal to the foraminous surface, since, in the former, only the surface tension tends to stabilize the fluid interface.

### B. EXPERIMENTAL APPARATUS AND TEST PROCEDURE

A series of bench tests was made before the drop tests using the Plexiglas model pictured in Fig. 55. An 11/16-in.-diameter ball-type end mill was used to machine the two Plexiglas halves into a 30-in.-long hollow cylinder of near-circular cross-sectional area. Different foraminous materials were then sandwiched between the halves for each test (see Fig. 56).



(a) Unassembled



(b) Assembled

Fig. 52 Plexiglas Model for 1-g Lateral Stability Tests



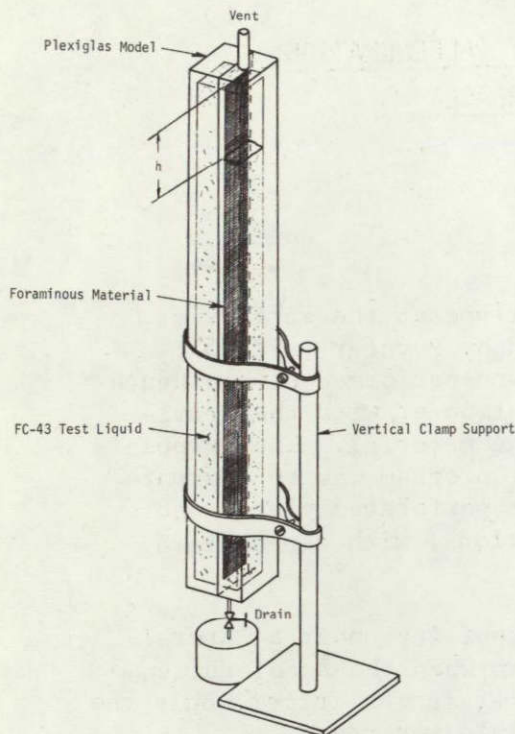


Fig. 53 Bench Test Setup

samples were clamped horizontally between two 4.970-in.-I.D. cylinders and the cylindrical specimen was then mounted on the lateral travel mechanism. During the 2.1-sec free-fall, the lateral mechanism was accelerated by constant-torque NEG'ATOR motors. The scale and pointer setup shown in Fig. 54 was used to measure the lateral travel. The test results were recorded on 16-mm color film at approximately 200 frames per second; timing pips imposed on the film at 20 pps were used to determine the exact film speed.

The activation of the lateral accelerator mechanism was delayed until about 0.75 sec after drop initiation for two reasons: (1) the duration of the lateral travel test, limited by the lateral travel distance, was less than 1 sec; and (2) zero-g was desired prior to initiating the lateral travel.

However, the results of the first tests showed that a lateral travel distance greater than 2.2 in. was required, along with an 1/8 to 1/4 in. liquid cover above the barrier (to ensure that the barrier was wetted when the capsule was dropped), to obtain

\*FC-43 is a fluorochemical liquid compatible with Plexiglas that is commercially available from Minnesota Mining and Manufacturing Co, St. Paul, Minnesota. It has a density of  $117 \text{ lb}_m/\text{ft}^3$ , a surface tension of  $1.097 \times 10^{-3} \text{ lb}_f/\text{ft}$ , and a viscosity of  $0.0032 \text{ lb}_m/\text{ft-sec}$  at  $20^\circ\text{C}$  (Ref 28).

After the samples were cleaned in a detergent solution and degreased with vapor, the fixture was completely filled with test liquid (FC-43)\* and was positioned vertically (upright) so that the acceleration vector would act parallel to the foraminous surface.

The tests were initiated by simultaneously venting and draining one side (gravity drain) of the model. The liquid flowrate ranged from about 0.1 to 6.7 ml/sec. The hydrostatic head,  $h$  (see Fig. 53), across the material at breakdown was measured.

The initial drop tests were conducted using a mechanism (see Fig. 54) whose lateral travel was limited to about 2.2 in. All tests were made with an axial acceleration of zero. The clean foraminous



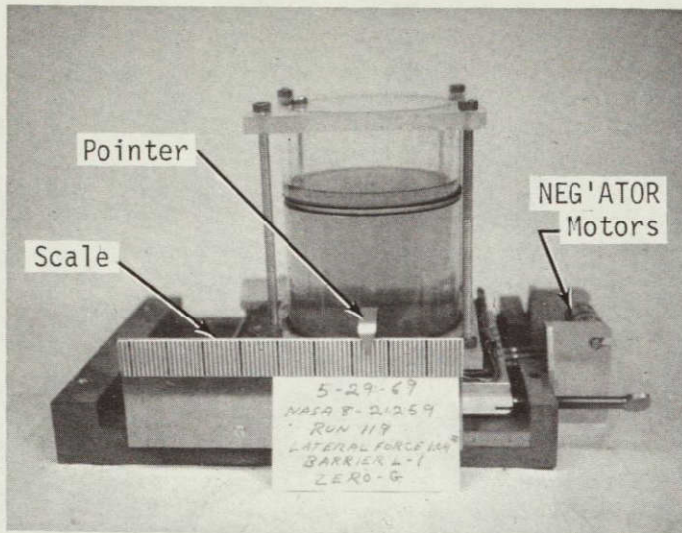


Fig. 54 Lateral Accelerator Mechanism  
(2.2 in. of travel)

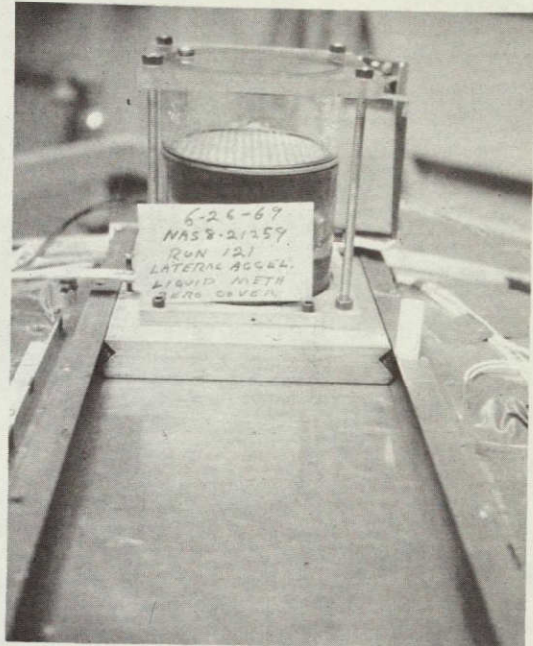


Fig. 55 Lateral Motion Device  
(approximately 15 in. of travel)

quantitative data. The 2.2-in travel distance made it difficult to determine whether breakdown occurred before, or at, the termination of the lateral motion. Consequently, a second mechanism, which provided about 15 in. of lateral travel, was used for the majority of the stability tests (this device is shown in Fig. 55); and instead of using a single cylindrical container, the box-like test specimen shown in Fig. 56 was used because it permitted us to evaluate two different barriers, or two liquids, during each drop.

The larger lateral mechanism required that the test be made with the device attached to the drag shield; the smaller inner capsule (test cell) could not be used. The test specimens were, as a result, subjected to a slight axial drag force during the drop. The magnitude of this axial acceleration (on the order of  $10^{-4}$  g) was negligible compared to the lateral accelerations that were imposed.

The test procedure was similar to that mentioned earlier. Lead weights were added to the test specimen, as required, to produce the desired lateral accelerations. The total mass accelerated by the NEG'ATOR motors ranged from 11.0 to 18.5 lb<sub>m</sub>. The scale and pointer setup used in the first series of drops to record the lateral travel was not satisfactory (the pointer relaxed and



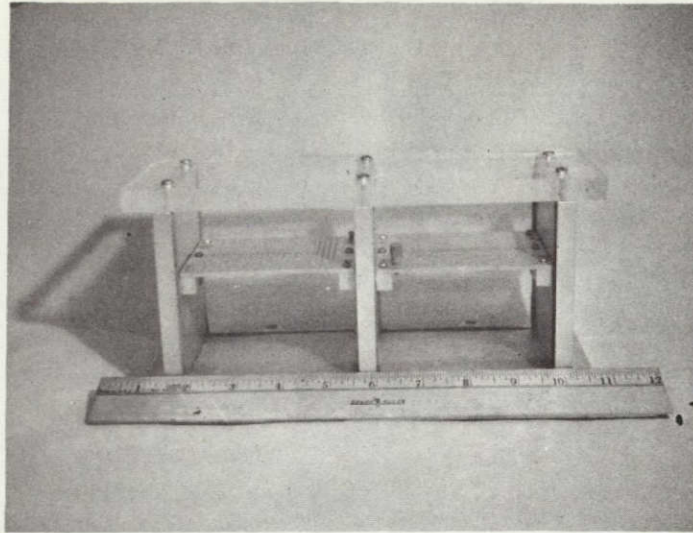


Fig. 56 Box-Like Test Specimen

bounced erratically during the test); it was replaced by a single light that was viewed by the camera. The neon bulb was triggered when magnetic reed switches positioned along the lateral travel guide rails made contact with the mechanism. The test results were photographically recorded using the reflector arrangement shown in Fig. 57. The 16-mm Milliken camera viewed the reflector directly. The test specimen, which was activated 0.75 sec after the capsule was released, travelled toward the reflector. Gas breakdown was clearly evident, since gas was ingested along the foraminous surface nearest the reflector.

### C. EXPERIMENTAL RESULTS

Referring to Fig. 58, a constant lateral acceleration,  $a_L$ , results in a hydrostatic pressure difference across the foraminous material. The maximum difference in liquid pressure is between the pores at Sta 1 and 2:

$$\Delta P_\ell = P_{\ell 1} - P_{\ell 2} = \rho_\ell \left( \frac{a_L}{g_c} \right) h_{12}. \quad [21]$$

Since the ullage pressure is constant, the interfacial pressure difference at the pore (Sta 1) is greater than that at Sta 2.

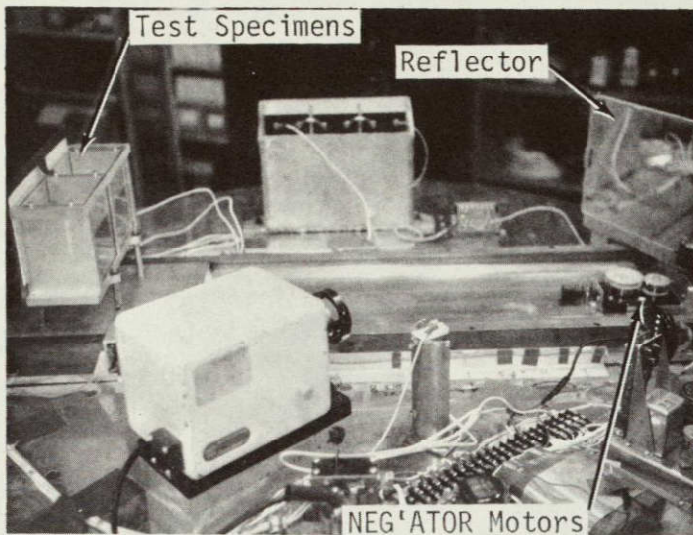


Fig. 57 Box-Like Test Specimen Positioned on Lateral Travel Mechanism

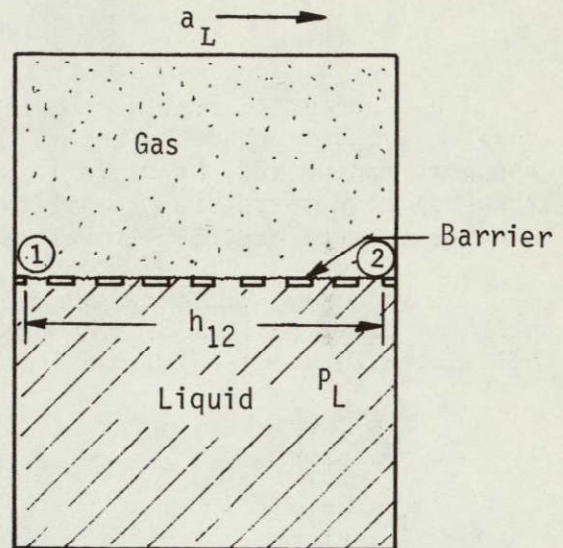


Fig. 58 Pressure Retention Under Lateral Acceleration

If we assume that the circular pore sizes are identical, each provides a capillary pressure difference

$$\Delta P_C = \frac{2\sigma}{b} \cos \theta, \quad [22]$$

which is maximum when  $b$ , the radius of curvature of the interface, is equal to the pore radius ( $b = r$ ). The capillary support must, therefore, be sufficient to stabilize the interface at Sta 1 or gas entering at Sta 2 will cause liquid to be lost through pores at Sta 1.

One of the stability criteria, therefore, may be expressed as:

$$(\Delta P_C)_{\max} \geq \rho_l \left( \frac{a_L}{g_c} \right) h_{12}; \quad [23]$$

and since the capillary and hydrostatic pressure differences act on the same area (i.e., the pore opening), we can express the ratio of the acceleration-to-capillary forces as

$$\phi = \frac{\rho_l a_L h r}{2\sigma g_c \cos \theta}; \quad [24]$$

or more simply, as

$$\phi = \frac{a_L h r}{\beta} \quad \Phi. \quad [25]$$



The  $\phi$  number is similar to the  $Bo$  number discussed in previous chapters, except that the lateral dimension,  $h$ , is not necessarily the pore radius ( $r$ ), as it is for  $Bo$ . Previous studies (Ref 23 thru 25) have correlated stability results against the acceleration-to-capillary force ratio.

A dimensional analysis was performed to determine other significant dimensionless scaling parameters. The following six variables were included in the analysis:

- $v_L$  = lateral velocity of the system (parallel to foraminous barrier);
- $a_L$  = acceleration of the system (parallel to foraminous barrier);
- $d$  = diameter of barrier pore;
- $h$  = uncovered length of barrier in direction of acceleration;
- $\nu$  = kinematic viscosity of test liquid; and
- $\beta$  = kinematic surface tension of test liquid.

Through the use of the Buckingham Pi Theorem, these variables might have been combined into four dimensionless groups in any of 15 ways. However, of the many combinations possible using this theorem, only 17 unique dimensionless groups can be generated. Five of these groups have been previously defined:

- 1)  $\frac{ad^2}{\beta}$  = Bond number (the ratio of the acceleration to the surface-tension forces);
- 2)  $\frac{v^2d}{\beta}$  = Weber number (the ratio of the inertia forces to the surface-tension forces);
- 3)  $\frac{vd}{\nu}$  = Reynolds number (the ratio of the inertia forces to the viscous forces);
- 4)  $\frac{v^2}{ad}$  = Froude number (the ratio of the inertia forces to the gravitational forces); and
- 5)  $\frac{ad^3}{\nu^2}$  = Galileo number (the product of the Reynolds number and the ratio of the gravitational forces to the viscous forces).

A sixth group,  $d/h$ , the ratio of the pore size to the uncovered barrier length in the direction of acceleration, was also considered important for the drop tests. The remaining groups, though they have no formal definitions, were investigated but produced no useful results.

The results showed that the Froude number was essentially a constant ( $Fr > 1$ ), which indicated that acceleration forces, rather than viscous forces, were dominant in the system. We concluded, therefore, that a dimensionless group containing an acceleration term would tend to offer a more appropriate representation of the effects of system motion. Accordingly, our consideration of the Weber and Reynolds numbers was dropped in favor of the Galileo number.

To reflect the influence of the lateral dimension in the direction of acceleration, the Galileo number was divided by the dimensionless ratio  $d/h$  to form the modified Galileo number:

$$Ga = \frac{ad^2h}{v^2} ; \quad [26]$$

and in addition to investigating the  $\emptyset$  number, we also determined the significance of the modified Galileo number in predicting the stability of the liquid/gas interface.

A description of the foraminous samples and the results for the bench tests are presented in Table 19. Where a variation in  $h$  values was observed, minimum and maximum  $\emptyset$  numbers are presented. The  $\emptyset$  numbers were calculated using Equation [25] assuming  $\Phi = 1.0$ .

Five drop tests were conducted with straight-hole perforated plates, square-weave screens, and Dutch-twill screens. The 2.2-in. lateral travel mechanism was used in these tests, and a cover of methanol, ranging from 1/8 to 1/4 in. above the material (as noted), was provided. The test results for the foraminous samples described in Table 20 are presented in Table 21.

The foraminous barriers used in the drop tests conducted with the 15-in. lateral travel device are described in Table 22. Table 23 shows which barriers were studied in the various runs. The results for the 119 drop tests made with the 15-in. mechanism are presented in Table 24. The  $\emptyset$  number was calculated using Eq [25]. The modified  $Ga$  number was calculated from Eq [26]. The  $h$  dimension measured for each perforated sample is shown in Fig. 58. The pore diameter of each perforated plate and square-weave screen was measured using a microscope with a calibrated stage. A rep-



Table 19 One-g Lateral Stability Test Results

FORAMINOUS SAMPLE	$(\phi_{\max})^*$	$(\phi_{\min})^*$
0.024-in.-thick single-layer stainless steel plate with a 60° array of 0.026-in.-diameter holes on 0.043-in. centers.	1.66	1.30
Two 0.024-in.-thick stainless steel plates separated by a 0.020-in. gap. Each plate has a 60° array of 0.026-in.-diameter holes on 0.042-in. centers.	2.35	2.10
Single-layer 100x100-mesh stainless steel screen with 0.0055-in. pore openings.	1.66	1.66
Single-layer 150x150-mesh stainless steel screen with 0.0040-in. pore openings.	1.72	1.72
Single-layer 200x200-mesh stainless steel screen with 0.0033-in. pore openings.	1.83	1.80
Single-layer 165x800-mesh stainless steel screen with 0.00112-in. pore openings.	1.41	1.40
Single-layer 200x1400-mesh stainless steel screen with 0.000532-in. pore openings.	1.20	1.29
Single-layer 325x2300-mesh stainless steel screen with 0.00352-in. pore openings.	1.35	1.35
*Based upon $h_{\max}$ and $h_{\min}$		

Table 20 Foraminous Samples Used for Drop Tests  
(2.2 in. of Lateral Travel)

BARRIER	DESCRIPTION	r (ft)
L-1	Plexiglas plate with one row of 1/8-in.-diameter straight holes on 1/4-in. centers.	0.0052
L-2	200 x 200-mesh stainless steel square-weave screen.	0.000138
L-3	30 x 250-mesh stainless steel Dutch-twill-weave screen	0.000145
1-B	Aluminum plate with a 90° array of 1/8-in.-diameter straight holes on 1/4-in. centers.	0.0052

Table 21 Lateral Acceleration Test Results  
(2.2-in. Lateral Travel Device)

RUN	BARRIER	$a_L/g$	LIQUID LEVEL ABOVE BARRIER, (in.)	$\phi$	STABILITY
116	L-3	0.864	0.125	1.49	Yes
117	L-2	0.476	0.125	0.78	Yes
118	L-3	0.789	0.125	1.37	Yes
119	L-1	0.098	0.375	6.36	No
120	1-B	0.075	0.125	4.75	No

Table 22 Foraminous Samples Used for Drop Tests  
(15.0 in. of Lateral Travel)

BARRIER	DESCRIPTION	$r$ (ft)	OPEN-TO-CLOSED AREA (%) - $\xi$ *
1	Aluminum plate with a 90° array of 1/32-in.-diameter straight holes on 1/16-in. centers.	0.00137	22.2
2	Aluminum plate with a 90° array of 1/16-in.-diameter straight holes on 1/8-in. centers.	0.00268	22.7
3	Aluminum plate with a 90° array of 1/16-in.-diameter straight holes on 3/16-in. centers.	0.00259	9.5
4	Aluminum plate with a 90° array of 1/8-in.-diameter straight holes on 3/8-in. centers.	0.00521	11.5
5	Stainless steel plate with a 60° array of 0.026-in.-diameter cone holes on 0.042-in. centers.	0.00108	36.2
6	100 x 100-mesh stainless steel square weave screen.	0.000246	34.8
7	50 x 50-mesh stainless steel square weave screen	0.000442	28.1
8	30 x 250-mesh stainless steel Dutch twill weave screen.	0.000145	0
9	24 x 110-mesh stainless steel Dutch twill weave screen.	0.000180	0

\*Flow normal to the surface of the material.



Table 23 Barriers Used in Lateral Acceleration Tests

RUN NO.	BARRIER NO.								
	1	2	3	4	5	6	7	8	9
136	X	X							
137	X	X							
138	X	X							
139	X	X							
140	X	X							
141	X	X							
151	X	X							
152	X	X							
153	X	X							
154	X	X							
155	X	X							
156	X	X							
157	X	X							
158	X	X							
159						X	X		
160						X	X		
161						X	X		
162						X	X		
163								X	X
164								X	X
165								X	X
166								X	X
167								X	X
169								X	X
170						X	X		
171						X	X		
172						X	X		
173						X	X		
174							X		
175						X			
176							X		
177						X	X		
178	X	X							
179	X	X							
180	X	X							
182	X	X							
184	X	X							
185	X	X							
186	X	X							
187	X	X							
188	X	X							
189	X	X							
190	X	X							
191						X	X		
193						X	X		
194						X	X		
195								X	X
197								X	X
198								X	X
199								X	X
200								X	X
201								X	X
202								X	X
203	X	X							
204	X	X							
205	X	X							
206	X	X							
207	X	X							
208	X	X							
209	X	X							
210	X	X							
211						X	X		
212						X	X		
213						X	X		
214						X	X		
215						X	X		

Table 24 Lateral Acceleration Stability Test Results

(a) Barrier 1

RUN NO.	TEST LIQUID*	LATERAL ACCELERATION (ft/sec <sup>2</sup> )	h (ft)	Ø	Ga (x 10 <sup>-4</sup> )	STABILITY
136	F	1.31	0.200	0.87	8.70	Yes
137	F	1.82	0.200	1.20	12.1	Yes
138	F	2.10	0.200	1.38	13.9	Yes
139	M	3.04	0.200	0.83	5.45	Yes
140	M	4.20	0.200	1.14	7.50	Yes
141	M	5.44	0.200	1.48	9.70	Yes
151	F	4.32	0.200	2.85	28.8	No
152	F	4.88	0.200	3.62	32.6	No
153	F	5.93	0.200	3.91	39.4	No
154	F	7.00	0.200	4.61	46.5	No
155	M	6.68	0.200	1.81	11.9	Yes
156	M	8.00	0.200	2.17	14.2	Yes
157	M	8.47	0.200	2.30	15.1	No
158	M	10.05	0.200	2.73	17.9	No
178	M	7.72	0.200	2.09	13.8	No
179	M	8.45	0.200	2.29	15.1	No
180	M	10.25	0.200	2.78	18.3	No
182	F	3.24	0.200	2.14	21.6	Yes
184	F	3.56	0.200	2.35	23.7	No
185	F	3.66	0.200	2.42	24.4	No
186	F	4.32	0.200	2.85	28.8	No
187	CT	5.01	0.200	2.31	18.0	No
188	CT	5.18	0.200	2.39	18.6	No
189	CT	6.08	0.200	2.80	21.7	No
190	CT	7.10	0.200	3.27	25.6	No
203	M	9.76	0.143	1.89	12.4	Yes
204	M	10.90	0.143	2.12	13.9	Yes
205	M	12.90	0.143	2.50	16.4	No
206	M	13.60	0.143	2.64	17.3	No
207	F	5.02	0.143	2.37	23.8	No
208	F	5.17	0.143	2.44	24.4	No
209	F	5.95	0.143	2.81	28.3	No
210	F	7.10	0.143	3.36	33.7	No

\*Liquid designations: F = Freon-TF;  
M = methanol;  
CT = carbon tetrachloride.

(b) Barrier 2

RUN NO.	TEST LIQUID*	LATERAL ACCELERATION (ft/sec <sup>2</sup> )	h (ft)	Ø	Ga (x 10 <sup>-4</sup> )	STABILITY
136	F	1.31	0.087	0.74	14.5	Yes
137	F	1.82	0.087	1.03	20.1	Yes
138	F	2.10	0.087	1.18	23.2	Yes
139	M	3.04	0.70	0.70	9.00	Yes
140	M	4.20	0.087	0.97	12.4	Yes
141	M	5.44	0.087	1.25	16.0	Yes
151	F	4.47	0.087	2.52	49.8	No
152	F	5.20	0.087	2.94	57.5	No
153	F	5.98	0.087	3.36	66.3	No
154	F	7.00	0.087	3.95	77.5	No
155	M	6.68	0.087	1.55	19.8	Yes
156	M	8.40	0.087	1.95	24.9	Yes
157	M	9.28	0.087	2.15	27.6	Yes
158	M	10.05	0.087	2.33	29.8	No
178	M	8.40	0.087	1.95	24.9	Yes
179	M	9.28	0.087	2.15	27.6	Yes
180	M	10.87	0.087	2.52	32.3	Yes
182	F	3.24	0.087	1.83	36.0	Yes
184	F	3.56	0.087	2.00	39.6	Yes
185	F	4.05	0.087	2.28	45.0	No
186	F	4.85	0.087	2.74	54.0	No
187	CT	5.01	0.087	2.01	30.0	Yes
188	CT	5.88	0.087	2.32	35.2	Yes
189	CT	6.08	0.087	2.37	36.2	No
190	CT	7.10	0.087	2.79	42.3	No
203	M	9.76	0.073	1.89	24.2	Yes
204	M	10.90	0.073	2.12	27.0	Yes
205	M	12.90	0.073	2.50	32.0	Yes
206	M	13.60	0.073	2.64	32.2	No
207	F	5.02	0.073	2.37	46.7	Yes
208	F	5.67	0.073	2.68	33.9	No
209	F	5.95	0.073	2.80	55.0	No
210	F	7.10	0.073	3.36	66.0	No

\*Liquid designations: F = Freon-TF;  
M = methanol;  
CT = carbon tetrachloride.



Table 24 (cont)

(c) Barrier 3

RUN NO.	TEST LIQUID*	LATERAL ACCELERATION (ft/sec <sup>2</sup> )	h (ft)	Ø	Ga (x 10 <sup>-4</sup> )	STABILITY
227	M	5.04	0.192	2.49	30.8	No
228	M	3.56	0.192	1.76	21.7	Yes
229	M	4.05	0.192	2.00	24.9	Yes
230	M	4.87	0.192	2.40	29.6	No
231	M	5.10	0.192	2.51	31.2	No
232	F	3.14	0.192	3.76	71.7	No
233	F	3.50	0.192	4.20	79.6	No
234	F	4.05	0.192	4.85	92.5	No
235	F	4.10	0.192	4.91	93.5	No
268	F	1.56	0.192	1.88	35.6	Yes
269	F	1.78	0.192	2.14	40.7	Yes
270	F	1.88	0.192	2.26	43.0	No
271	F	2.22	0.192	2.66	50.4	No

\* Liquid designations: M = methanol;  
F = Freon - TF.

(d) Barrier 4

RUN NO.	TEST LIQUID*	LATERAL ACCELERATION (ft/sec <sup>2</sup> )	h (ft)	Ø	Ga (x 10 <sup>-4</sup> )	STABILITY
227	M	5.04	0.104	2.70	67.3	No
228	M	3.56	0.104	1.91	47.7	Yes
229	M	4.05	0.104	2.17	54.3	Yes
230	M	4.87	0.104	2.62	65.2	Yes
231	M	5.10	0.104	2.74	68.3	No
232	F	3.14	0.104	4.10	157.0	No
233	F	3.50	0.104	4.57	175.0	No
234	F	4.05	0.104	5.30	202.0	No
235	F	4.10	0.104	5.35	205.0	No
268	F	1.56	0.104	2.04	77.9	Yes
269	F	1.78	0.104	2.32	88.9	Yes
270	F	1.88	0.104	2.46	93.8	No
271	F	2.22	0.104	2.90	111.0	No

\* Liquid designations: M = methanol;  
F = Freon - TF.

(e) Barrier 5

RUN NO.	TEST LIQUID*	LATERAL ACCELERATION (ft/sec <sup>2</sup> )	h (ft)	Ø	Ga (x 10 <sup>-4</sup> )	STABILITY
236	M	9.77	0.167	1.74	9.02	No
237	M	10.88	0.167	1.94	10.00	No
238	M	11.89	0.167	2.11	11.00	No
239	M	14.96	0.167	2.66	13.80	No
240	F	4.57	0.167	1.98	15.75	No
241	F	5.03	0.167	2.18	17.34	No
242	F	6.12	0.167	2.66	21.10	No
243	F	7.33	0.167	3.18	25.20	No
260L	M	6.74	0.167	1.20	6.22	No
260R	M	6.98	0.146	1.09	5.63	Yes
261L	M	8.00	0.167	1.43	7.37	No
261R	M	8.00	0.146	1.25	6.45	Yes
262L	M	10.30	0.167	1.83	9.50	No
262R	M	10.30	0.146	1.61	8.30	No
263L	M	10.50	0.167	1.87	9.68	No
263R	M	12.19	0.146	1.90	9.70	No
264L	F	3.15	0.167	1.37	10.83	Yes
264R	F	3.15	0.146	1.20	9.46	Yes
265L	F	3.35	0.167	1.45	11.54	Yes
265R	F	3.35	0.146	1.27	10.10	Yes
266L	F	3.74	0.167	1.62	12.89	No
266R	F	4.06	0.146	1.54	12.2	Yes
267L	F	4.45	0.167	1.93	15.30	No
267R	F	4.83	0.146	1.83	14.55	No

\* Liquid designations: M = methanol;  
F = Freon - TF.



Table 24 (cont)

(f) Barrier 6

RUN NO.	TEST LIQUID*	LATERAL ACCELERATION (ft/sec <sup>2</sup> )	h (ft)	$\phi$	Ga (x 10 <sup>-4</sup> )	STABILITY
150	F	12.1	0.176	1.27	2.29	No
160	F	14.0	0.176	1.46	2.58	No
161	F	19.0	0.176	1.98	3.58	No
162	F	16.2	0.176	1.69	3.06	No
170	M	20.9	0.176	0.90	1.05	Yes
171	M	22.6	0.176	0.97	1.14	Yes
172	M	26.7	0.176	1.14	1.35	Yes
173	M	28.3	0.176	1.21	1.43	No
175	F	9.11	0.176	0.95	1.72	No
191	CT	12.2	0.176	0.89	1.24	Yes
193	CT	16.8	0.176	1.22	1.71	No
194	CT	21.0	0.176	1.50	2.10	No
211	M	21.0	0.125	0.63	0.74	Yes
212	M	22.7	0.125	0.69	0.81	Yes
213	M	29.2	0.125	0.89	1.05	No
214	M	35.3	0.125	1.07	1.26	No
215	F	9.28	0.125	0.69	1.27	Yes
216	F	20.3	0.125	0.77	1.38	Yes
217	F	11.5	0.125	0.85	1.54	Yes
218	F	13.7	0.125	1.02	1.83	No

\*Liquid designations: F = Freon-TF;  
M = methanol;  
CT = carbon tetrachloride.

(g) Barrier 7

RUN NO.	TEST LIQUID*	LATERAL ACCELERATION (ft/sec <sup>2</sup> )	h (ft)	$\phi$	Ga (x 10 <sup>-4</sup> )	STABILITY
150	F	12.7	0.086	1.17	3.78	No
160	F	15.6	0.086	1.43	4.65	No
161	F	19.0	0.086	1.74	5.67	No
162	F	16.2	0.086	1.49	4.82	No
170	M	20.9	0.086	0.79	1.66	Yes
171	M	22.6	0.086	0.85	1.80	Yes
172	M	26.7	0.086	1.01	2.12	Yes
173	M	28.3	0.086	1.06	2.25	No
174	F	8.80	0.086	0.81	2.61	Yes
176	F	10.9	0.086	1.00	3.24	Yes
177	F	13.7	0.086	1.26	4.07	No
191	CT	12.2	0.086	0.78	1.96	Yes
193	CT	14.9	0.086	0.95	2.39	No
194	CT	21.0	0.086	1.34	3.37	No
211	M	21.0	0.0625	0.57	1.22	Yes
212	M	22.7	0.0625	0.62	1.31	Yes
213	M	29.2	0.0625	0.80	1.69	Yes
214	M	35.3	0.0625	0.96	2.04	No
215	F	9.28	0.0625	0.62	2.00	Yes
216	F	10.3	0.0625	0.69	2.22	Yes
217	F	11.5	0.0625	0.77	2.48	Yes
218	F	13.7	0.0625	0.91	2.96	Yes

\*Liquid designations: F = Freon-TF;  
M = methanol;  
CT = carbon tetrachloride.

Table 24 (concl)

(h) Barrier 8

RUN NO.	TEST LIQUID	LATERAL ACCELERATION (ft/sec <sup>2</sup> )	h (ft)	Ø	Ga (x 10 <sup>-4</sup> )	STABILITY
163	F	22.6	0.177	1.40	1.505	Yes
164	F	23.3	0.177	1.44	1.55	No
165	F	32.6	0.177	2.02	2.17	No
166	M	29.2	0.177	0.740	0.515	Yes
167	M	32.0	0.177	0.812	0.565	Yes
169	M	48.7	0.177	1.24	0.860	Yes
195	CT	24.6	0.177	1.06	0.879	Yes
197	CT	35.0	0.177	1.51	1.25	No
199	M	35.0	0.177	0.888	0.618	Yes
200	M	34.8	0.177	0.885	0.615	Yes
201	M	39.1	0.177	1.00	0.693	Yes
202	M	43.5	0.177	1.11	0.768	Yes
272	F	26.8	0.111	1.04	1.115	Yes
273	F	29.2	0.111	1.13	1.205	Yes
275	F	37.8	0.111	1.46	1.575	No

(i) Barrier 9

RUN NO.	TEST LIQUID	LATERAL ACCELERATION (ft/sec <sup>2</sup> )	h (ft)	Ø	Ga (x 10 <sup>-4</sup> )	STABILITY
163	F	22.6	0.087	0.853	1.14	Yes
164	F	24.6	0.087	0.925	1.24	Yes
165	F	32.6	0.087	1.23	1.64	No
166	M	29.2	0.177	0.917	0.795	Yes
167	M	32.0	0.177	1.01	0.870	Yes
169	M	42.9	0.177	1.35	1.17	No
195	CT	22.6	0.177	1.21	1.24	No
197	CT	35.0	0.177	1.87	1.92	No
198	CT	31.4	0.177	1.69	1.73	No
200	M	34.8	0.177	1.09	0.947	No
201	M	36.6	0.177	1.15	0.990	No
202	M	39.6	0.177	1.23	1.08	No
219L	M	24.6	0.104	0.455	0.392	Yes
219R	M	24.6	0.052	0.227	0.199	Yes
220L	M	26.7	0.104	0.493	0.426	Yes
220R	M	26.7	0.052	0.246	0.213	Yes
221L	M	35.6	0.104	0.658	0.570	Yes
221R	M	35.6	0.052	0.329	0.285	Yes
223L	F	10.9	0.104	0.490	0.655	Yes
223R	F	10.9	0.052	0.245	0.327	Yes
224L	F	12.2	0.104	0.550	0.732	Yes
224R	F	12.2	0.052	0.275	0.365	Yes
225L	F	14.7	0.104	0.662	0.883	Yes
225R	F	14.7	0.052	0.331	0.442	Yes
226L	F	16.8	0.104	0.755	1.01	Yes
226R	F	16.8	0.052	0.378	0.504	Yes
244L	F	18.0	0.052	0.405	0.540	Yes
244R	F	18.0	0.104	0.810	1.09	Yes
245R	F	17.9	0.104	0.810	1.08	No
246R	F	22.7	0.104	1.02	1.37	No
247R	F	32.1	0.104	1.44	1.93	No
272	F	26.8	0.0728	0.848	1.13	Yes
273	F	29.2	0.0728	0.923	1.23	Yes
274	F	35.3	0.0728	1.04	1.49	No
275	F	37.8	0.0728	1.20	1.60	No

MCR-69-585



representative number of holes was measured and the hole diameter was determined as the average of the two extreme diameters.

The twilled cloth has both warp and shute wires; the warp wires have larger diameters. This particular weave forms a dense material that has extremely small (micronic) and irregular passageways into the cloth. Since the openings are complex, and vary in size and shape, we did not measure the pore size of the twilled cloth as we did for the plates and square-weave screens. Instead, we used the conventional bubble-point technique to determine the absolute micron rating for each mesh size.

Bubble-point data for the twilled cloth samples used for test could not be directly determined due to limitations of the bubble-point test apparatus used; however, samples were taken from the same roll of screen. From these data and the absolute micron rating versus bubble point correlation\* an absolute micron rating was determined for each twilled-cloth specimen. The pore radii used for the calculations were one-half the absolute micron ratings (see Table 19, 20 and 22).

The average lateral accelerations listed in Tables 21 and 24, determined from the film data, as described earlier, were used to calculate the dimensionless parameters.

#### D. DISCUSSION OF TEST RESULTS

The bench tests were made in an attempt to narrow the range of the  $\emptyset$  number and to reduce the number of drop tests. As mentioned, the 2.2-in. travel mechanism used in the first five drop tests did not produce meaningful results and was replaced with a 15-in. mechanism.

The critical  $\emptyset$  number for the one-g lateral stability tests for single layer material ranged from 1.29 to 1.83 (Table 19). For the double-layer plate, it ranged from 2.10 to 2.33; for the single-layer perforated plates, from 1.30 to 1.66; for square-weave screen, from 1.66 to 1.83; and for the Dutch twill, from 1.20 to 1.41. The data were repeatable, and no noticeable effect was observed using different draining rates.

---

\*Bubble Test Spec. 207, Western Filter Company, Gardena, Calif.

Typical drop-test results, showing stability and instability at the liquid/gas interface, are presented in Fig. 59 and 60. The test liquids are carbon tetrachloride and methanol, respectively.

The results shown in Fig. 59 are from Run 195 (Table 24 - h and i) and are for 100x100 and 50x50-mesh screens. Note that the finer-mesh screen in the left cylinder provided a stable interface, but that continuous gas breakthrough was observed for the 50x50-mesh screen.

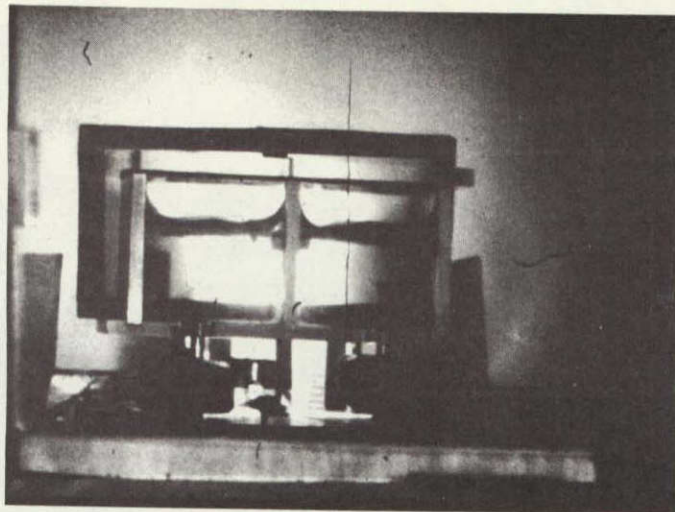
The results pictured in Fig. 60 are from Run 205 (Table 24 - a and b) and are for perforated plates. The barrier in the cylinder on the left had 1/32-in.-diameter holes; that in the cylinder on the right had 1/16-in.-diameter holes. The barrier with the 1/32-in. holes was unstable while the other perforated barrier provided a stable interface. The  $\emptyset$  numbers were identical for each ( $\emptyset = 2.50$ ).

Two types of gas ingestion were observed, i.e., continuous and non-continuous. The latter was either a single breakdown followed by an apparent stable condition, or vice-versa. We believe that the intermittent breakdowns resulted from variations in the lateral acceleration. The calculated accelerations showed that, in general, the acceleration on the test specimens decreased slightly due to frictional drag and resistance caused by irregularities in the parallel guide rails.

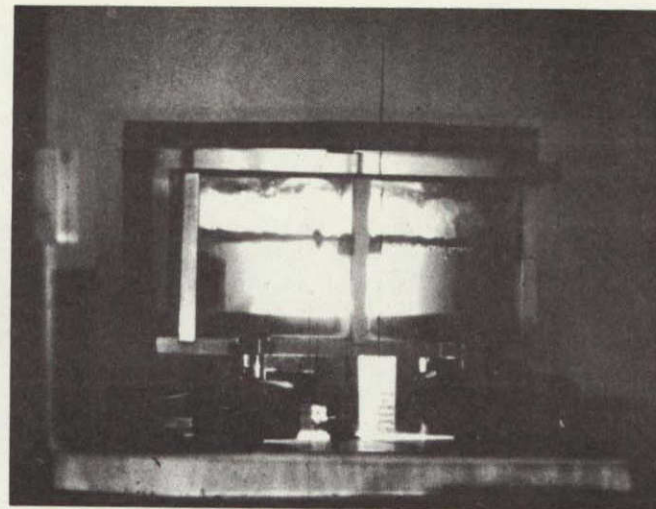
The method used to calculate the dimensionless numbers  $\emptyset$  and  $G_a$  was: (1) when the interface was stable, the highest calculated acceleration (between reed stations) was used; and (2) when the interface was unstable, either the lowest acceleration (for continuous gas breakthrough during the lateral travel) or the average acceleration to the reed switch following breakdown (for non-continuous breakdown) was used. The accelerations listed in Tables 21 and 24 reflect this procedure.

The  $\emptyset$  numbers listed in Table 24 are presented graphically in Fig. 61 thru 66. The  $h$  dimension is plotted against the term  $\beta/a_{Lr}$ . As a result, the straight line segments shown represent constant  $\emptyset$  numbers. Figures 61 and 62 are for perforated plates with constant-diameter drilled and reamed holes and with open-to-closed area ratios ( $\xi$ ) of approximately 11 and 23%, respectively. Figure 63 presents data for Perforated Plate 5 (Table 20), which has an  $\xi$  of 36.2%.





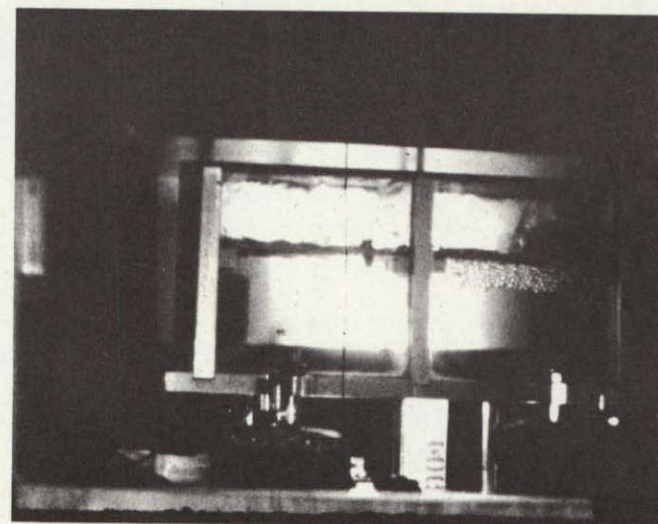
(a) Start of Lateral Acceleration ( $t = 0$  sec)



(b)  $\Delta t = 0.19$  sec

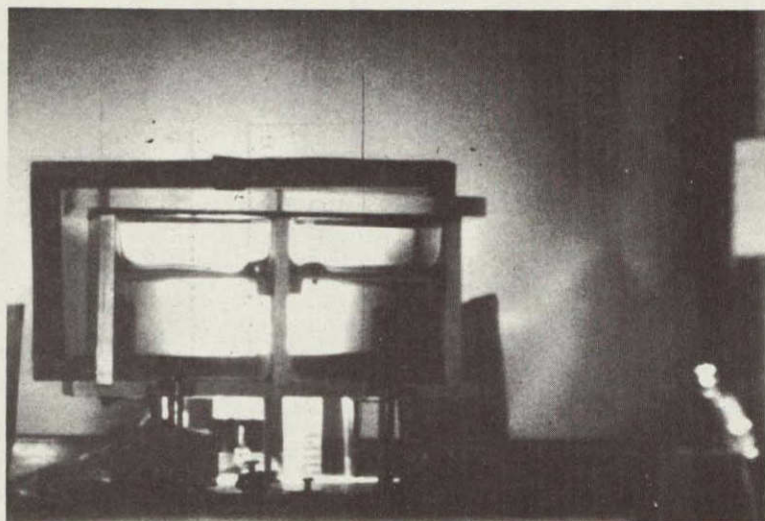


(c)  $\Delta t = 0.27$  sec

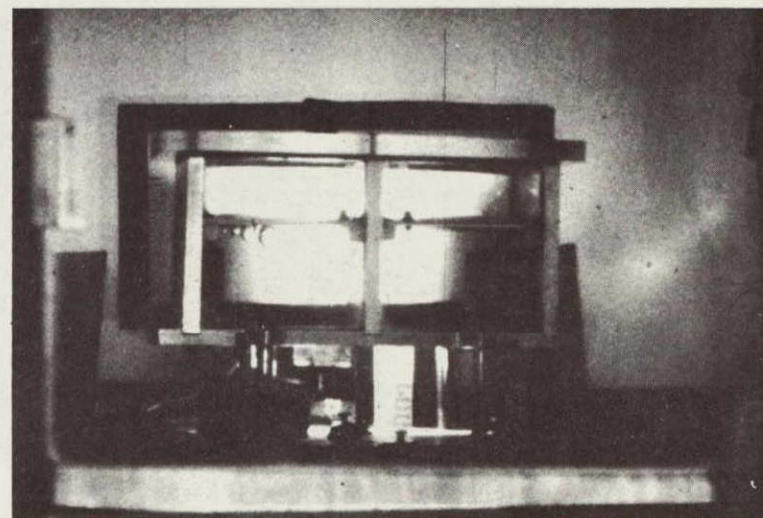


(d)  $\Delta t = 0.33$  sec

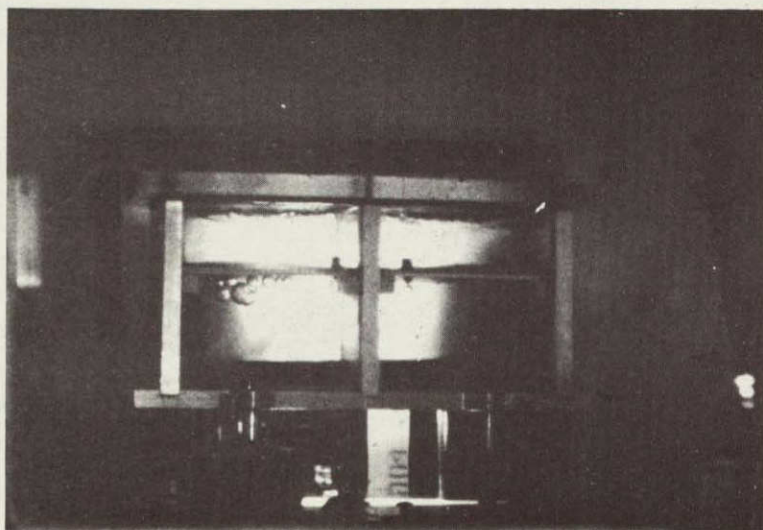
Fig. 59 Lateral Acceleration Test, Run 195 (See Table 24-h,i)  
Barrier 8 (on left) is stable; Barrier 9 is unstable.



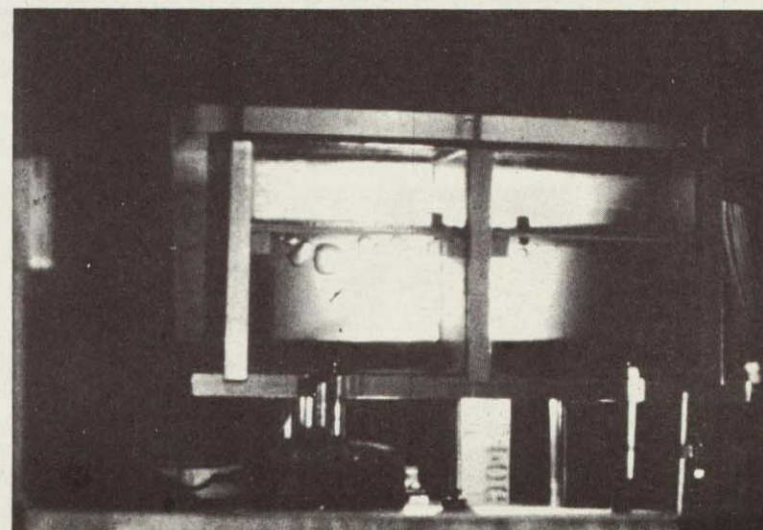
(a) Start of Lateral Acceleration ( $t = 0$  sec)



(b)  $\Delta t = 0.28$  sec



(c)  $\Delta t = 0.45$  sec



(d)  $\Delta t = 1.45$  sec

Fig. 60 Lateral Acceleration Test, Run 205 (See Table 24-a,b)  
Barrier 1 (on left) is unstable; Barrier 2 is stable.



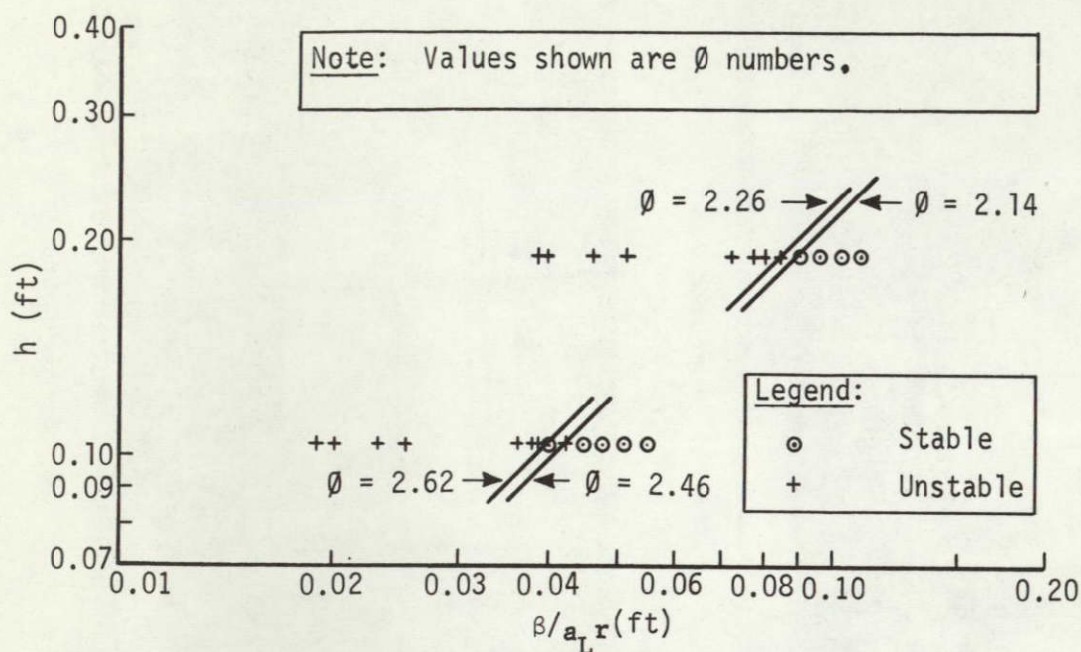


Fig. 61 Stability Characteristics for Straight-Hole Perforated Plates,  $.095 \leq \xi \leq .115$ .

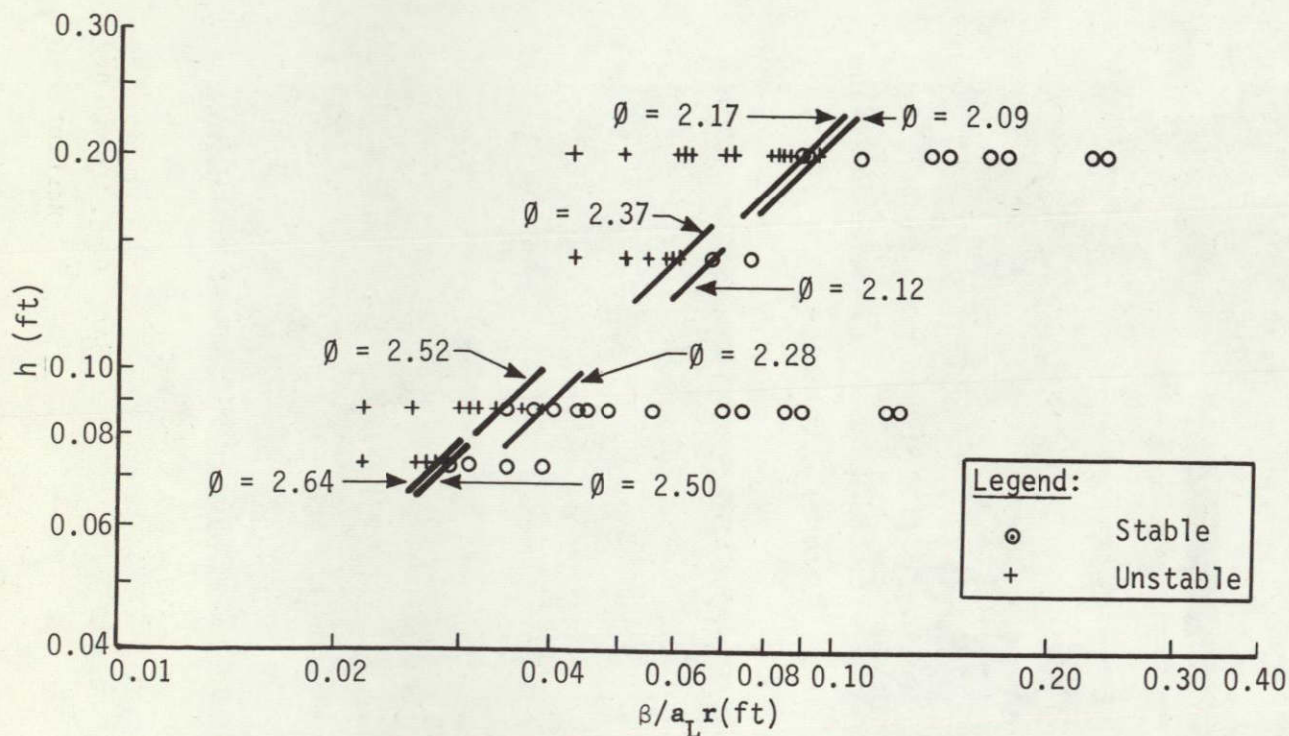


Fig. 62 Stability Characteristics for Straight-Hole Perforated Plates,  $.222 \leq \xi \leq .227$

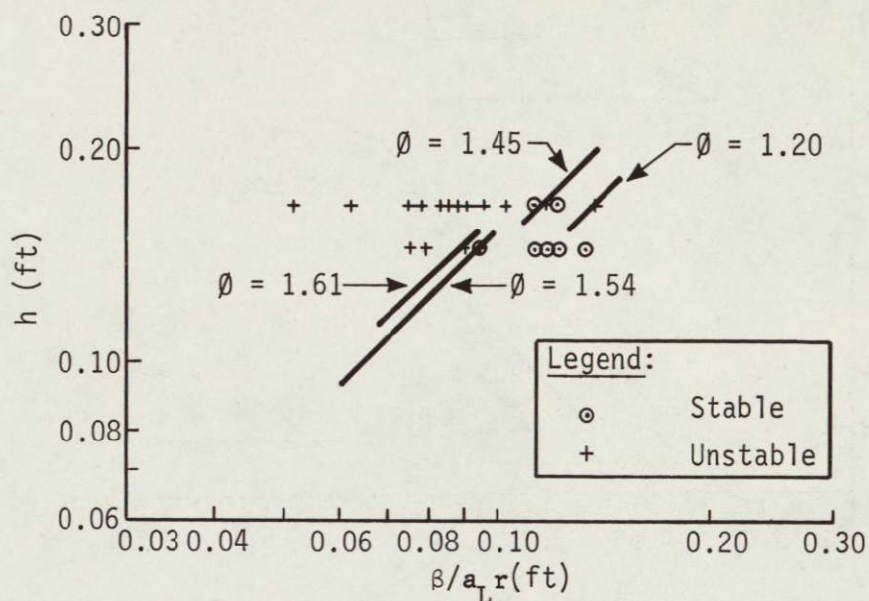


Fig. 63 Stability Characteristics for Cone-Hole Perforated Plates,  $\xi = .362$ .

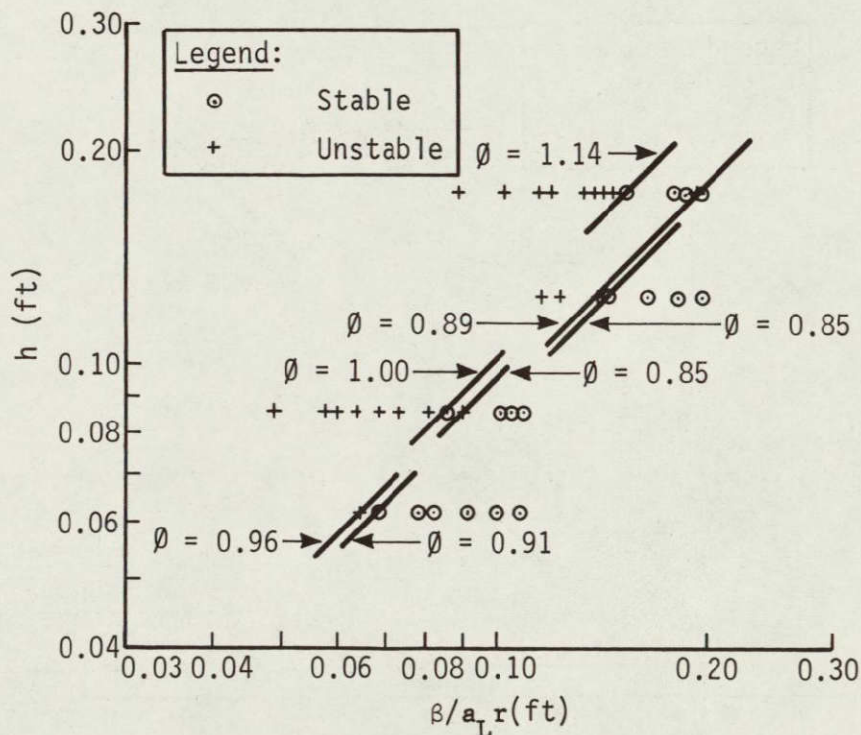
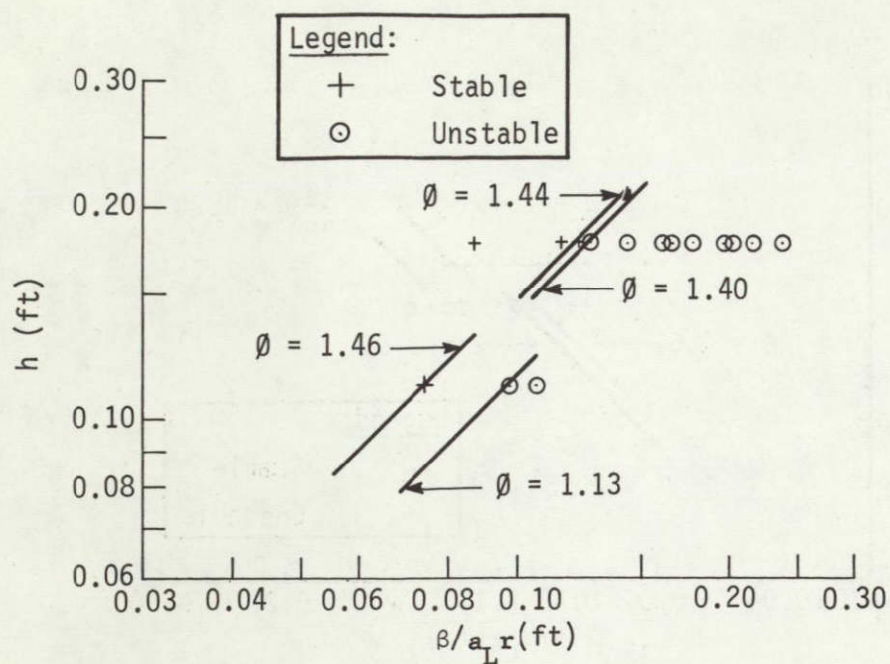
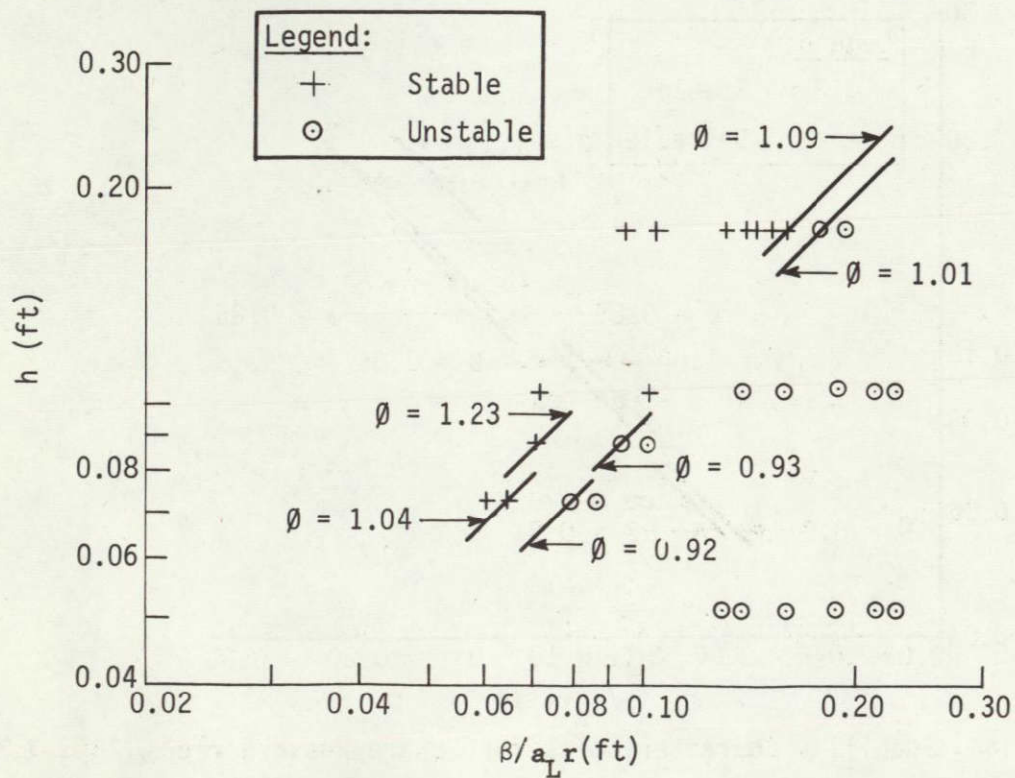


Fig. 64 Stability Characteristics for Square-Weave Screens,  $.28 \leq \xi \leq .35$ .



Fig. 65 Stability Characteristics for 30x250-Mesh Screens ( $\xi = 0$ )Fig. 66 Stability Characteristics for 24x110-Mesh Screens ( $\xi = 0$ )

Figures 61 thru 63 suggest: (1) that the critical  $\emptyset$  number, which delineates stability from instability, tends to be less as  $h$  and  $\beta/a_{Lr}$  increase; and (2) that the critical  $\emptyset$  number decreases as  $\xi$  increases. The dependence of  $\emptyset$  on  $h$  and  $\beta/a_{Lr}$ , however is not as pronounced as its dependence on  $\xi$ . A conservative interpretation (not considering Ga number) of the critical  $\emptyset$  number for perforated plates, based on the data presented in Fig. 61 thru 63, yields  $\emptyset = 2.14$  for  $\xi \leq 11.5\%$ ,  $\emptyset = 2.09$  for  $\xi = 22.7\%$ , and  $\emptyset = 1.20$  for  $\xi = 36.2\%$ . In the same conservative manner, the data for square-weave screens (see Fig. 64) suggest a critical  $\emptyset$  number of 0.85 for  $28.1 \leq \xi \leq 34.8\%$ . The results for twilled cloth (see Fig. 65 and 66) tend to support a critical  $\emptyset$  number of 0.92.

The modified Ga numbers for the test runs are listed in Table 24. These numbers and the corresponding  $\emptyset$  numbers are presented in Fig. 67 thru 74 for perforated plates, square-weave screens, and twilled cloth, respectively. The critical stability lines plotted on each figure correlate fairly well with the two dimensionless parameters.

In Fig. 67, for example, the stability boundary covers a  $\emptyset$  number range from 2.1 to 2.5; the corresponding Ga numbers range from  $1.35 \times 10^5$  to  $9.4 \times 10^5$ . The data are for perforated plates with constant-diameter pores ( $\xi \leq 22.7\%$ ). In Fig. 61 and 62, however, the critical  $\emptyset$  number for the perforated plates ranged from 2.09 to 2.64. This change in the critical  $\emptyset$  number, as illustrated in Fig. 67, is related to the Ga parameter.

For each figure, 67 thru 70, the maximum pore size (diameter) that will provide liquid/gas interface stability can be determined from:

$$d \leq \frac{\frac{m}{2\sigma} \pm \sqrt{\frac{m^2}{4\sigma^2} + \frac{4B}{\mu^2 a_L} h}}{\frac{2\rho}{\mu^2}}, \quad [27]$$

where  $m$  is the slope of the stability boundary line and  $B$  is the intercept on the Ga axis. The pore diameters calculated from Eq [27] are limited to the range of data presented in each figure.

The effect of  $\xi$  on the interface stability of the perforated-plate specimens is shown in Fig. 71. Although the data are rather limited, they show that there was little, or no, effect on stability



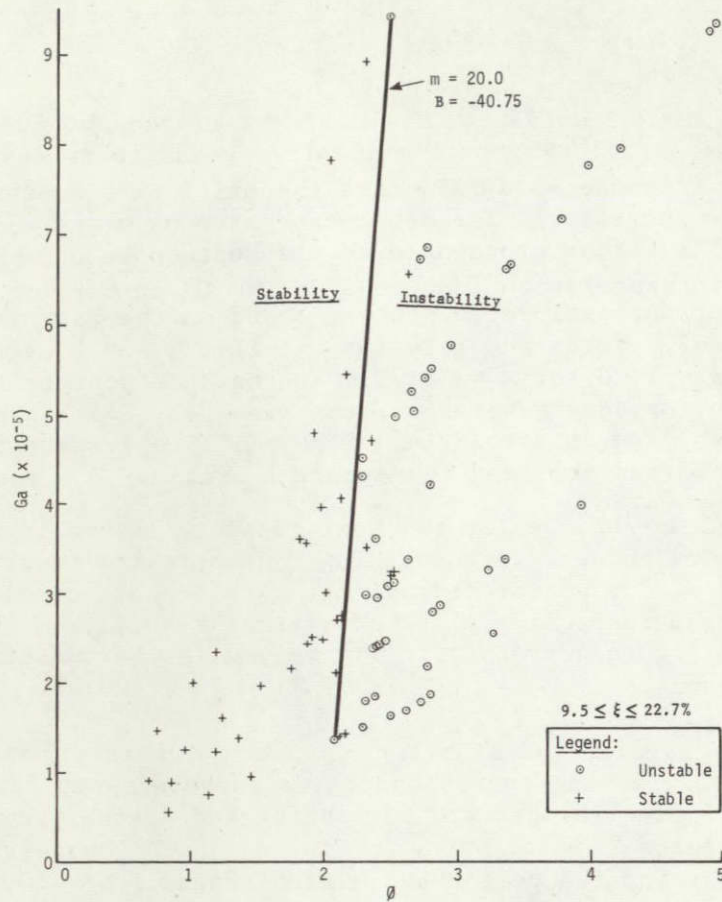


Fig. 67 Stability Characteristics for Straight-Hole Perforated Plates

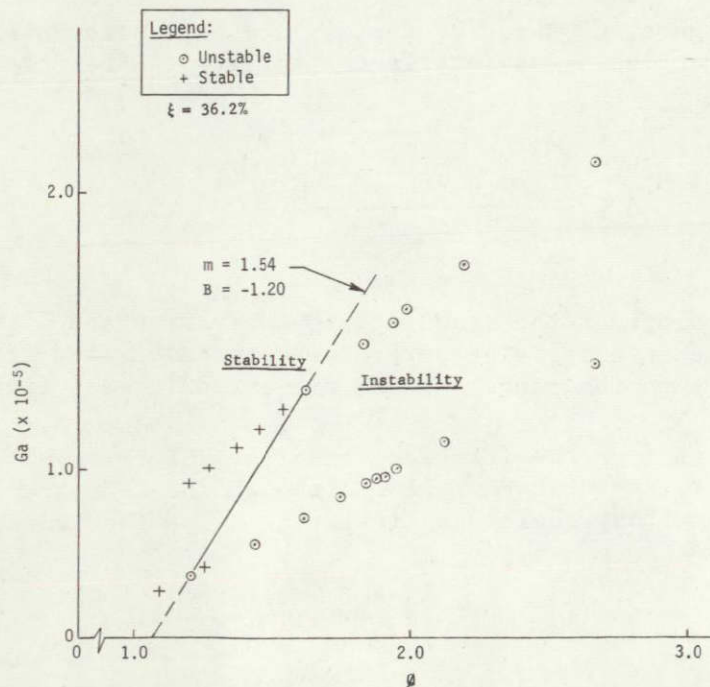


Fig. 68 Stability Characteristics for Cone-Hole Perforated Plates

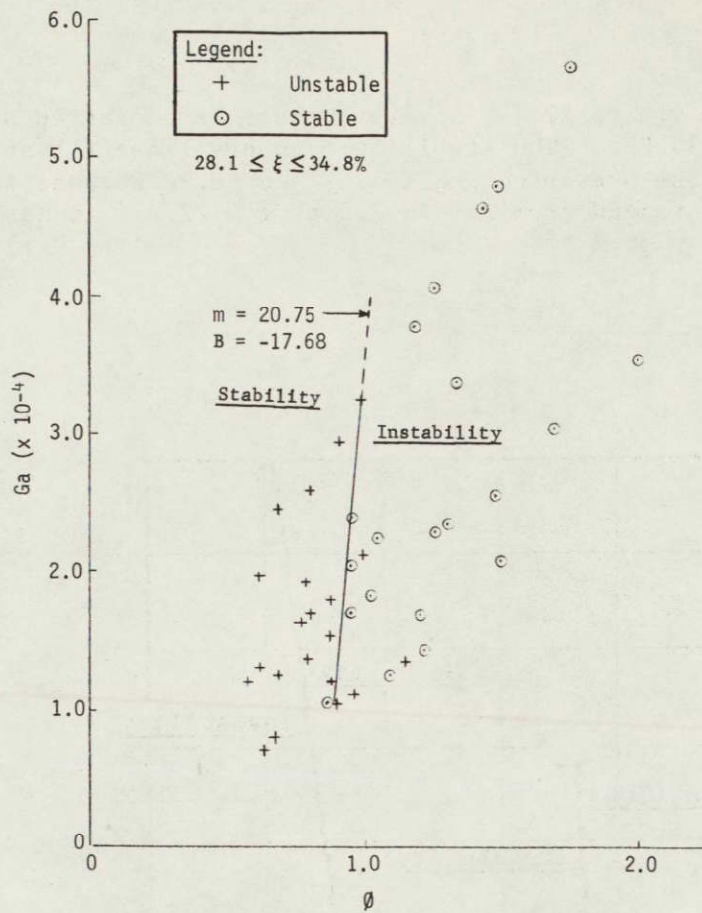


Fig. 69 Stability Characteristics for Square-Weave Screens

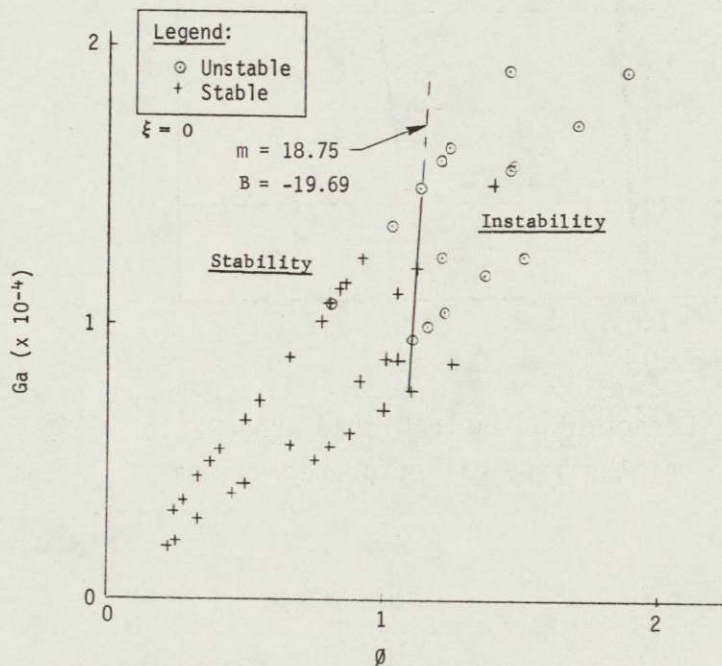


Fig. 70 Stability Characteristics for Dutch-Twill Screens



for  $\xi$  values from 9.5 to 22.7%; however, there is a drastic stability reduction at  $\xi = 36.2\%$ . (The stability boundary lines illustrated in Fig. 71 are those presented in Fig. 67 and 68.) Whereas the critical  $\phi$  number ranged from 2.1 to 2.5 at  $\xi \leq 22.7\%$ , it has a value of 1.1 at  $\xi = 36.2\%$ .

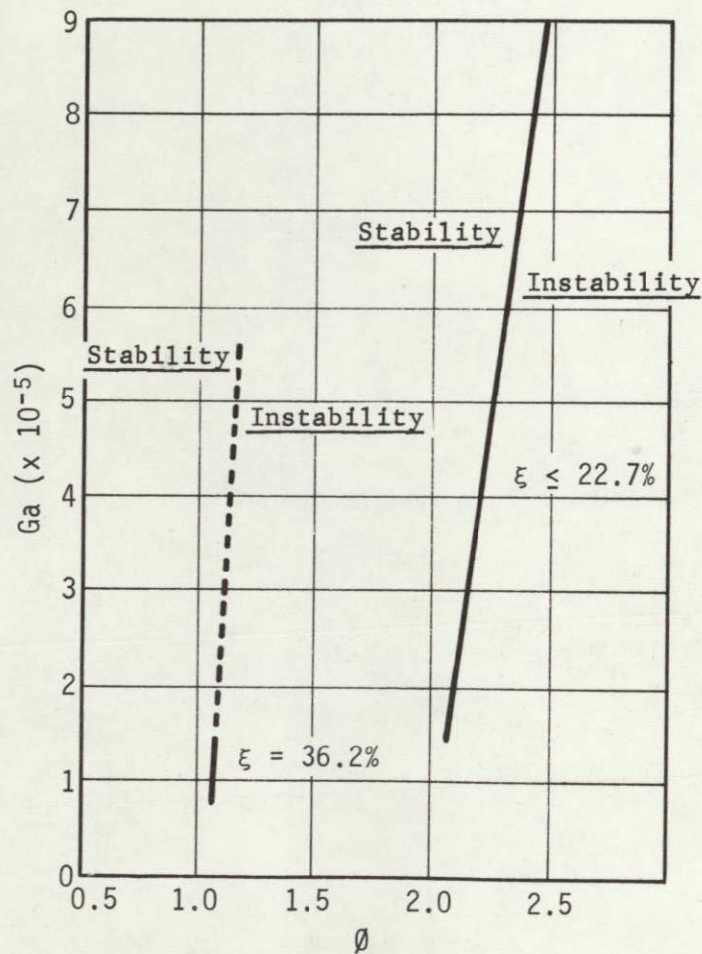


Fig. 71 Effect of Open-to-Closed Area Ratio on Stability of Perforated Plates

The lowered stability with increased  $\xi$  may be explained by referring to Fig. 72. As mentioned previously, the tests were conducted with liquid  $\frac{1}{4}$  in. or less above the perforated barriers to ensure that the barrier would be wetted before the capsule was dropped. Upon initiation of the lateral acceleration, the liquid above the barrier moved toward one side of the box-like test specimen. The flow path for this lateral migration tended to be above the surface of the barrier; however, depending on the open area of the barrier, some liquid flowed through the pores.

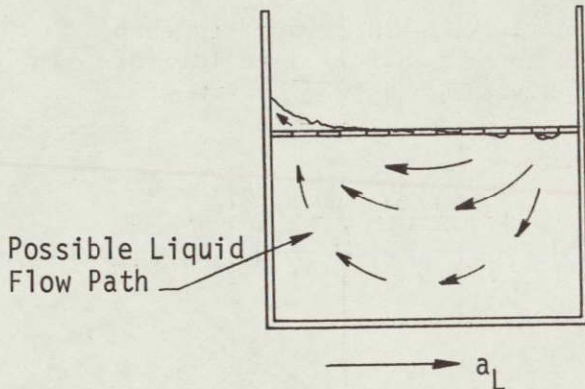


Fig. 72 Possible Sideways Liquid Motion

The momentum of this liquid must be dissipated by viscous shear and by the capillary differential pressure force at the pores. As the open-to-closed surface area increases, the amount of liquid passing through the barriers tends to increase, thereby reducing the interface stability.

In summary, liquid/gas interface stability under a lateral acceleration may be determined either by considering both the modified Ga number (see Fig. 61 thru 66), or by considering both the modified Ga number and the  $\emptyset$  number (see Fig. 67 thru 71). The latter procedure is recommended, even though the

interface stability for the test data presented in this report is a relatively weak function of the modified Ga number.

An analysis similar to that outlined in previous chapters was performed to estimate the accuracy of the test results. With regard to the accuracy of the  $\emptyset$  number:

$$w_{\emptyset} = \left[ \left( \frac{\partial \emptyset}{\partial a_L} w_{a_L} \right)^2 + \left( \frac{\partial \emptyset}{\partial r} w_r \right)^2 + \left( \frac{\partial \emptyset}{\partial h} w_h \right)^2 + \left( \frac{\partial \emptyset}{\partial \beta} w_{\beta} \right)^2 \right]^{1/2}, \quad [28]$$

where  $w$  is the uncertainty interval (plus or minus) associated with the  $\emptyset$  number and the variables in the  $\emptyset$  number relationship.



The lateral acceleration was calculated as

$$a_L = 2(\Delta x) \left( \frac{fs}{\Delta f} \right)^2, \quad [29]$$

where  $\Delta x$  is the lateral distance,  $fs$  is the camera's film speed, and  $\Delta f$  is the frame count over the lateral distance.

By substituting Eq [29] into Eq [25], we obtain:

$$\phi = \frac{2(\Delta x)hr}{\beta} \left( \frac{fs}{\Delta f} \right)^2. \quad [30]$$

This equation can be partially differentiated with respect to each of the variables and combined with the non-dimensionalized form of the uncertainty equation (obtained by dividing Eq [28] by the  $\phi$  number) to yield:

$$\frac{w_\phi}{\phi} = \left[ \left( \frac{w_{\Delta x}}{\Delta x} \right)^2 + \left( \frac{w_r}{r} \right)^2 + \left( \frac{w_h}{h} \right)^2 + \left( \frac{2w_{fs}}{fs} \right)^2 + \left( \frac{w_\beta}{\beta} \right)^2 + \left( \frac{2w_{\Delta f}}{\Delta f} \right)^2 \right]^{1/2}. \quad [31]$$

Similarly, for the Ga number:

$$\frac{w_{Ga}}{Ga} = \left[ \left( \frac{w_{\Delta x}}{\Delta x} \right)^2 + \left( \frac{2w_d}{d} \right)^2 + \left( \frac{w_h}{h} \right)^2 + \left( \frac{2w_{fs}}{fs} \right)^2 + \left( \frac{2w_v}{v} \right)^2 + \left( \frac{2w_{\Delta f}}{\Delta f} \right)^2 \right]^{1/2} \quad [32]$$

Equations [31] and [32] are valid only when the uncertainty for each variable is based on the same odds (in other words, the best value for each variable is the average value). The odds are 20:1 that the true value of each variable lies within the uncertainties given in Table 25. The estimated uncertainty values for the variables determined in the lateral stability tests are presented in Table 26.

The uncertainty values thus determined for all runs except those using the 100x100-mesh screen are between  $\pm 5.05$  and  $\pm 7.75\%$ . The higher uncertainty values for the  $\phi$  number ( $\pm 10.70\%$ ) and the Ga number ( $\pm 13.0\%$ ) calculated from tests made using the 100x100-mesh screen are mainly due to a greater variation in the screen pore opening.

Table 25 Uncertainty Intervals for Sample Variables Used to Calculate  $\emptyset$  and Ga

VARIABLE	SYMBOL	AVERAGE VALUE	UNCERTAINTY
Distance	$\Delta x$	0.18 ft	$\pm 0.0013$ ft
Pore Radius (1/32-in.-diameter plate)	r	0.0164 in.	$\pm 0.00045$ in.
Height	h	0.2 ft	$\pm 0.0013$ ft
Camera Film Speed	fs	198 frames/sec	$\pm 2$ frames/sec
Kinematic Surface Tension, Methanol	$\beta$	$10.1 \times 10^{-4}$ ft <sup>3</sup> /sec <sup>2</sup>	$\pm 0.55 \times 10^{-4}$ ft <sup>3</sup> /sec <sup>2</sup> *
Kinematic Viscosity, Methanol	$\nu$	$9.17 \times 10^{-6}$ ft <sup>2</sup> /sec	$\pm 0.50 \times 10^{-6}$ ft <sup>2</sup> /sec
Lateral Travel Frame Count	$\Delta f$	125 frames	$\pm 2$ frames
*Table IV, Ref 7.			

Table 26 Per Cent Uncertainty for Lateral Stability Tests Made with Lateral Travel Mechanism Shown in Fig. 58

NO.	TEST LIQUID	RUN NO.	PER CENT UNCERTAINTY ( $\pm$ ) FOR BARRIER NO.								
			1	2	3	4	5	6	7	8	9
$\emptyset$	Methanol	$\leq 202$	6.60	6.75				10.25	7.00	5.90	6.40
		$> 202$	6.60	6.80	6.1	6.0	6.3	10.25	7.10		6.50
Ga	Methanol	$\leq 202$	6.5	6.7				12.9	7.3	5.1	6.25
		$> 202$	6.5	6.75	5.4	5.35	4.95	13.0	7.35		6.35
$\emptyset$	Freon	$\leq 202$	7.25	7.40				10.65	7.6	6.55	7.15
		$> 202$	7.25	7.45	6.9	6.8	6.95	10.70	7.75		7.15
Ga	Freon	$\leq 202$	6.4	6.6				12.9	7.3	5.05	6.2
		$> 202$	6.4	6.65	5.3	5.25	4.9	13.0	7.35		6.30
$\emptyset$	Carbon Tetra-chloride	All Runs	6.1	6.25				9.9	6.5	5.3	5.85
Ga	Carbon Tetra-chloride	All Runs	6.2	6.4				12.8	7.1	4.8	6.0



## VI. FILLING OF CAPILLARY DEVICES

### A. OBJECTIVES

The drop tower tests described in Chapters III, IV, and V dealt with establishing criteria for the selection of foraminous materials and the design of capillary devices to provide proper liquid positioning and control. As discussed in Chapter I, single-phase fluid (liquid) may be drained from a storage tank during low-g accelerations provided that: (1) the annulus of the capillary system contains only liquid; and (2) the liquid reservoir is in contact with the annulus. When these two conditions are satisfied, liquid will drain from the reservoir into the annulus, and out of the tank.

The probability that the annulus within a small propellant-acquisition device will lose its liquid priming until propellant becomes depleted is low since the trap is usually totally immersed during high-g (boost) accelerations.

For other capillary configurations, in which the annulus is relatively long (such as a complete concentric liner), the probability is high, and liquid may be lost from the annulus before launch, during launch, and after launch. During a ground hold (at 1 g) and launch (at 6 to 8 g), the hydrostatic heads may exceed the pressure-retention ability of the foraminous material, as discussed in previous chapters. This may also happen during attitude control maneuvers, engine burns, and coasting periods. During the latter, vehicle drag can cause liquid loss from annuli.

The objective of the work described in this chapter was to evaluate the ability of annuli to be refilled, if required, utilizing surface-tension forces and to examine the impact on capillary-system designs. Flow induced by surface-tension forces (capillary pumping) has been studied by a number of investigators (Ref 13 and, 28 to 32), but the filling of annuli in propellant orientation and control devices has not been adequately examined.



## B. EXPERIMENTAL APPARATUS AND TEST PROCEDURE

Three test specimens were used. The first was a sealed glass cylinder that had an I.D. of  $3 \frac{7}{16}$  in. and a length of  $2 \frac{5}{16}$  in. A 100x100-mesh,  $3 \frac{3}{16}$  in. O.D. cylindrical screen was placed inside the cylinder. There was a 0.125 in. (nominal) annulus gap between the screen and cylinder. This cylinder was mounted on its side on the test platform of the inner capsule. One end of the cylinder faced the camera. Mirrors positioned at the side and top of the specimen showed two additional views of the annulus (see Fig. 73). The annulus was filled in the azimuthal direction, as shown. This test setup was used since it shows the interaction between the reorientation of the bulk liquid and the liquid flow into the annulus.

The second glass specimen was also a cylinder with an I.D. of  $4 \frac{7}{8}$  in. and a length of  $4 \frac{1}{4}$  in. It had a 200x1400-mesh Dutch-twill screen liner with an annulus gap of 0.125 in. (nominal).

The third test specimen was an  $8 \frac{15}{32}$  in. I.D. glass sphere containing a 40x40-mesh spherical screen liner. The spherical annulus gap was a nominal 0.11 in.

Methanol was the test fluid for the cylinders. Chloroform<sup>\*</sup> was used in the sphere.

The general test plan was to determine under what conditions (low-g level, screen weave and mesh, and liquid volume) the annuli would fill and to determine the time required.

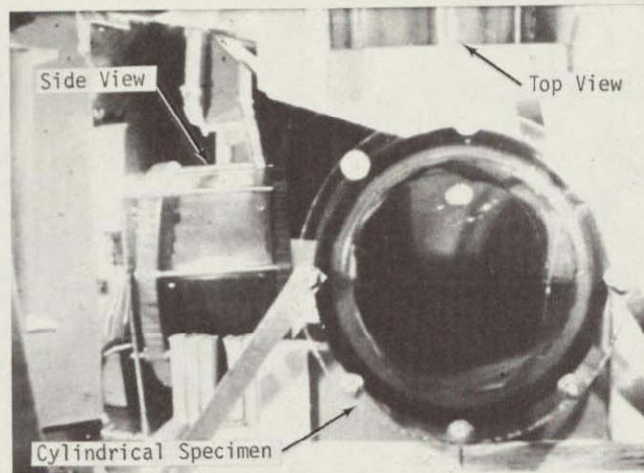
The primary reason for incomplete filling of the annulus was assumed to be that the screen pores would fill with liquid before the annulus was filled. This could result for at least three reasons: (1) wicking in the capillary passages of the screen material; (2) sloshing or splashing of the liquid on the screen; and (3) reorientation of the bulk liquid.

---

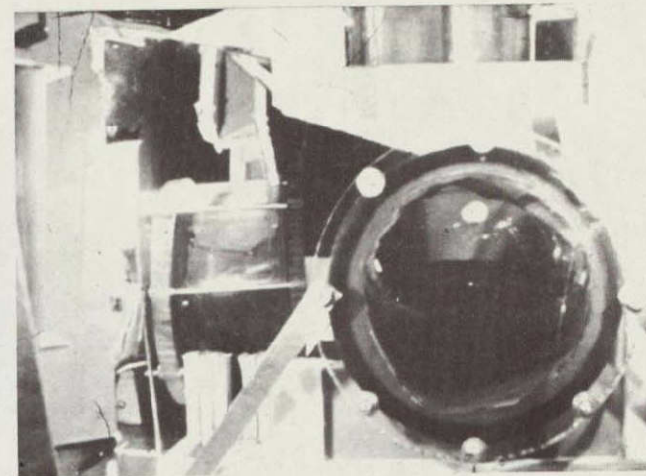
\*Chloroform has the following physical properties (20°C):

$\sigma = 1.85 \times 10^{-3}$  lb<sub>f</sub>/ft;  $\rho = 93.0$  lb<sub>m</sub>/cu. ft; and  $\mu = 3.89 \times 10^{-4}$  lb<sub>m</sub>/ft-sec. The kinematic surface tension is  $6.41 \times 10^{-4}$  ft<sup>3</sup>/sec<sup>2</sup>.

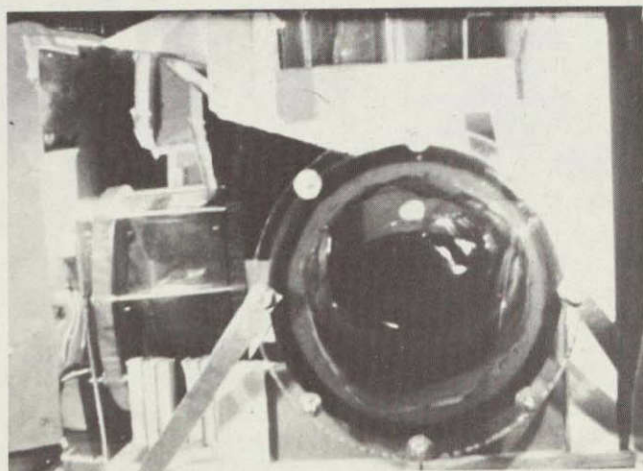




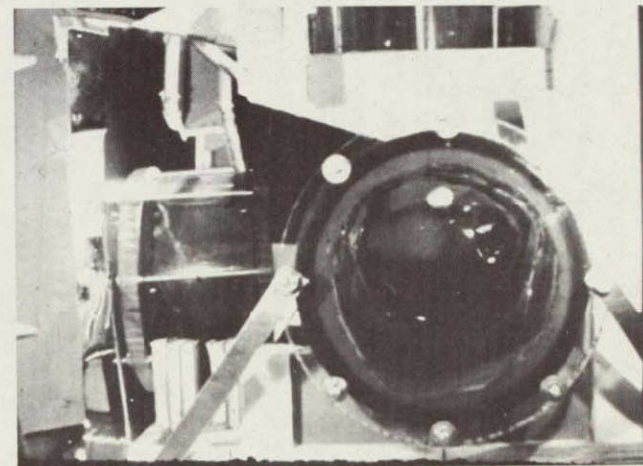
(a)  $t = 0 \text{ sec}$



(b)  $\Delta t = 0.34 \text{ sec}$



(c)  $\Delta t = 0.67 \text{ sec}$



(d)  $\Delta t = 1.03 \text{ sec}$

Fig. 73 Annulus Being Filled in Run 4 (Three View are Shown;  
Top View Best Shows Complete Filling).

Twilled cloth and square-weave screens were tested to evaluate the effect of the weave on wicking. Wetting by sloshing was examined by comparing the fill results for the 100x100-mesh specimen from two different sets of tests. In the first set, considerable care was taken to prevent the liquid from splashing on the screen before the capsule was dropped; in the second set of tests, the filled specimen was inverted and rotated to ensure that the liquid had contacted the screen before the capsule was dropped. Screen wetting due to bulk reorientation of the liquid was evaluated by using different initial liquid levels. Also, in several tests, liquid ( $0.35 \text{ lb}_m/\text{sec}$ ) was expelled from the spherical container 0.9 sec after the capsule was released to evaluate the effect of expulsion on the filling of the annulus. All the tests were made with a sudden transition from 1 g to either a zero-g or a low negative axial-g condition.

### C. EXPERIMENTAL RESULTS

Twenty-one drop tests were made. Table 27 and Fig. 74 summarize the test results, and show the time required to completely fill the annulus ( $t_{\text{fill}}$ ). Figures 73, 75, and 76 are photographic sequences taken during the drop tests.

Figure 73 shows that the annulus filled completely. Figure 75 shows that the liquid in the central reservoir wetted the screen and prevented the annulus from being filled. Figure 76 shows that the annulus formed by the 200x1400-mesh Dutch-twill screen was not filled during the zero-g test.

We found that the annulus never filled when the test specimen contained a Dutch-twill screen liner (200x1400 mesh), but did for a square-weave liner when  $V_L/V_C \leq 0.47$ . We concluded that the Dutch-twill screen wicked faster than the annulus filled, and that the liquid sealed the screen so that vapor could not flow out of the annulus. On the other hand, the square-weave screen barrier did not wick; but at high fill levels, the bulk liquid was re-oriented and wetted the screen before the annulus could fill, thereby closing the annulus and preventing vapor from escaping.



Table 27 Summary of Data on Annulus Filling

RUN	TEST SPECIMEN*	LIQUID	ACCELERATION (g)	SCREEN MESH	FULL OF LIQUID (%)	ANNULUS FILLED	TIME REQUIRED TO FILL ANNULUS (sec)
1	1	Methanol	0	100	22.3	Yes	1.34
2	1	Methanol	-0.0036	100	22.3	Yes	1.30
3	1	Methanol	-0.0180	100	22.3	Yes	1.05
4	1	Methanol	0	100	45.4	Yes	1.04 <sup>†</sup>
5	1	Methanol	-0.0030	100	45.4	Yes	0.97 <sup>†</sup>
6	1	Methanol	-0.0147	100	45.4	Yes	0.845 <sup>†</sup>
7	1	Methanol	0	100	45.4	Yes	1.07 <sup>§</sup>
8	1	Methanol	-0.0030	100	45.4	Yes	1.00 <sup>§</sup>
9	1	Methanol	-0.0147	100	45.4	Yes	0.845 <sup>§</sup>
10	1	Methanol	0	100	28.3	Yes	1.42
11	1	Methanol	0	100	70.9	No	
12	1	Methanol	0	100	89.4	No	
13	2	Methanol	0	200x1400	25.0	No	
14	2	Methanol	0	200x1400	50.0	No	
15	2	Methanol	0	200x1400	75.0	No	
16	3	Chloroform	0	40	17.0	Yes	1.44 <sup>¶</sup>
17	3	Chloroform	0	40	25.0	Yes	1.22 <sup>¶</sup>
18	3	Chloroform	0	40	47.0	Yes	0.875
19	3	Chloroform	-0.0216	40	17.0	Yes	1.40 <sup>¶</sup>
20	3	Chloroform	-0.0216	40	25.0	Yes	1.105 <sup>¶</sup>
21	3	Chloroform	-0.0216	40	47.0	Yes	0.735

\*Test specimen designations: 1 = Horizontal Cylinder  
Diameter = 3.44 in.  
Annulus Gap = 0.125 in.  
Length = 2.31 in.  
2 = Horizontal Cylinder  
Diameter = 4.875 in.  
Annulus Gap = 0.125 in.  
Length = 4.25 in.  
3 = Sphere  
Diameter = 8.46 in.  
Annulus Gap = 0.11 in.

<sup>†</sup>Experimental package handled with considerable care to avoid sloshing liquid on the screen.

<sup>§</sup>Experimental package handled so that liquid contacted the entire screen before the drop.

<sup>¶</sup>Liquid expulsion (0.35 lb<sub>m</sub>/sec) initiated after 0.9 sec of drop time.

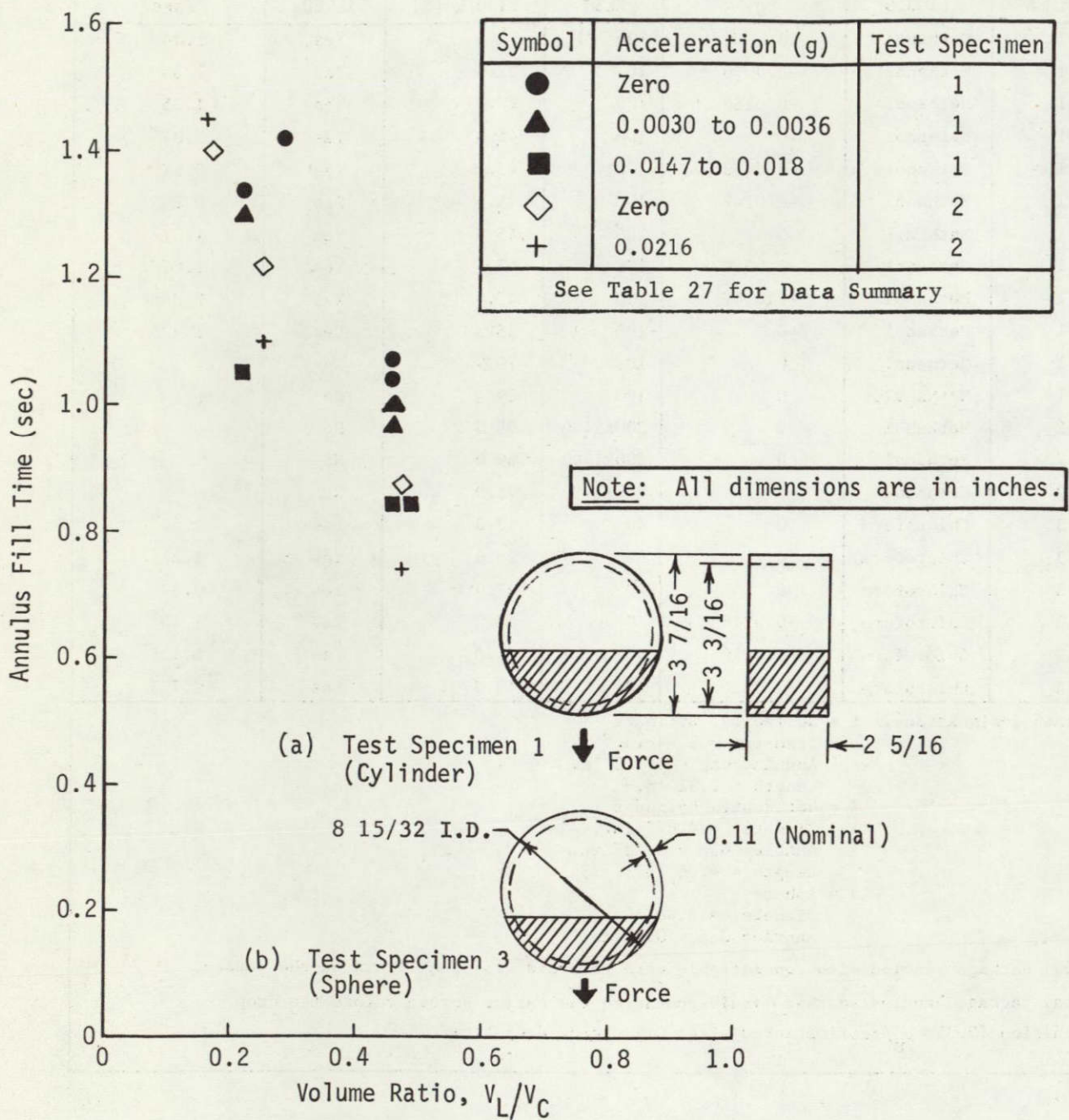
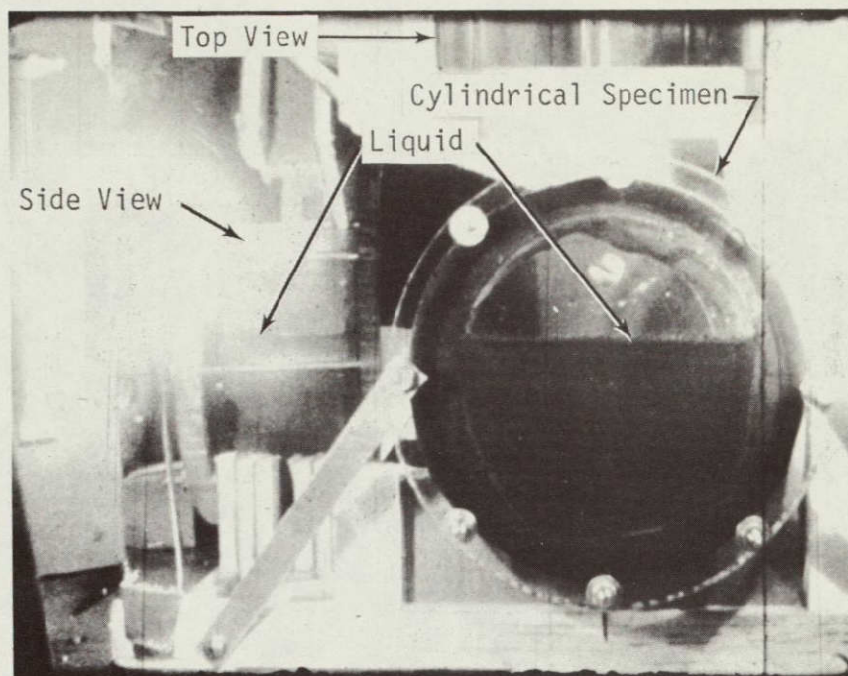
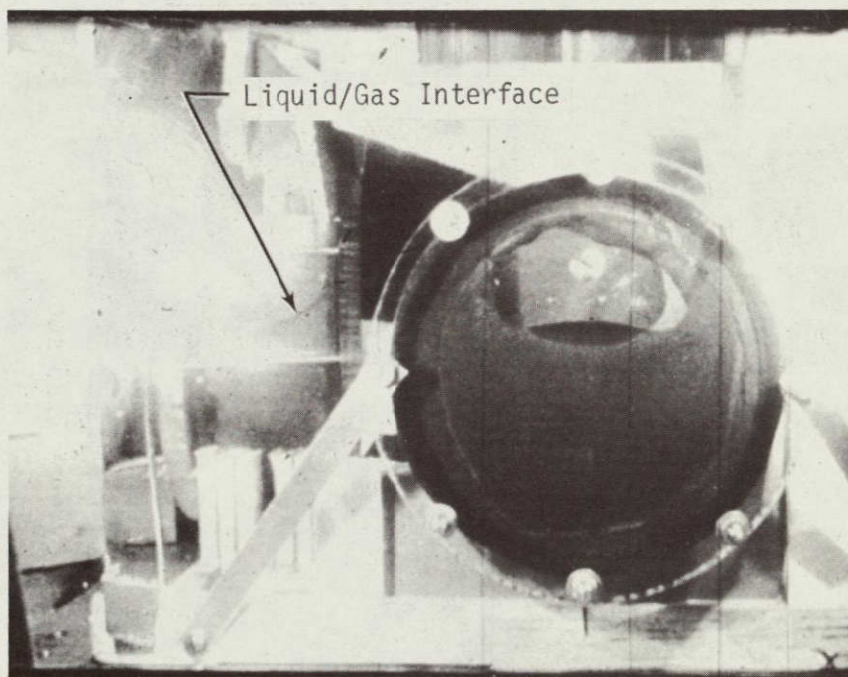


Fig. 74 Annulus Fill Time vs Liquid-to-Container Volume Ratio





(a) At Initiation of Zero-g Test ( $\Delta t = 0$  sec)



(b)  $\Delta t = 0.50$  sec

Fig. 75 Annulus Fill Test, Run 11  
(Three Views Shown; Side View  
Shows Incomplete Filling).

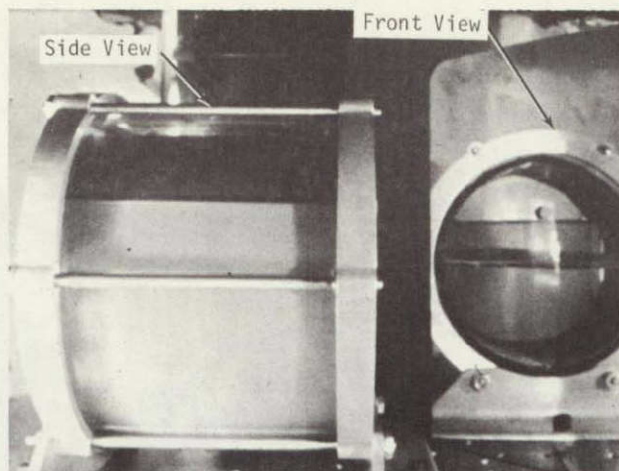
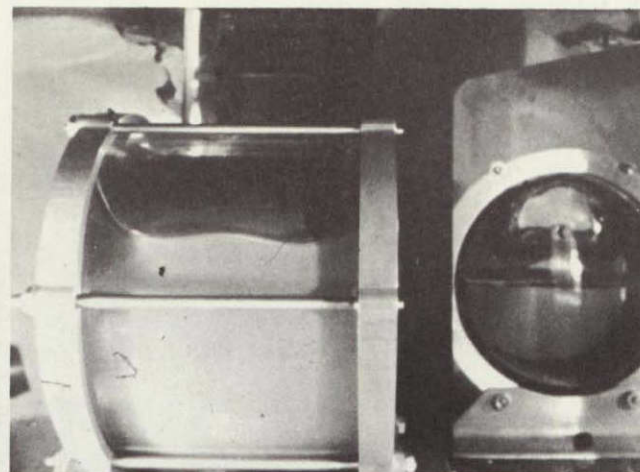
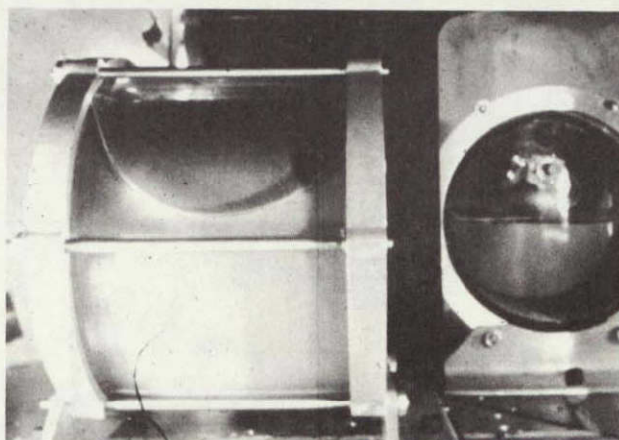
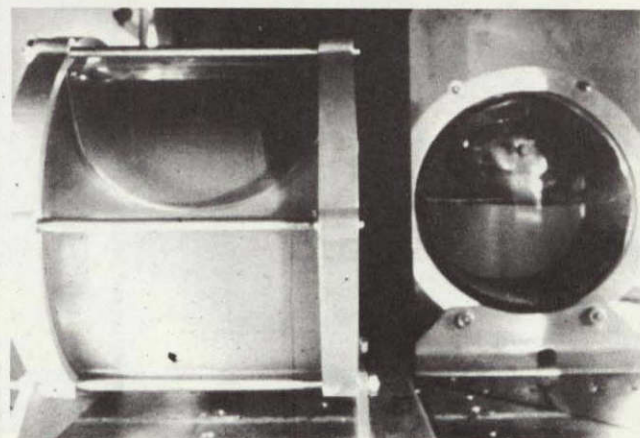
(a)  $t = 0$  sec(b)  $\Delta t = 0.63$  sec(c)  $\Delta t = 1.25$  sec(d)  $\Delta t = 1.88$  sec

Fig. 76 Annulus Fill Test, Run 19 (Two Views are Shown ... the front view is provided by a reflector; the liquid/gas interface in the annulus is clearly evident in the side view).



Paynter's energy correlation of the free-surface distortion time (Ref 32) shows that the time it takes to wet the screen,  $t_{\text{wet}}$ , is proportional to a characteristic time  $t'$ :

$$t_{\text{wet}} = K t' = \frac{K}{\left(\frac{\sigma}{\rho R^3}\right)^{1/2}}, \quad [33]$$

where  $K$ , an empirical factor, is a function of the liquid-to-container volume ratio ( $V_R$ ).

As seen from Runs 4 thru 9 (Table 27), liquid sloshing on the square-weave screen before the capsule was dropped did not affect the time it took the annulus to fill. Clearly, the square-weave screen did not remain wetted before the capsule was released.

The liquid outflow that occurred during Runs 16, 17, 19 and 20 with the spherical specimen slowed the rate at which the annulus filled, as indicated by Fig. 77. However, there was no tendency for the gas in the annulus to be drawn out of the container. Rather, the annulus continued to fill while the bulk liquid flowed through the screen, into the annulus, and out of the container.

The following analysis of the fluid dynamics of the filling process shows that the fill time is a function of the following nondimensional parameters:

$$\frac{t_{\text{fill}}}{t'} = f(\alpha, Bo, S, V_R), \quad [34]$$

where:

$$t' = \left(\frac{\sigma}{\rho R^3}\right)^{-1/2} \quad [35]$$

$$\alpha = \frac{\ell}{R}; \quad [36]$$

$$Bo = \frac{\rho a R^2}{\sigma}; \quad [37]$$

$$S = \left(\frac{\rho v^2}{\sigma R}\right)^{1/2}; \quad [38]$$

$$V_R = \frac{V_L}{V_C}. \quad [39]$$

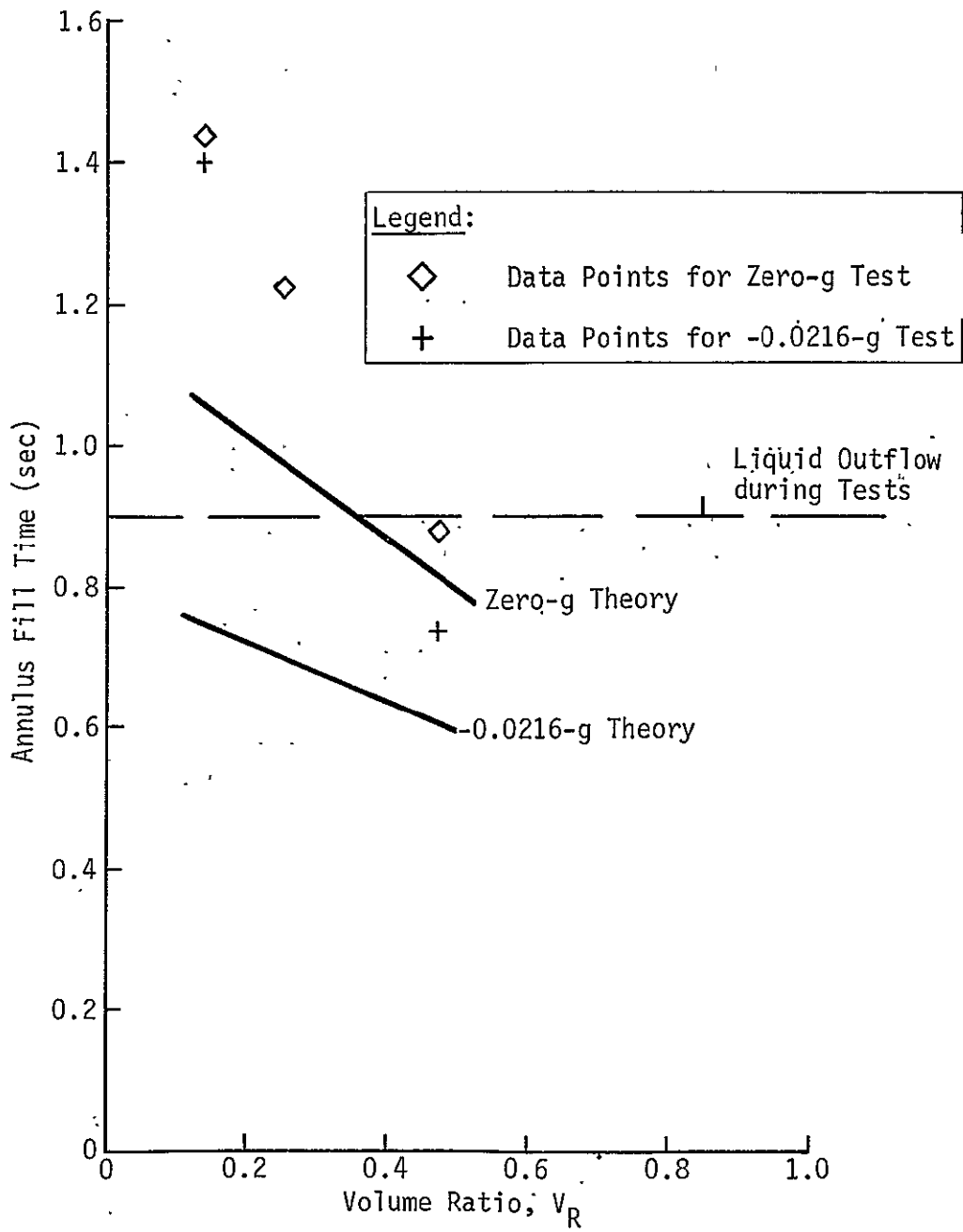


Fig. 77 Comparison of Predicted and Recorded Fill Times for a Spherical Annulus



The time required to fill a cylindrical annulus (see Table 27 and Fig. 74) are roughly correlated by

$$\frac{t_{fill}}{t'} = \frac{1.6 - 1.3 \frac{V_R}{Bo}}{1 + 0.0043 \frac{V_R}{Bo}} \quad [40]$$

for

$$\alpha = 0.267$$

$$S = 4.3 \times 10^{-4}.$$

The parameters  $\alpha$  and  $S$  were not varied during these tests.

The limiting fill condition is that at which the fill time is just matched by the time required for the bulk liquid to wet and seal the screen,

$$t_{wet} = t_{fill}. \quad [41]$$

The data show that this relation is satisfied by a value of  $V_R$  somewhere between 0.454 and 0.709 for the cylindrical test specimen.

An exact analysis of the fluid dynamics of annulus filling does not appear to be possible because of the complexity of the bulk liquid flow and its interaction with the annular flow; however, an order-of-magnitude study was made and is presented here. Let us consider the dynamics associated with annulus filling in a spherical container and compare our calculations to the test results.

The fluid dynamics of the incompressible liquid can be derived from two equations: the equation of mass continuity

$$\nabla \cdot \underline{v} = 0; \quad [42]$$

and the equation for the conservation of momentum

$$\frac{\partial \underline{v}}{\partial t} + (\underline{v} \cdot \nabla) \underline{v} + \frac{\nabla p}{\rho} = \underline{a} + \text{viscous term}. \quad [43]$$

We assume one-dimensional flow in the spherical annulus and account for viscous effects via a friction-factor approach. The viscous term is assumed to be

$$\text{Viscous term} = -\frac{4f}{D} \cdot \frac{\rho v^2}{2}, \quad [44]$$

where the hydraulic diameter,  $D$ , is four times the flow area divided by the wetted perimeter. Since the flow area in the spherical annulus is the lateral area of the frustum of a cone (half the slant height times the perimeter), the hydraulic diameter is:

$$D = 2\ell. \quad [45]$$

The friction factor is assumed to be inversely proportional to the Reynolds number:

$$4f = \frac{K}{\text{Re}} = \frac{Kv}{v\ell}. \quad [46]$$

Since there is no exact solution to act as a guide to the proper value for  $K$  as there is with flow inside a tube (where  $K = 64$ ), we make the assumption of one-dimensional flow in the spherical annulus (see Fig. 78). This is expressed by

$$v \sim \widehat{v i}_\theta, \text{ where } \chi(t) \leq \theta \leq \tau(t). \quad [47]$$

The mean height of the bulk liquid interacts with the annulus at  $\theta = \chi(t)$ . The liquid/vapor interface inside the annulus is at  $\theta = \tau(t)$ .

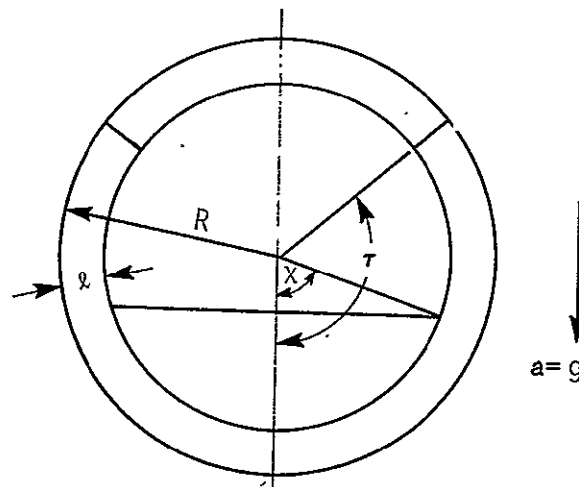


Fig. 78 Schematic Representation of Annulus Filling



The continuity equation, Eq [42], can be expressed in spherical coordinates as

$$\frac{\partial}{\partial \theta} (v \sin \theta) = 0, \quad [48]$$

or as

$$v(\theta, t) \sin \theta = v[\tau(t), t] \sin \tau(t). \quad [49]$$

The momentum equation becomes:

$$\frac{\partial v}{\partial t} + \frac{v}{R} \left( \frac{\partial v}{\partial \theta} \right) + \frac{1}{\rho R} \left( \frac{\partial p}{\partial \theta} \right) = -a \sin \theta - \frac{Kv}{4\ell^2} v. \quad [50]$$

Now, using the continuity result, Eq [49], the momentum equation, Eq [50], can be solved for pressure as:

$$\frac{\partial p}{\partial \theta} = -\rho R \left\{ \frac{\frac{\partial}{\partial t} [v(\tau, t) \sin \tau]}{\sin \theta} - \frac{v^2(\tau, t) \sin^2 \tau \cos \tau}{R \sin^3 \theta} + \frac{\frac{Kv}{4\ell^2} v(\tau, t) \sin \tau}{\sin \theta} - a \sin \theta \right\}, \quad [51]$$

which integrates to

$$p(R, \tau, t) - p(R, \chi, t) = -\rho R \left( \left\{ \frac{\partial}{\partial t} [v(\tau, t) \sin \tau] + \frac{Kv}{4\ell^2} v(\tau, t) \sin \tau \right\} \ln \left( \frac{\tan \frac{\chi}{2}}{\tan \frac{\tau}{2}} \right) + \frac{v^2(\tau, t)}{2R} \left( \frac{\sin^2 \tau}{\sin^2 \chi} - 1 \right) + a(\cos \chi - \cos \tau) \right). \quad [52]$$

The liquid pressure is related to the ullage pressure by the surface-tension expression

$$p(R, \tau, t) = p_{\text{ullage}} - \sigma \left( \frac{1}{R_1} + \frac{1}{R_2} \right), \quad [53]$$

where  $R_1$  and  $R_2$  are the principal radii of curvature. In approximation:

$$R_1 \approx \frac{\ell}{2}; \quad [54]$$

$$R_2 \approx -R \tan \tau. \quad [55]$$

Now, by assuming that the liquid pressure at  $\theta = \chi$  is approximately equal to the ullage pressure -- i.e., that

$$p(R, \chi, t) \approx p_{\text{ullage}}, \quad [56]$$

we do not need to consider the fluid dynamics inside the spherical screen nor the interaction with flow in the annulus. Thus, the pressure difference is simply

$$p(R, \chi, t) - p(R, \tau, t) \approx \sigma \left( \frac{2}{\ell} - \frac{1}{R \tan \tau} \right); \quad [57]$$

and the assumption of one-dimensional flow allows us to relate velocity and the position of the annulus interface by the kinematic condition

$$v(\tau, t) = R \frac{d\tau}{dt}. \quad [58]$$

Consequently, Eq [52] can be written:

$$\begin{aligned} \frac{d^2\tau}{dt^2} + \left( \frac{d\tau}{dt} \right)^2 \cot \tau + \frac{Kv}{4\ell^2} \left( \frac{d\tau}{dt} \right) = \\ = \frac{\frac{a}{R} (\cos \tau - \sin \tau) + \frac{\sigma}{\rho R^3} \left( \frac{2R}{\ell} - \cot \tau \right) + \frac{1}{2} \left( \frac{\sin^2 \tau}{\sin^2 \chi} - 1 \right) \left( \frac{d\tau}{dt} \right)^2}{\sin \tau \ln \left( \frac{\tan \frac{\tau}{2}}{\tan \frac{\chi}{2}} \right)}, \end{aligned} \quad [59]$$

where the angles  $\tau$  and  $\chi$  are interrelated by mass continuity.

The volume of bulk liquid (inside the screen) is

$$V_\ell = \frac{\pi}{3} (R - \ell)^3 [2 - \cos \chi (3 - \cos^2 \chi)], \quad [60]$$

and the volume in the annulus is

$$V_A = \frac{2\pi}{3} R^3 \left[ 1 - \left( 1 - \frac{\ell}{R} \right)^3 \right] (1 - \cos \tau). \quad [61]$$



Mass continuity requires that:

$$V_A + V_\ell = \text{constant} = \left( V_A + V_\ell \right) \Big|_{t=0}; \quad [62]$$

and since the ratio of liquid volume-to-container volume can be written

$$V_R = \frac{V_A + V_\ell}{\frac{4\pi R^3}{3}}, \quad [63]$$

Eq [62] can be written as:

$$\left(1 - \frac{\ell}{R}\right)^3 [2 - \cos \chi (3 - \cos^2 \chi)] + 2 \left[1 - \left(1 - \frac{\ell}{R}\right)^3\right] (1 - \cos \tau) = 4V_R, \quad [64]$$

which is a cubic equation for  $\cos \chi$  in terms of  $\tau$ , as shown below:

$$\cos^3 \chi - 3 \cos \chi + 2 \left\{ 1 - \cos \tau \left[ 1 - \left(1 - \frac{\ell}{R}\right)^3 \right] - 2V_R \right\} = 0. \quad [65]$$

The proper root of Eqn 65 is

$$\cos \chi = 2 \cos \left( \frac{\cos^{-1} \left\{ 2V_R + \left[ 1 - \left(1 - \frac{\ell}{R}\right)^3 \right] \cos \tau - 1 \right\} + 4\pi}{3} \right). \quad [66]$$

Writing non-dimensional versions of Eq [59] and [66] in terms of Eq [35] thru [39] with

$$\bar{t} = \frac{t}{t^1}, \quad [67]$$

we have

$$\begin{aligned} \frac{d^2 \tau}{d\bar{t}^2} + \left( \frac{d\tau}{d\bar{t}} \right)^2 \cot \tau + \frac{KS}{4\alpha^2} \left( \frac{d\tau}{d\bar{t}} \right) = \\ = \frac{Bo(\cos \tau - \cos \chi) + \frac{2}{\alpha} - \cot \tau + \frac{1}{2} \left( \frac{d\tau}{d\bar{t}} \right)^2 \left( \frac{\sin^2 \tau}{\sin^2 \chi} - 1 \right)}{\sin \tau \ln \left( \frac{\tan \frac{\tau}{2}}{\tan \frac{\chi}{2}} \right)} \end{aligned} \quad [68]$$

and

$$\cos \chi = 2 \cos \left( \frac{\cos^{-1} \left\{ 2V_R + [1 - (1 - \alpha)^3] \cos \tau - 1 \right\} + 4\pi}{3} \right).$$

[69]

These two equations can be solved numerically by integration from the initial conditions ( $t = 0$ ,  $\tau = \tau_0$ , and  $\chi = \chi_0$ ) to the desired final conditions of a filled annulus ( $\tau = \pi$ ) to yield a fill time such that

$$\bar{t} \Big|_{\tau=\pi}$$

This fill time is determined by the initial conditions and the parameters in Eq [34].

Equations [68] and [69] were programed for computer solution. Data for the filling of the spherical annulus (Table 27) were input, and the friction factor was chosen as the tube flow factor ( $K = 64$ ). Figure 77 compares the theoretical and test results. The comparison is somewhat inappropriate since outflow from the sphere was initiated after 0.9 sec, whereas the theory does not model this outflow; however, the agreement is relatively good and tends to prove the theory.

## D. DISCUSSION OF RESULTS

### 1. Effects of Incomplete Annulus Refill

The first question is whether the annulus pocket of ullage gas can cause any difficulty during liquid outflow during low-g. As mentioned, the annulus serves to prevent the ingestion of pressurant gas or other vapors into the outlet by providing a continuous liquid path from the outlet to whatever bulk liquid may be inside the screen. If a trapped annulus gas pocket flows into the outflow line, or if it separates the liquid in the annulus from the bulk liquid, thereby causing vapor to be pulled through the screen, then the screen device has failed.



No stability analysis has yet been performed to see under what conditions a gas pocket will move in the annulus to the outlet, although such an analysis is possible. Drop-tower experiments have shown, however, that gas in the annulus tends not to move, even during outflow (Ref 33). This would tend to indicate that the annulus gap may, generally, be made small enough to prevent the ingestion of gas pockets in the annulus while liquid is being drained. More work is required to verify this premise.

A more serious problem is that of losing a liquid path to the bulk liquid. Consider a low-g coast that follows a high-g period in which vapor entered the annulus. Drag forces orient the bulk liquid away from the outlet, but the annulus pocket of vapor remains at the top of the tank, as shown in Fig. 79.

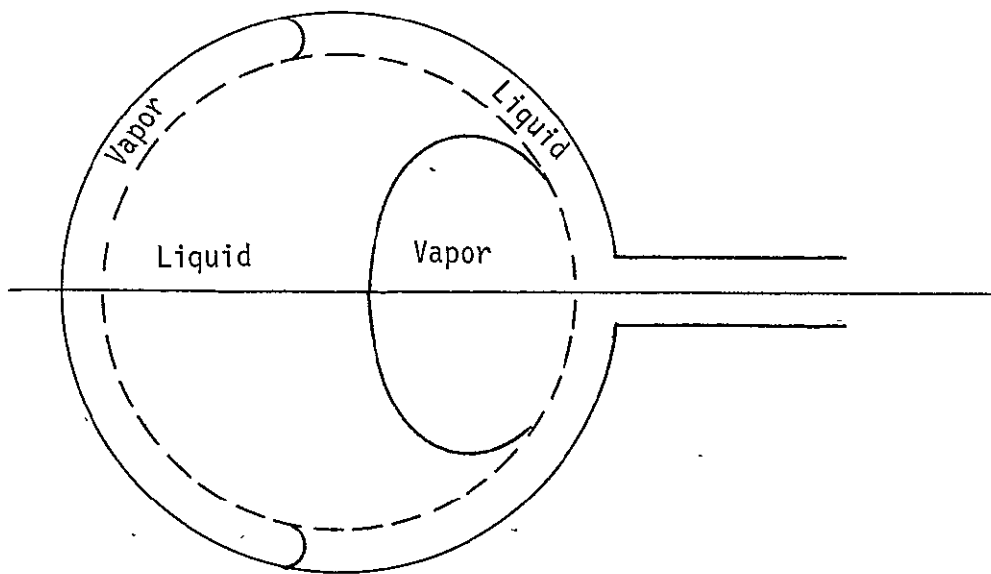


Fig. 79 Possible Liquid/Gas Annulus Condition

As liquid flows out of this tank, a point is reached at which there is no continuous liquid path to the bulk liquid, as shown in Fig. 80.

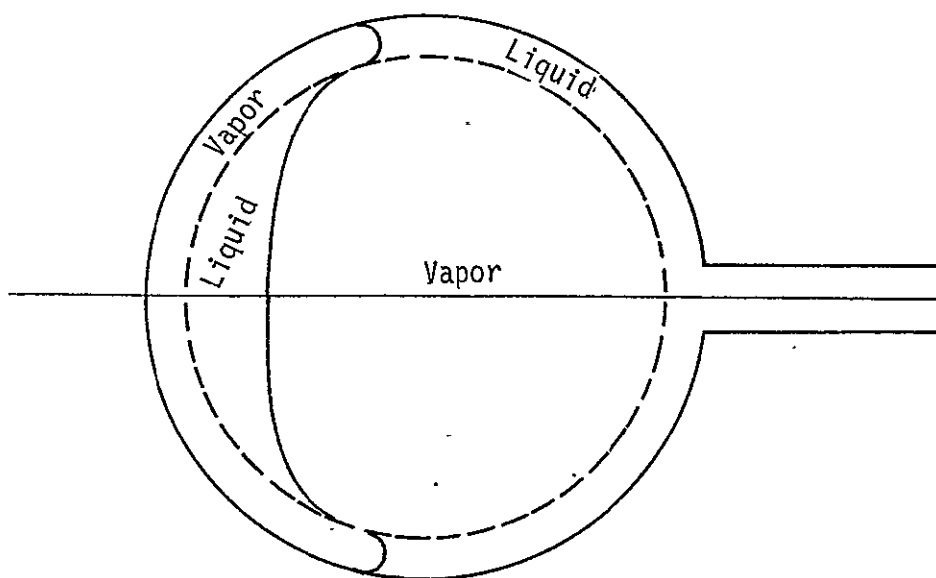


Fig. 80 No Continuous Liquid Path to Bulk Liquid

At this point, the pressurant gas will break through the screen and enter the outflow line, leaving a substantial portion of the bulk liquid unused.

## 2. Possibilities of Breaking the Barrier of a Wetted Screen

As discussed earlier, vapor will enter the concentric screen annulus during thrusting periods. At thrust termination and entrance into a low-gravity condition, the liquid tends to reorient. Capillary forces attempt to refill the annulus until the screen becomes completely rewetted. Then the annulus vapor is trapped at some pressure,  $p_A$ , that is related to the liquid pressure ( $p_\ell$ ) and the curvature of the liquid/vapor interface in the annulus:

$$p_A = p_\ell - \sigma \left( \frac{1}{R_1} + \frac{1}{R_2} \right). \quad [70]$$

$R_1$  and  $R_2$  are the principal radii of curvature.

At low Bond numbers ( $Bo \lesssim 1$ ) and for small annulus gaps,  $\frac{1}{R_2}$  is negligible, and

$$R_1 \approx \frac{\ell}{2}. \quad [71]$$



The pressure of the trapped vapor can be accurately calculated by solving the nonlinear Young-Laplace equation for the surface shape in a gravity field. This equation can be expressed in cylindrical coordinates to give the axisymmetric free-surface height as a function of the radius,  $\eta(r)$ :

$$-\frac{1}{R_1} + \frac{1}{R_2} = \frac{1}{r} \frac{d}{dr} \left[ \frac{r \frac{d\eta}{dr}}{\sqrt{1 + \left(\frac{d\eta}{dr}\right)^2}} \right] = b_o + \frac{\rho a}{\sigma} (\eta - \eta_o), \quad [72]$$

where  $b_o$  is the curvature at  $\eta = \eta_o$  and is an unknown to be determined from the boundary conditions.

The surface slope can be defined in terms of an angle  $\tau$  such that

$$\tan \tau = \frac{d\eta}{dr}. \quad [73]$$

Changing the independent variable to  $\tau$  yields the relations

$$\frac{d\eta}{d\tau} = \frac{\sin \tau}{b + \frac{\rho a}{\sigma} (\eta - \eta_o) - \frac{\sin \tau}{r}} \quad [74]$$

and

$$\frac{dr}{d\tau} = \frac{\cos \tau}{b + \frac{\rho a}{\sigma} (\eta - \eta_o) - \frac{\sin \tau}{r}}. \quad [75]$$

These Bashforth-Adams expressions can be numerically integrated between any two axisymmetric surfaces that form an annulus.

For a sphere containing a concentric screen liner, we can choose a point on the inner sphere at some angle  $\theta$  (see Fig. 81). Then, at that point, we can also choose  $\eta_o$  such that:

$$\left. \begin{aligned} \tau &= \tau_o = \theta - \pi; \\ r &= (R - \ell) \sin \theta; \\ \eta &= \eta_o = -(R - \ell) \cos \theta. \end{aligned} \right\} \quad [76]$$

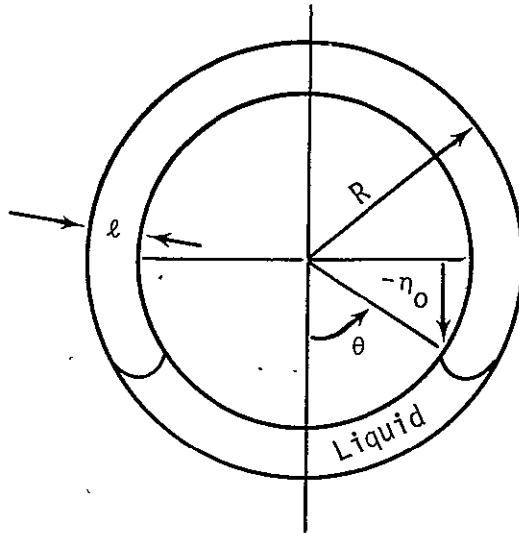


Fig. 81 Schematic Sketch of Annulus

We can now estimate  $b_0$  initially as.

$$b_0 \approx \frac{2}{\ell}, \quad [77]$$

and integrate Eq [74] and [75] from  $\tau = \tau_0$  to a point at which

$$r(\tau) = R \sin \tau. \quad [78]$$

At this point, we let  $\tau = \tau_{\text{final}}$ .

Then the outer sphere will have been reached if the exact value of  $b_0$  was used. The error is measured by the difference:

$$\text{Error} = \eta(\tau_{\text{final}}) + R \cos \tau_{\text{final}}. \quad [79]$$

The integration is repeated with better estimates of  $b_0$  until

$$\left| \frac{\eta(\tau_{\text{final}})}{R \cos \tau_{\text{final}}} + 1 \right| < \epsilon \ll 1, \quad [80]$$

where  $\epsilon$  is some very small number. At this point we have an accurate solution for the surface shape.

From Eq [70], we know that the pressure difference across the free surface of the inner wall is

$$p_A - p_\ell = \sigma b. \quad [81]$$

We can now nondimensionalize this expression to verify the statement associated with Eq [71]. Let

$$\Delta P = \frac{p_A - p_\ell}{\frac{2\sigma}{\ell}} \quad [82]$$

be the nondimensional pressure difference across the interface in the annulus. Then

$$\Delta P = \frac{b}{2} \frac{\ell}{\ell}. \quad [83]$$

Numerical solutions of the Young-Laplace equation then yield the parametric results:

$$\Delta P = F\left(B_o, \frac{\ell}{R}, \theta\right), \quad [84]$$

where  $B_o$  has been defined in Eq [37].

Figure 82 shows a specific example gained from the numerical calculations. It indicates that the capillary pressure difference is

$$p_A - p_\ell \approx \frac{2\sigma}{\ell} \quad [85]$$

for  $20^\circ < \theta < 160^\circ$ .

For a low fill level ( $\theta < 20^\circ$ ), the capillary pressure difference rapidly falls to zero. For a high fill level ( $\theta > 160^\circ$ ), the capillary pressure difference rapidly approaches that of a near-spherical bubble:

$$p_A - p_\ell \approx \frac{4\sigma}{\ell} \quad [86]$$

for  $\theta \approx 180^\circ$ .



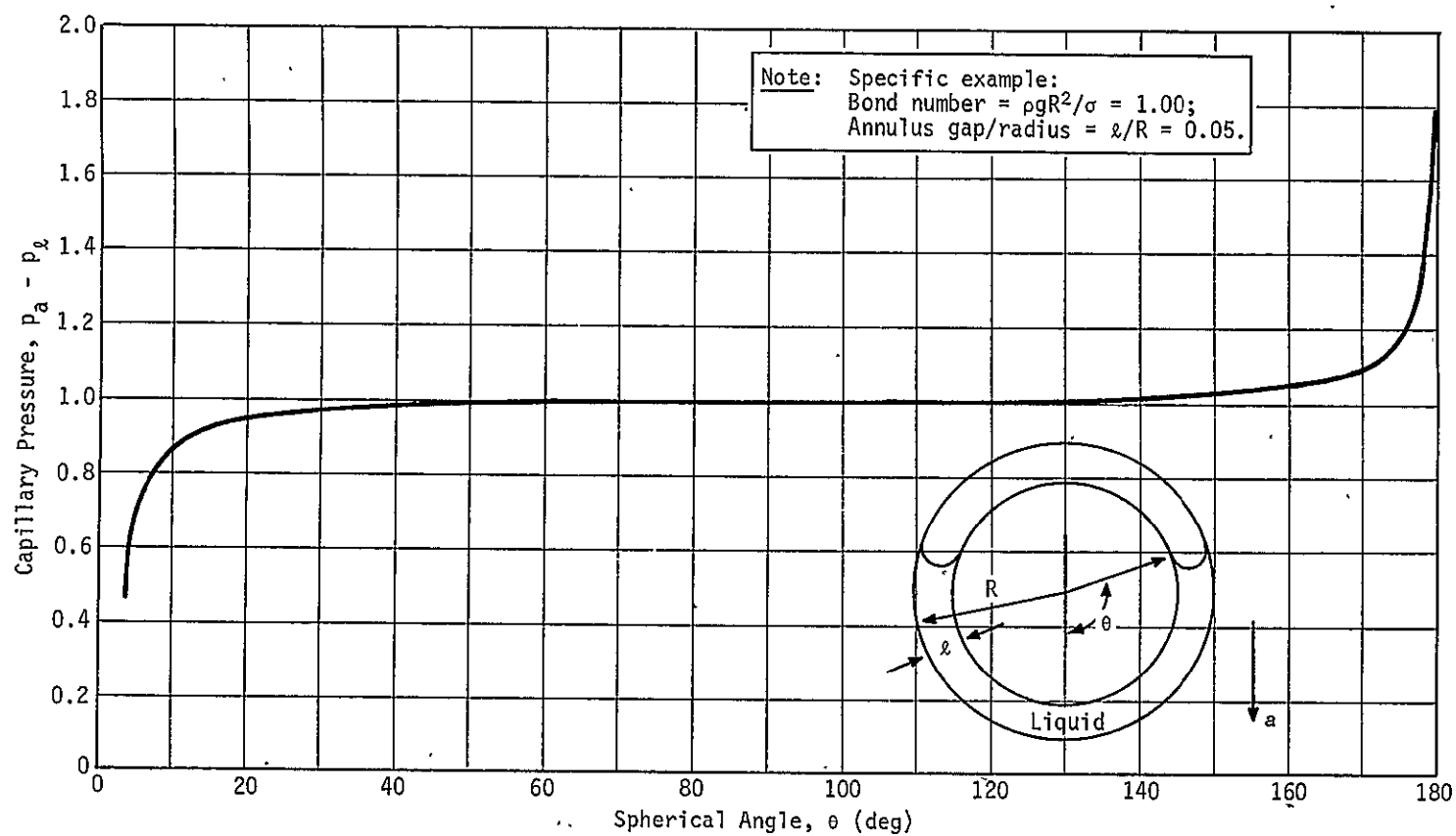


Fig. 82 Nondimensional Capillary Pressure Difference Across a Liquid Interface Inside a Spherical Annulus

These results can be used to evaluate whether an annulus with a wetted screen can be refilled. Assume that a spherical tank with a concentric screen liner is about half full in a high-g condition. Assume that the screen is completely wetted. After entrance into a low-g environment, the liquid will try to fill the annulus as a result of capillary pumping. The ullage trapped in the annulus will be slightly compressed, but its pressure cannot exceed the sum of the capillary pressure and liquid pressure (except by a small amount due to oscillations induced by the fluid dynamics).

The ullage pressure in the bulk region inside the screen liner is about equal to the liquid pressure. Thus, there is a maximum pressure difference across the wetted screen equal to the capillary pressure difference across the liquid interface in the annulus. This situation is schematically represented in Fig. 83.

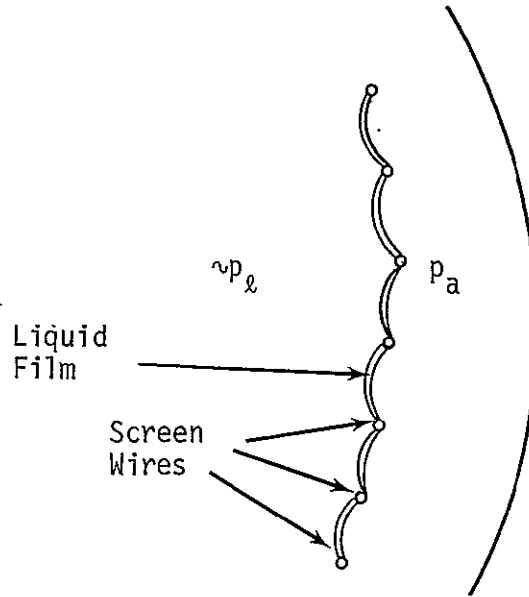


Fig. 83 Schematic Representation of a Wetted Screen

The maximum pressure difference the wetted screen can support is approximately

$$\Delta p_{\text{screen}} \lesssim \frac{4\sigma}{r_{\text{pore}}}, \quad [87]$$

where  $r_{\text{pore}}$  is the effective pore radius. The factor of 4 in this equation is due to the presence of the two liquid surfaces, which have twice the capillary pressure of a single surface.

The capillary pressure difference due to the annulus interface is approximately

$$p_A - p_\ell \approx \frac{2\sigma}{\ell}. \quad [88]$$

Thus, if the capillary pumping is to break the wetting film on the screen and permit the annulus to be refilled, then the annulus gap must be such that

$$\frac{2\sigma}{\ell} > \frac{4\sigma}{r_{\text{pore}}},$$

$$\ell < \frac{1}{2} r_{\text{pore}}. \quad [89]$$

This criterion is most restrictive and impractical to obtain using a wetted screen. Even Dutch-twill screen generally has a pore radius of about 5 to 50  $\mu$ , and cannot provide an annulus gap of that size.

Furthermore, in an annulus gas pocket, the pressure head at a low-gravity level that is favorable for annulus refilling depends on the initial filling level, but is on the order of

$$\Delta p_{\text{gravity}} \sim \rho a R, \quad [90]$$

where  $R$  is the radius of the container. The favorable acceleration required to break through the wetted screen barrier must be such that

$$a > \frac{4\sigma}{\rho R r_{\text{pore}}}. \quad [91]$$

For Test Specimen 2, which was lined with a 200x1400-mesh Dutch-twill screen, this criterion is approximately

$$\frac{4\sigma}{\rho R r_{\text{pore}}} \sim 36 \text{ ft/sec}^2, \quad [92]$$

which is greater than 1 g.



Because of these arguments, we conclude that it is not possible to refill an annulus with a wetted screen in a low-gravity environment.

### 3. Possible Techniques to Minimize Trapped Annulus Vapor Pockets

The primary means of minimizing the size of trapped vapor pockets is to slow the wetting of the screen relative to the annulus fill rate. Since the fill rate is approximately inversely proportional to the annulus gap, by making the gap smaller the fill rate can certainly be made to remove virtually all vapor from the annulus before the bulk liquid wets the entire surface of the screen. This approach, however, is limited by the outflow rate that can be achieved in the annulus.

The static pressure in the annulus is roughly

$$p \approx p_{\text{total}} - \frac{1}{2} \rho v^2; \quad [93]$$

the velocity is

$$v = \frac{\dot{M}}{\rho A}; \quad [94]$$

and the flow area in an axisymmetric annulus is approximately

$$A \approx 2\pi R \ell. \quad [95]$$

Thus, the static pressure  $p$  is related to the annulus gap  $\ell$  by

$$p \approx p_{\text{total}} - \frac{\left( \frac{\rho \dot{M}^2}{8\pi^2 R^2} \right)}{\ell^2}. \quad [96]$$

The maximum pressure difference across the screen that will not pull vapor through the screen is related to the screen pore size:

$$p \geq p_{\text{vapor}} - \frac{2\sigma}{r_{\text{pore}}}. \quad [97]$$

Another approach for minimizing trapped vapor pockets is to take advantage of the fact that, for a given screen and specific mass flow requirements, there is some gap  $\ell$  for which Eq [97] will be violated and for which vapor breaks through the screen during the outflow. In any design, the gap will have to be larger than this limiting value.

If the screen pore is sufficiently fine, the entire screen wets very fast due to wicking. Therefore, the screen must be coarse enough to prevent wicking if annulus refilling is desired.

A third approach to minimize trapped vapor pockets is to baffle the area inside the screen. This will slow and delay the wetting of the entire surface of the screen that results from the reorientation of the bulk liquid. The baffle should be composed of a deflection ring at the wall (to restrict the liquid from splashing on the screen) and a deflection cone in the center (to halt any reorientation spike). The deflection ring and the deflection cone could be connected by a bridge that is vented to allow vapor to flow. Such a device is depicted in Fig. 84.

In summary, three factors -- the design of the screen device, its location, and the mission -- determine whether vapor will enter the outflow annulus during a high-g period. A vapor pocket will be created in the annulus after the high-g period if the entire screen becomes wetted before the vapor can be pushed out by capillary pumping. If the annulus is thin, the vapor pocket will probably remain stuck even during an outflow of liquid; however, it may isolate bulk liquid from flowing into the annulus and out the tank outlet.

The size of trapped vapor pockets can be minimized by:

- 1) Selecting the minimum annulus gap required for successful outflow;
- 2) Selecting perforated plates and square-weave screens, rather than twilled cloth, so that no wicking occurs in the reorientation period following high-g accelerations;
- 3) Using deflection baffles inside the screen to prevent reorientated bulk liquid from completely wetting the screen.

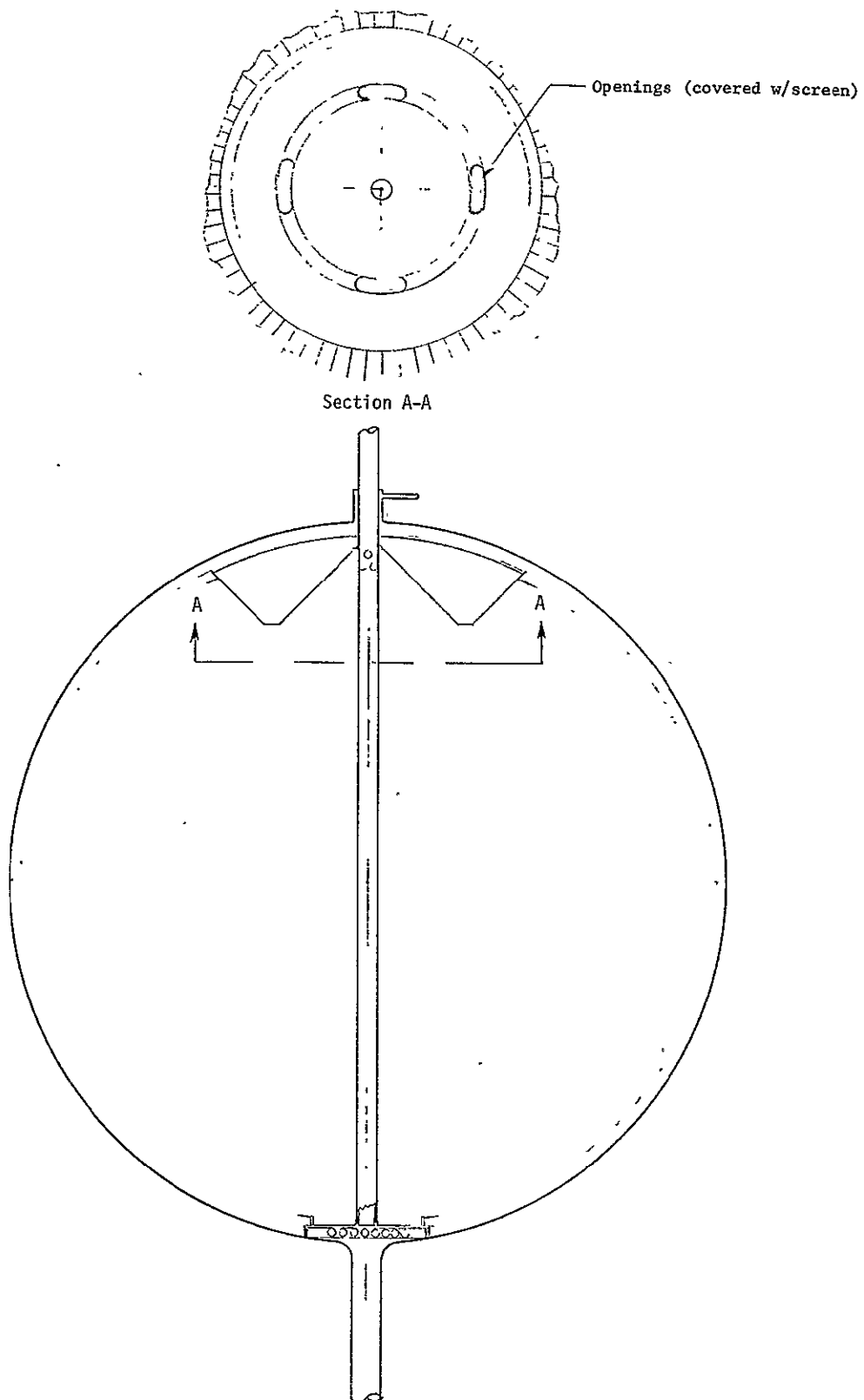


Fig. 84 Sketch of Possible Baffle Scheme  
to Delay Wetting of Screen Liner



## VII. CONCLUSIONS AND RECOMMENDATIONS

### A. CONCLUSIONS

The quantitative and qualitative test results presented in this report are applicable to the design of capillary systems. Typical capillary designs that provide propellant orientation and control during low-g operation are presented and briefly discussed in Chapter I.

The primary objective of the study was to determine and verify, via drop tower experiments, pertinent dimensionless parameters needed to more efficiently design passive systems. The Bo number was verified as the important scaling parameter for hydrostatic stability when the acceleration vector is normal to the foraminous material. A form of the Bo number (the  $\phi$  number) and a modified Ga number were determined as the pertinent scaling parameters for liquid/gas interface stability when the acceleration vector acts parallel to the foraminous material.

For interface stability evaluations, in which a wetted barrier was desired, the majority of tests were made with the liquid  $\frac{1}{4}$ -in. or less above the perforated material. This liquid cover was needed to compensate for misalignment of the drop capsule and test specimen and to keep the barrier wetted at the initiation of the drop test. The motion of this liquid cover under an imposed acceleration must be damped by the capillary pressure difference at the pores. The presence of this momentum contribution tends to reduce the stability criteria. This effect was not thoroughly evaluated during the program, except for slight variations in the liquid cover. It would be desirable to obtain additional data at different liquid cover depths.

Different passive schemes were evaluated with regard to their ability to damp and control liquid under axisymmetric settling. Their passive function is similar to a one-way check valve in that they must permit the passage of pressurization gas and liquid in one direction but prevent the passage of liquid in the opposite direction. The two schemes that showed best performance were the double-plate and the Dutch twill configurations.

Various damping categories (A thru G) are presented as a function of the liquid's impingement We number for the various schemes. The damping was categorized from A, no liquid passage through the barrier, to G, no apparent damping. The results are qualitative since certain parameters, such as the open-to-closed area ratio, were not thoroughly evaluated.

Drop tower test results are also presented that qualitatively complete and incomplete filling of capillary annuli formed by perforated plate (or screen) and the tank wall to provide a path for liquid draining. Methods are presented to provide complete liquid filling and refilling of capillary annuli.

The results of the program show that the designer must have a good understanding of the performance requirements for the capillary device so that he can correctly specify a particular foraminous material.

For example, when ordering Dutch-twill screens, it is usually preferred to specify a particular pressure to be retained (or bubble point) and the desired mesh size; specifying pressure retention, by itself, is usually not adequate. For example, if the material is to be used to form an annular flow passage for liquid draining, the designer is also concerned about flow loss and wicking characteristics. Different foraminous materials can satisfy a specified pressure-retention requirement; however, their flow losses and wicking characteristics may be different. (Square-weave screens and perforated plates will not wick, as will the Dutch twill.)

Similarly, different-diameter wires may be used in a given kind of square-weave screen that has only been specified according to mesh size; accordingly, different samples may have different open dimensions and open-to-closed area ratios. And the number of holes and type of hole pattern in a perforated plate will affect its open-area ratio.

As still another example, merely specifying the pressure-retention requirement is not adequate if the foraminous material is to be used to provide damping. As discussed in Chapter IV, the type of weave is equally important if a screen is to be used, since having a tortuous flow path and the ability to effect complete wetting of the material are definite requirements for good liquid damping.

In general, for any kind of screen the specified pressure retention and mesh size must be consistent. The same is true when purchasing perforated plates; the designer should specify hole size, tolerance limits, and the array (hole pattern). The hole size specified must be consistent with the pressure-retention requirement.

## B. RECOMMENDATIONS

As discussed in Chapter I, no single capillary design is best for all possible storage applications. Rather, different configurations are preferred for different tank sizes and shapes, types of propellants (cryogenics or non-cryogenics), propellant properties (surface tension and density), environmental conditions during prelaunch, launch, and low-g storage, and propellant-orientation, supply, and control requirements.

It would, therefore, be a difficult, if not an impractical task, to conduct a general investigation that would document criteria directly applicable to all possible capillary designs. For example, during this experimental program more than 300 drop tests were conducted and still more data are desired to provide additional quantitative results.

The approach recommended for designing a capillary system is to use this report as a basic guide in designing the preliminary system and to construct subscale and full-scale models to verify the design via bench tests and drop-tower studies.



VIII. REFERENCES

1. *Advanced Maneuvering Propulsion Technology Program, Fourth Quarterly Report (U)*. AFRPL-TR-68-221. Rocketdyne Div, North American Rockwell Corp, Canoga Park, California, December 1968 (Confidential)
2. D. L. Balzer et al: *Advanced Propellant Management System for Spacecraft Propulsion Systems, Phase I - Survey Study and Evaluation*. MCR-69-87 (Contract NAS9-8939). Martin Marietta Corporation, Denver, Colorado, February 1969.
3. H. L. Paynter et al: *Investigation of Space-Storable Propellant Acquisition Devices, Quarterly Letter Report*. MCR-69-575 (Issue 3)(Contract NAS7-754). Martin Marietta Corporation, Denver, Colorado, May, 1970.
4. *Low-Gravity Propellant Control Using Capillary Devices in Large-Scale Cryogenic Vehicles, First Quarterly Progress Report*. 584-4-20B (Contract NAS821465). General Dynamics/Convair Div, San Diego, California, October 1968.
5. H. L. Paynter et al: *Passive Retention/Expulsion Methods for Subcritical Storage of Cryogens*. MCR-70-85 (Issue 3)(Contract NAS9-104801). Martin Marietta Corporation, Denver, Colorado, May, 1970.
6. T. E. Bowman and H. L. Paynter: "Weightless Liquids." *Science Journal*, Vol 2, No. 9, London, England, September 1966.
7. G. R. Page and J. R. Tegart: *Vent Free Fluorine Feed System Analysis*. AFRPL-TR-69-200. Martin Marietta Corporation, Denver, Colorado, September 1969.
8. T. R. Barksdale and H. L. Paynter: *Design, Fabrication, and Testing of Subscale Propellant Tanks with Capillary Traps - Final Report*. MCR-68-11 (Contract NAS8-20837). Martin Marietta Corporation, Denver, Colorado, March 1968.
9. H. M. Satterlee and W. C. Reynolds: *The Dynamics of the Free Liquid Surface in Cylindrical Containers Under Strong Capillary and Weak Gravity Conditions*. LG-2 Mechanical Engineering Dept, Stanford University, Stanford, California, May 1964, p 5.

10. W. J. Masica et al: *Hydrostatic Stability of the Liquid-Vapor Interface in a Gravitational Field*. NASA TN D-2267. May 1964
11. F. Bashforth and J. C. Adams: *An Attempt to Test the Theorie of Capillary Action*. University Press, Cambridge, England, 1883.
12. J. C. Maxwell: "Capillary Action." *The Scientific Papers of James Clark Maxwell*, Vol 2, University Press, Cambridge, England, 1890, pp 541-591.
13. T. E. Bowman: *The Literature of Low-g Propellant Behavior - 1966-1969*. MCR-69-438 (Contract NAS9-8939). Martin Marietta Corporation, Denver, Colorado, September 1969.
14. *Studies of Interfacial Surface Energies, Summary Report*. NASA CR-54175 (Contract NAS3-5744). Harris Research Laboratories, Rockville, Maryland, December 1964.
15. W. A. Zisman: "Relation of Equilibrium Contact Angle of Liquid and Solid Constitution." *Contact Angle - Wettability and Adhesion*, Adv. in Chem. Eng. Series No 43. American Chemical Society, Washington, D.C., 1964, p 20.
16. *Study of Earth-Orbital Experiments for Low-Gravity Fluid Mechanics*. P-66-51 (Vol I). Martin Marietta Corporation, Denver, Colorado, June 1966, p II-6.
17. D. E. Gilmore and T. R. Barksdale: *Low-g Laboratory Annual Progress Report - 1965*. TM-0444-66-2. Martin Marietta Corporation, Denver, Colorado, December 1965.
18. S. J. Kline and F. A. McClintock: "Describing Uncertainties in Single-Sample Experiments." *Mechanical Engineering*, January, 1953.
19. J. J. Bikerman: *Surface Chemistry*. Academic Press, Inc, New York, New York, 1958.
20. A. S. Povitskii and L. Ya. Lyubin: "The Outflow of Gas Into a Liquid Under Weightless Conditions." *Cosmic Research*, Vol 3. No 5, September-October 1965.
21. H. L. Paynter and T. R. Barksdale: *Criteria for Passive Propellant Control Schemes*. Paper 69-531. Presented at AIAA 5th Propulsion Joint Specialist Conference, U.S. Air Force Academy, Colorado, June 1969.

22. C. M. Mackenzie: *Probable Vehicle Acceleration Levels During a Zero-g Space Mission*. TM-0444-64-1. Martin Marietta Corporation, Denver, Colorado, June 1967.
23. F. E. Swalley et al: "Low-Gravity Fluid Behavior and Heat-Transfer Results from the S-IVB-203 Flight." *Proceedings of the Conference on Long-Term Cryo-Propellant Storage in Space*, George C. Marshall Space Flight Center, Alabama, October 12-13, 1966.
24. T. E. Bowman: *Cryogenic Liquid Experiments in Orbit: Vol I - Liquid Settling and Interface Dynamics*. NASA CR-651. Martin Marietta Corporation, Denver, Colorado, December 1966.
25. H. L. Paynter et al: *Zero-g Liquid Propellant Orientation by Passive Control*. Paper 682D. Presented at Air Transport and Space Meeting, New York, New York, April 1964, p 19.
26. M. P. Hollister: *Propellant Containment Utilizing Screen-Mesh and Perforated-Plate Surfaces*. LMSC-A665481. Lockheed Missiles and Space Co., Sunnyvale, California, December 1964.
27. J. P. Gille: *Stability of Capillary Barriers when Subjected to Suddenly Applied Linear Accelerations*. California State College at Long Beach, Long Beach, California, January 1969.
28. D. L. Balzer et al: *Advanced Propellant Management System for Spacecraft Propulsion Systems: Phase II - Detail Design*. MCR-69-436 (Contract NAS9-8939). Martin Marietta Corporation, Denver, Colorado, September 1969.
29. R. Siegal: "Transient Capillary Rise in Reduced and Zero-Gravity Fields." *J. Appl Mech*, Vol 83, June 1961, pp 169-170.
30. D. A. Petrash, T. M. Nelson, and E. W. Otto: *Effect of Surface Energy on the Liquid-Vapor Interface Configuration During Weightlessness*. NASA TN D-1582. January 1963.
31. R. F. Lacovic and J. A. Berns: *Capillary Rise in the Annular Region of Concentric Cylinders During Coast Periods of Atlas-Centaur Flights*. NASA TM X-1558. May 1968.
32. H. L. Paynter: "Time for a Totally Wetting Liquid to Deform from a Gravity-Dominated to a Null-Gravity Equilibrium State." *AIAA Journal*, Vol 2, September 1964, pp 1627-1630.
33. H. L. Paynter et al: *Final Design Report: Development of a Capillary System for Liquid Propellant Orientation During Low-g*. TM-0444-66-3. Martin Marietta Corporation, Denver, Colorado, December 1965.